

**ULTRAFAST
VIBRATIONAL DYNAMICS
OF WATER**

ULTRAFAST VIBRATIONAL DYNAMICS OF WATER

Academisch Proefschrift

ter verkrijging van de graad van doctor
aan de Universiteit van Amsterdam
op gezag van de Rector Magnificus Prof. Mr P.F. van der Heijden
ten overstaan van een door het college voor promoties ingestelde commissie,
in het openbaar te verdedigen in de Aula der Universiteit
op vrijdag 23 januari 2004, te 12.00 uur

door

Arie Jacob Lock
geboren te Maassluis

Promotor: Prof. Dr H.J. Bakker

Faculteit der Natuurwetenschappen, Wiskunde en Informatica

ISBN 90-77209-06-9

The work described in this thesis was performed at the

FOM Institute for Atomic and Molecular Physics (AMOLF)

Kruislaan 407

1098 SJ Amsterdam

The Netherlands

This work is part of the research program of the *Stichting voor Fundamenteel Onderzoek der Materie* (FOM) and was made possible by financial support from the *Nederlandse Organisatie voor Wetenschappelijk Onderzoek* (NWO).

Photography: Tijmen van Dobbenburgh

Contents

1	Introduction	11
1.1	Water and hydrogen bonds	12
1.2	Molecular vibrations	13
1.3	Vibrations in liquids	15
1.4	Non-linear spectroscopic techniques	16
1.5	Outline of the thesis	18
2	Nonlinear Spectroscopy	21
2.1	Nonlinear polarization	22
2.2	Linear absorption	23
2.3	Wave coupling	24
2.4	Nonlinear response theory	25
2.4.1	The coupled Maxwell-Liouville equations	26
2.4.2	Pump-probe response and Feynman diagrams	28
2.5	Pump-probe spectroscopy	33
3	Experimental	35
3.1	Nonlinear optical interactions in crystals	36
3.2	Setup for femtosecond mid-infrared pump-probe spectroscopy	38
3.2.1	Generation of mid-infrared laser pulses	38
3.2.2	Two color pump-probe setup	40
3.3	Sample preparation	42
4	Temperature Dependence of the Vibrational Relaxation in Liquid H₂O	43
4.1	Introduction	44
4.2	Experimental	46
4.3	Results	46
4.4	Kinetic modeling	50
4.5	Relaxation mechanism for the OH-stretch vibration	52
4.6	Conclusions	54

5	Ultrafast Energy Equilibration in Hydrogen-Bonded Liquids	57
5.1	Introduction: water as solvent for (bio)chemical reactions	58
5.2	Experimental	59
5.3	Results	60
5.4	Kinetic modeling	63
5.5	Discussion	64
	5.5.1 Energy redistribution and repositioning	64
	5.5.2 Low frequency hydrogen-bond modes	65
5.6	Conclusions	66
6	Comment on:	
	<i>Vibrational Relaxation and Spectral Evolution Following Ultrafast OH stretch Excitation of Water</i>	
	by A. Pakoulev, Z. Wang, D.D. Dlott	69
6.1	Introduction	70
6.2	Spectral diffusion or vibrational relaxation	70
6.3	Population relaxation or equilibration	72
6.4	Conclusion	73
7	Strong Feedback Effect in the Vibrational Relaxation of Liquid Water	75
7.1	Introduction	76
7.2	Model for the vibrational relaxation of liquid H ₂ O	77
7.3	Results and comparison with experiments	80
7.4	Discussion	86
7.5	Conclusions	87
8	Hydrogen Bond Mediated Energy Transfer in Embedded Water Molecules	89
8.1	Introduction	90
8.2	Experimental	90
8.3	Linear absorption spectrum	92
8.4	Vibrational and orientational relaxation	92
	8.4.1 Transient spectra	92
	8.4.2 Delay time scans	95
	8.4.3 Orientational dynamics	98
8.5	Hydrogen bond mediated energy transfer	99
	8.5.1 The HDO molecule	99
	8.5.2 H ₂ O: the intermediate state	100
	8.5.3 H ₂ O: interpretation of the measurements	103
8.6	Conclusions	105

9	Vibrational Relaxation and Coupling of Two OH-stretch Oscillators with an Intramolecular Hydrogen-Bond	107
9.1	Introduction: The OH-stretch vibration as an indicator for the structure of molecules	108
9.2	Experimental	109
9.2.1	Narrow band excitation	109
9.2.2	Signal detection	109
9.2.3	Broadband excitation	110
9.2.4	Sample	110
9.3	Results	110
9.3.1	Absorption spectrum	110
9.3.2	Transient spectra	111
9.3.3	Delay time scans	113
9.3.4	The sidebands	115
9.3.5	Broadband excitation	118
9.4	Coupling of two O-H oscillators	119
9.5	Discussion	122
9.6	Summary	124
	Bibliography	127
	Summary	137
	Samenvatting	141
	Dankwoord	145

Publications covered in this thesis

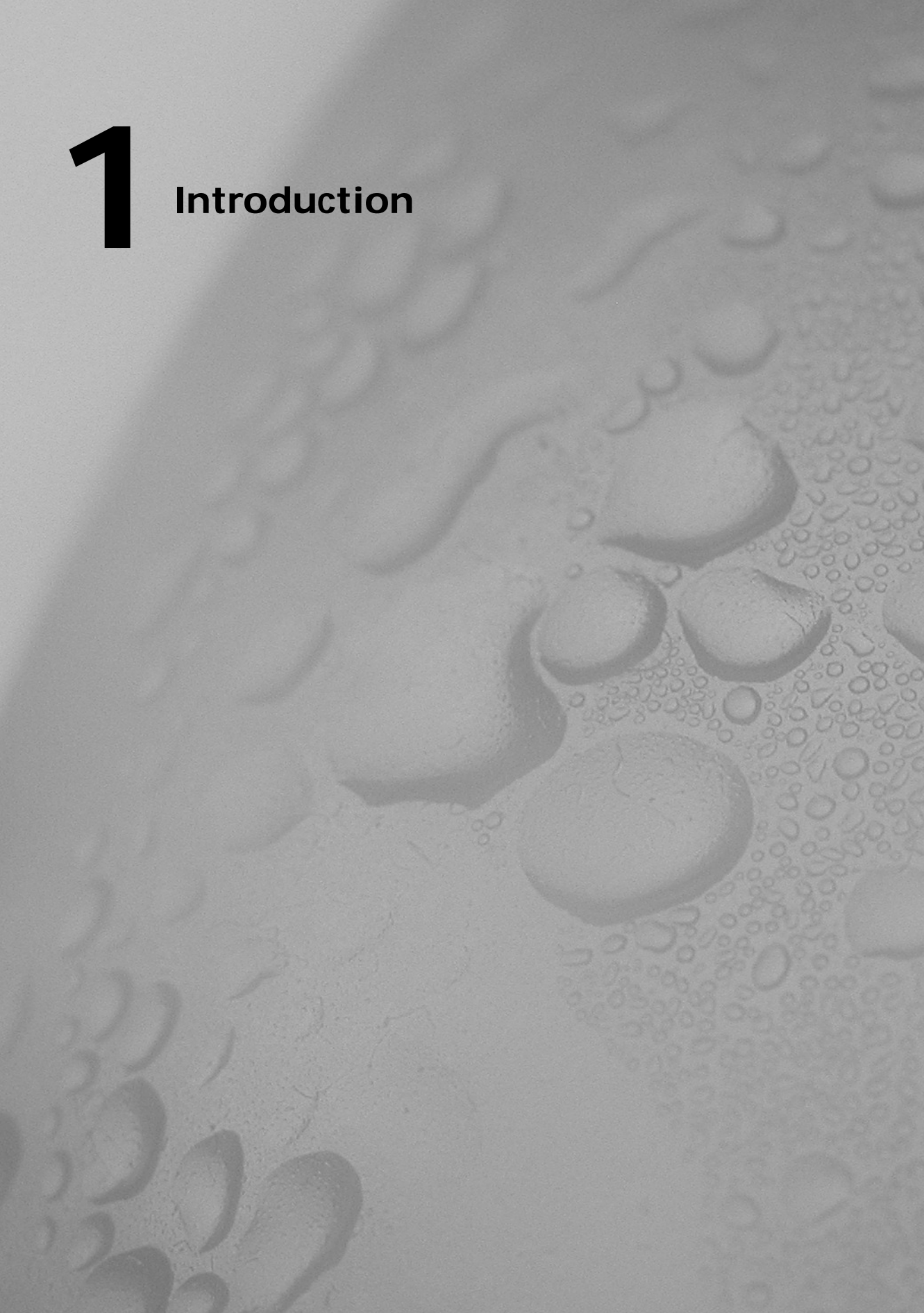
- A. J. Lock, S. Woutersen, and H. J. Bakker. Ultrafast energy equilibration in hydrogen-bonded liquids. *J. Phys. Chem. A*. **105**, 1238 (2001).
- A. J. Lock and H. J. Bakker. Temperature dependence of the vibrational relaxation in liquid H₂O. *J. Chem. Phys.* **117**, 1708 (2002).
- A. J. Lock, S. Woutersen, and H. J. Bakker. Vibrational relaxation and energy equilibration in liquid water. In *Femtochemistry and Femtobiology*, A. Douhal and J. Santamaria, Eds., pp 234-239 (World Scientific, Singapore, 2002).
- A. J. Lock and H. J. Bakker. Vibrational energy relaxation in H₂O. In *Ultrafast Phenomena XIII*, R. D. Miller, M. M. Murnane, N. F. Scherer and A. M. Weiner, Eds., pp 529-531 (Springer, Heidelberg, 2003).
- H. J. Bakker, A. J. Lock and D. Madsen. Comment on: *Vibrational relaxation and spectral evolution following ultrafast OH stretch excitation of water* by A. Pakoulev, Z. Wang, D.D. Dlott. *Accepted for publication in Chem. Phys. Lett.*
- H. J. Bakker, A. J. Lock and D. Madsen. Strong feedback effect in the vibrational relaxation of liquid water. *Submitted to Chem. Phys. Lett.*
- A. J. Lock, J. J. Gilijamse, S. Woutersen and H. J. Bakker. Vibrational relaxation and coupling of two OH-stretch oscillators with an intramolecular hydrogen-bond. *J. Chem. Phys.*, *Scheduled for publication*, February 1, (2004).
- J. J. Gilijamse, A. J. Lock and H. J. Bakker. Hydrogen bond mediated energy transfer in embedded water molecules. *In preparation.*

Other publications

- F. T. H. den Hartog, F. Vacha, A. J. Lock, J. Barber, J. P. Dekker, and S. Völker. Comparison of the excited-state dynamics of five- and six-chlorophyll photosystem II reaction center complexes. *J. Phys. Chem B.* **102**, 1974 (1998).
- A. J. Lock, T. M. H. Creemers and S. Völker. Spectral Diffusion in glasses under high pressure: A study by time-resolved hole-burning. *J. Chem. Phys.* **110**, 7467 (1999).
- T. M. H. Creemers, A. J. Lock, V. Subramaniam, T. M. Jovin, and S. Völker. Three photoconvertible forms of green fluorescent protein identified by spectral hole-burning. *Nature Struct. Biol.* **6**, 557 (1999).
- T. M. H. Creemers, A. J. Lock, V. Subramaniam, T. M. Jovin, and S. Völker. Photophysics and optical switching in green fluorescent protein mutants. *Proc. Natl. Acad. Sci. USA* **97**, 2974 (2000).
- T. M. H. Creemers, A. J. Lock, V. Subramaniam, T. M. Jovin, and S. Völker. Red-shifted mutants of green fluorescent protein: reversible photoconversions studied by hole-burning and high-resolution spectroscopy. *Chem. Phys.* **275**, 109 (2002).
- H. K. Nienhuys, A. J. Lock, R. A. van Santen, and H. J. Bakker. Dynamics of water molecules in an alkaline environment. *J. Chem. Phys.* **117**, 8021 (2002).

1

Introduction



1.1 Water and hydrogen bonds

The ubiquitous presence of water on earth and in everyday life may suggest that the behavior of this liquid is fully understood. Whereas its macroscopic properties like the high specific heat and the high boiling temperature, are attributed to the ability of water to form hydrogen-bonds, its microscopic behavior, which underlies the macroscopic properties, still forms an intriguing puzzle. It is beyond doubt that water molecules play a crucial role in the stabilization of biomolecules, like proteins, and in (bio)chemical reactions, either as reactant themselves, as in the photosynthesis or the ATP/ADP cycle, or as solvent facilitating these reactions. In the latter case, it not only determines the solvation dynamics, but also acts as an acceptant of excess energy dissipated in the reaction. In this context, it is necessary to know the behavior of water molecules in the liquid phase. This is one of the central themes in this thesis.

Water (H_2O) molecules can form up to 4 hydrogen bonds and because hydrogen bonds are cooperative in nature, they strongly affect the structure and dynamics of water. Hydrogen-bonding also plays a dominant role in the structure of macro- and biomolecules. The elementary building blocks for the secondary structure of proteins, the α -helices and β -sheets, owe their actual structure to hydrogen bonding. Hydrogen-bonding is much stronger than the intermolecular Van der Waals interactions, and is therefore expected to dominate the dynamic properties of hydrogen bonding liquids and solids. Breaking and making of hydrogen bonds on picosecond time scales, for example, are ubiquitous in liquid water. Chemical reactions, like acid-base reactions and excited state proton or hydrogen transfer, all involve the breaking of hydrogen bonds. Therefore, understanding water means understanding hydrogen-bonds.

Hydrogen bonding is an attractive interaction between proton donor (A-H) and proton acceptor (B) molecules. The atoms A and B are among the electro-negative atoms oxygen (O), fluorine (F) or nitrogen (N). Hydrogen bonds are directional and the energies associated with hydrogen bonding range from 4 to 40 kJ/mol [14]. In this thesis we will study the $\text{O-H}\cdots\text{O}$ system. In the case of liquid water, hydrogen bonds have an energy of 23.3 kJ/mol [93], while the covalent O-H bond is 492 kJ/mol [81]. Dynamical information on water, in particular on the reorientation time of water molecules in the liquid has been measured in NMR and dielectric relaxation experiments, and was shown to be 8 ps [3, 6, 42]. Infrared spectroscopy is one of the key tools to decipher the structure of gases, liquids and solids. The infrared absorption spectrum of a system is extremely sensitive for hydrogen bonding [28]. Position, width and the intensity of the O-H stretch absorption band changes dramatically, as will be shown in the next sections. This does not imply, however, that the ultrafast dynamics of water and other hydrogen bonded systems can be unraveled using the above mentioned methods, including linear absorption spectroscopy. As will be shown in the coming sections, short infrared pulses form a powerful means to get dynamical information on hydrogen bonding and the behavior of water molecules out of the absorption bands.

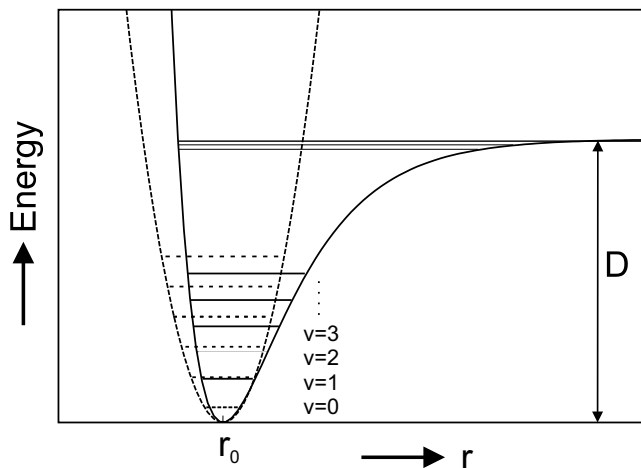


Figure 1.1. Anharmonic (solid line) versus harmonic (dashed line) potential with the energies of their vibrational states. r_0 is the equilibrium distance, D the dissociation energy.

1.2 Molecular vibrations

For the description of the A-H stretch vibration of the A-H \cdots B system, we will first focus on a vibration in a di-atomic molecule. Given a harmonic potential $V = k(r - r_0)^2$, i.e. the potential energy depends on the displacement from the equilibrium position $(r - r_0)$ squared, it can be shown that the energies of the oscillator are given by [35]:

$$G_v = \hbar\omega_0(v + 1/2) \quad (1.1)$$

with $\omega_0 = \sqrt{k/\mu}$, where μ is the reduced mass of the oscillator, k the force constant and v the quantum number. It follows from the above equation that all energy levels of the oscillator are equidistant. The selection rules for the harmonic oscillator are: $\Delta v = \pm 1$. The harmonic oscillator is, however, far from realistic. When the distance between the atoms gets too short, additional repulsive forces come into play, leading to a steeper slope for small internuclear distances. For distances larger than r_0 the slope becomes less steep than harmonic and decreases to zero for very large distances, i.e. the molecule is dissociated into two atoms. These effects can be taken into account using an anharmonic potential, i.e. a potential which contains a term $\propto (r - r_0)^3$ and higher order terms. An example of such a potential is the Morse potential: $V = D(1 - e^{-\beta(r-r_0)})^2$, which has a $(r - r_0)^3$ term in the expansion of the exponential. D is the equilibrium dissociation energy and β a constant. Figure 1.1 shows the Morse

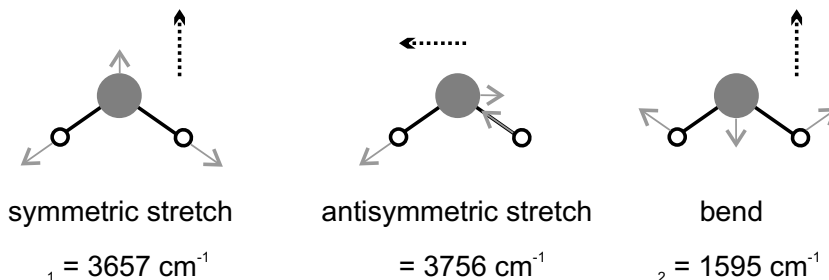


Figure 1.2. Normal mode vibrations for gaseous water, the solid arrows indicate the displacement of each of the atoms, the dashed arrows give the direction of the dipole moment.

potential together with the harmonic potential. The energy of vibrations in a Morse potential are given by [35]:

$$G_v = \hbar\omega_e(v + 1/2) - \omega_e x_e(v + 1/2)^2 \quad (1.2)$$

where $\omega_e x_e$ is the anharmonicity constant. The anharmonicity between the $0 \rightarrow 1$ and $1 \rightarrow 2$ is given by $\Delta = (G_1 - G_0) - (G_2 - G_1) = 2\omega_e x_e$. For an anharmonic oscillator the selection rules read: $\Delta v = \pm 1, \pm 2, \dots$. The levels are occupied following the Boltzmann distribution.

For polyatomic molecules, more vibrations come into play. These vibrations can be identified as normal mode vibrations, i.e. normal coordinates can be constructed along which the progress of a single vibration can be followed. If a vibration changes the dipole moment of the molecule, it is infrared active. If the polarizability changes, it is Raman active.

As a not completely arbitrarily chosen example, let's inspect the normal modes of water. It belongs to the point-group C_{2v} and has three normal mode vibrations, shown in Figure 1.2. All these modes are infrared active. There are two stretching modes, the symmetric ν_1 , and the antisymmetric ν_3 , which absorb at 3657 and 3756 cm^{-1} , respectively. The bending mode (ν_2) is the third normal mode, absorbing at 1595 cm^{-1} . The dipole moments of the symmetric and antisymmetric stretch vibration, indicated by the dashed arrows in Figure 1.2, are orthogonal with respect to each other.

Strictly speaking, the normal mode analysis only holds for small amplitudes of the oscillations, i.e. only the quadratic terms in the potential are taken into account. As we have seen before, oscillations are anharmonic, and therefore, severe modifications are needed on the concept of normal modes. It is no longer possible to resolve the vibrational degrees of freedom in simple normal mode motions. In analogy with Eq. 1.2, the total vibrational energy for a tri-atomic molecule in cm^{-1} reads [35]:

$$\begin{aligned}
G_{v_1, v_2, v_3} = & \omega_1(v_1 + 1/2) + \omega_2(v_2 + 1/2) + \omega_3(v_3 + 1/2) + \\
& x_{11}(v_1 + 1/2)^2 + x_{22}(v_2 + 1/2)^2 + x_{33}(v_3 + 1/2)^2 + \\
& x_{12}(v_1 + 1/2)(v_2 + 1/2) + x_{13}(v_1 + 1/2)(v_3 + 1/2) + \\
& x_{23}(v_2 + 1/2)(v_3 + 1/2) + \dots
\end{aligned} \tag{1.3}$$

where x_{ii} are the diagonal and x_{ij} the cross anharmonicities. For gas phase water, the following anharmonicity constant were found [35]: $\omega_1=3825.25 \text{ cm}^{-1}$, $\omega_2=1654.91 \text{ cm}^{-1}$, $\omega_3=3935.59 \text{ cm}^{-1}$, $x_{11}=-43.8 \text{ cm}^{-1}$, $x_{22}=-19.5 \text{ cm}^{-1}$, $x_{33}=-46.3 \text{ cm}^{-1}$, $x_{12}=-20.0 \text{ cm}^{-1}$, $x_{23}=-19.8 \text{ cm}^{-1}$, $x_{13}=-155.0 \text{ cm}^{-1}$. Using Eq. 1.3 the observed ir-frequencies can be calculated.

1.3 Vibrations in liquids

The validity of selection rules and the clear spectral positions of normal modes in the gas phase water, completely disappear in the liquid phase due to hydrogen bonding. Especially, the stretching vibrations in water, are extremely sensitive for hydrogen bonding. The A–H stretch frequency for a system A–H \cdots B strongly depends on the distance between atoms A and B. For weak hydrogen bonds, i.e. long distances, the A–H stretch frequency resembles the gas phase frequency. For very strong hydrogen bonds, the A–H stretch frequency is shifted to the red. For water, the red shift is approximately 300 cm^{-1} . There is a strong correlation between the OH-stretch frequency and the O–O distance [58], as is generally the case for A–H \cdots B systems. Recent calculations, however, have shown that for water not only the hydrogen bond length but also the hydrogen bond angle determines to a minor extent the stretch frequency [77]. The ν_2 bending mode of water, undergoes a small blue shift upon hydrogen bonding.

In addition to the red shift, a broadening of the spectral bands occurs for the stretch frequencies. The broadening stems from the dephasing of an ensemble of excited oscillators. Different mechanisms are responsible for the broadening of absorption lines. In two limiting cases, they are either static or dynamic. Dynamic contributions to the line-broadening are responsible for the homogeneous broadening and described by the dephasing time T_2 . This dephasing time reflects the loss of coherence of an ensemble of oscillators with the same center frequency. There are two causes for this loss: population relaxation to the ground state with time constant T_1 and pure dephasing with a time constant T_2^* . The latter time constant describes all very fast, small frequency jumps around the center frequency. A homogeneously broadened line shape is described by a Lorentzian with a width Γ_{hom} , which can be related to the time scales as follows:

$$\pi\Gamma_{\text{hom}} = \frac{1}{T_2} = \frac{1}{2T_1} + \frac{1}{T_2^*} \quad (1.4)$$

Static contributions to the line broadening are caused by static differences in the transition frequencies between different oscillators, i.e. different oscillators experience a different static environment. This leads to a Gaussian absorption line shape with a width that reflects the range of possible transition frequencies. The absorption band is inhomogeneously broadened.

A more general description of line broadening processes considers an oscillator with time-dependent transition frequency $\omega(t) = \omega_0 + d\omega(t)$. If the Gauss-Markov assumption is applied for the second term, i.e. $\langle d\omega(0)d\omega(t) \rangle = D^2 e^{-t/\tau_c}$, with D the width of the Gaussian distribution of the excursions $d\omega(t)$ and τ_c the typical frequency modulation time, the line shape can be calculated analytically [61]. The static and dynamic contributions to the line broadening are two limiting cases. The fast modulation limit ($D\tau_c \ll 1$) describes homogeneous broadening, whereas the slow modulation limit ($D\tau_c \gg 1$) describes inhomogeneous broadening.

For water, at least two line broadening mechanisms are present, a fast process leading to homogeneous broadening and a slow one leading to inhomogeneous broadening. In other words, the OH-stretch band consists of an inhomogeneous distribution of homogeneously broadened bands. If the changes in the transition frequency are neither very fast nor very slow, but change during the experiment, the process is called spectral diffusion. In this case, water molecules change orientations and positions, and continuously form and break hydrogen bonds towards neighboring water molecules on a picosecond time scale, which affects the OH-stretch frequency.

1.4 Non-linear spectroscopic techniques

All dynamical information, which can be extracted from the homogeneous line-width, is hidden under the inhomogeneous band. The band represents the average of an ensemble of oscillators. Therefore, other experimental techniques are necessary to reveal the broadening mechanism and the underlying dynamics.

These techniques can be grouped together as nonlinear spectroscopies, which means that the generated response scales with E^n , with E the total E-field and $n > 1$. Among the techniques are two and three pulse photon echo spectroscopy [75, 89, 91], coherent anti-Stokes Raman scattering (CARS) [61] and various types of pump-probe spectroscopies, like hole-burning, saturation spectroscopy [20, 25, 34, 37, 38, 46, 54, 64, 106, 107] and 2D-IR spectroscopy [21, 31, 41, 111, 112], which all have been applied to vibrations in the condensed phase. The above mentioned techniques are all third-order nonlinear techniques, which means that the response from the sample is generated from three interactions with the total light field.

Photon echo spectroscopy is a fully time-domain technique and makes use of two coherence periods. A short pulse excites an inhomogeneous distribution of oscillators,

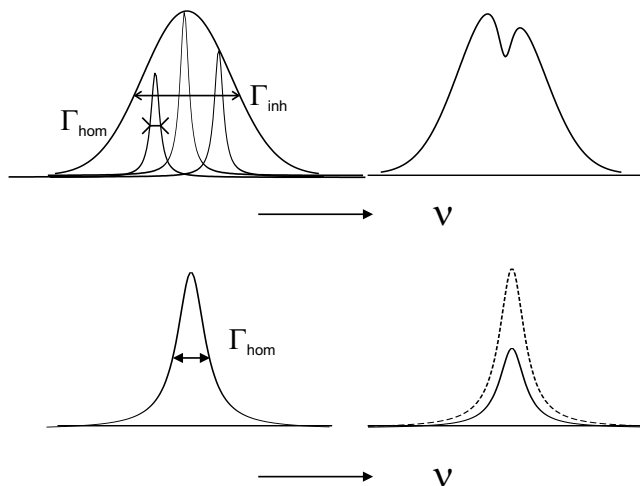


Figure 1.3. Left: Inhomogeneous (top) and homogeneous (bottom) line broadening. right: the effect on the absorption spectrum after pumping an inhomogeneous (top) and a homogeneous band.

which will all dephase differently due to the different transition frequencies in the excited ensemble. The third interaction with the light field initiates a rephasing of the dephased oscillators, leading to the production of an echo, which is well defined in time. The temporal shape and the shift in time of the maximum of the echo, enables the experimentalist, for example, to determine the spectral diffusion time scale. Recently, this technique has been applied in the infrared for HDO dissolved in D_2O [91]. A T_2^* was found of 90 fs.

Another technique to extract dynamical information from broadened absorption bands is CARS. In such an experiment, two incoming fields with frequencies ω_1 and ω_2 interact with the molecule. The frequency difference between the incoming fields is resonant with a transition to a state v in the molecule: $\omega_1 - \omega_2 = \omega_v$. Field ω_1 excites the molecules, whereas ω_2 is the Stokes line back to the level v in the molecule. The third interaction is again with light field ω_1 and generates the anti-Stokes signal at $2\omega_1 - \omega_2$ [61, 84].

In a hole-burning experiment two pulses are used [99]. The first narrow-band pump selects a sub-ensemble of oscillators, with the same surroundings. Due to this excitation, a hole is created in the absorption profile, see Figure 1.3. A second, tunable laser, measures the transient absorption spectrum. From these measurements, the hole-width, which is related to the homogeneous line-width and lifetime of the excited

state [99] can be extracted. The broadening of the hole with time is a measure for the spectral diffusion.

The technique we used in this thesis is femtosecond mid-infrared saturation spectroscopy. This technique is similar to that of hole-burning, however, the emphasis lies more on time- than on frequency-resolution. It will be shown in Chapter 3, that ultrashort pulses can be generated with enough spectral selectivity. Saturation spectroscopy gives information on the lifetimes T_1 , on anharmonicities and couplings of vibrations. Recent mid-infrared saturation spectroscopic studies of hydrogen-bonded systems were mainly focused on water monomers [23], dilute solutions of HDO in D_2O [20, 25, 64, 103, 104, 108] and alcohol clusters [27, 107, 48]. More recent work focuses on aqueous solutions of ions [43, 68], OD^- -ions dissolved in water [62] and proton transfer in photo-acids [78].

1.5 Outline of the thesis

The central theme of this thesis is the study of the vibrational relaxation of water and hydrogen-bonded systems. Before the presentation of pump-probe results, a formal description of the nonlinear polarization, with which wave mixing as well as pump-probe signals can be described, is given in Chapter 2. The third chapter deals with the generation of mid-infrared pulses and their usage in pump-probe spectroscopy.

The systems studied in Chapters 4-9 are depicted in Figure 1.4 together with the infrared absorption band of the OH-stretch region. As one can see from the large spread in positions, line shapes and band widths, the character of the hydrogen bond interaction is very different from sample to sample.

In Chapter 4, we study the temperature dependence of the lifetime of the OH-stretch vibration for pure liquid water and give an explanation for the observed behavior in terms of energy relaxation pathways. Chapter 5 focuses on the energy equilibration aspect in water. A comparison is made with the behavior measured in pure ethanol.

Dlott and coworkers [69] performed a coherent anti-Stokes Raman experiment with longer (picosecond) pulses on pure water. In their study, they present an alternative picture of the vibrational dynamics of liquid water. Chapter 6 forms the comment on this paper. In Chapter 7 an elaborate theoretical model is presented which both corroborates our findings and is able to explain their results.

The last two chapters are concerned with the study of OH-oscillators in dilute solutions. In contrast to earlier studies [23] where only water monomers without hydrogen bonds were studied, we investigate water monomers with one or two hydrogen bonds to acetone molecules. The results are presented in Chapter 8. The last Chapter is devoted to the study of an alcohol with two neighboring OH-groups that are hydrogen-bonded. Next to vibrational relaxation, we study the coupling between both groups.

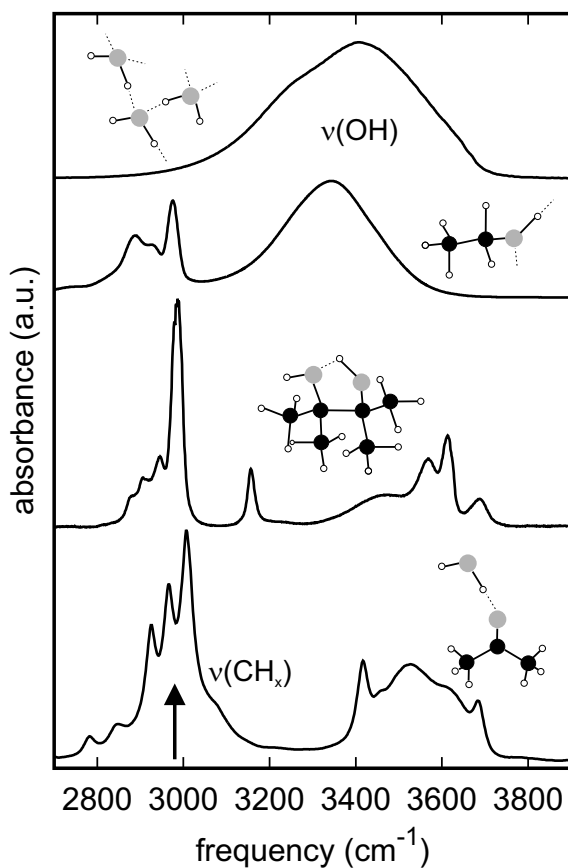


Figure 1.4. Infrared absorption spectra of the molecules studied. From top to bottom: spectrum of pure water (H₂O), pure ethanol (C₂H₅OH), pinacol (2,3-dimethyl-2,3-butanediol) dissolved in CDCl₃ and water-acetone complexes dissolved in CCl₄. The OH-stretch bands can be found around 3400 cm⁻¹ and higher. The narrow bands around 3000 cm⁻¹ are the different CH-stretch modes.

2

Nonlinear Spectroscopy

This chapter provides the reader with the basic concepts of the nonlinear spectroscopic techniques used in this thesis. First, we will show that intense light fields are able to set up a nonlinear polarization in a material, that in turn can act as a source for new radiation fields. To arrive at that point, we will first define the nonlinear polarization and the nonlinear susceptibilities. Section 2 gives an example of effects associated with linear polarization: absorption and refraction. In the subsequent section, we will discuss the wave equation for the propagation of intense electric fields. It follows from this wave equation that the generated nonlinear polarization is a source of new light fields. The next section shows that the generated nonlinear polarization can be described using so-called response functions. The measured pump-probe signal can be derived from the nonlinear polarization. In the last section an expression for the pump-probe signal is presented under specific experimental conditions.

2.1 Nonlinear polarization

The description of nonlinear interactions starts with the expansion of the polarization in powers of the electric field. If the incoming E-fields can be written as a sum of monochromatic plane waves, the polarization takes the form:

$$\begin{aligned}\mathbf{P}(\mathbf{k}, \omega) &= \mathbf{P}^{(1)}(\mathbf{k}, \omega) + \mathbf{P}^{(2)}(\mathbf{k}, \omega) + \mathbf{P}^{(3)}(\mathbf{k}, \omega) + \dots \\ &= \mathbf{P}^{(1)}(\mathbf{k}, \omega) + \mathbf{P}^{(\text{NL})}(\mathbf{k}, \omega),\end{aligned}\tag{2.1}$$

where the linear polarization is given by

$$\mathbf{P}^{(1)}(\mathbf{k}, \omega) = \epsilon_0 \chi^{(1)}(\mathbf{k}, \omega) \cdot \mathbf{E}(\mathbf{k}, \omega)\tag{2.2}$$

and the second-order nonlinear polarization by

$$\mathbf{P}^{(2)}(\mathbf{k}, \omega) = \epsilon_0 \chi^{(2)}(\mathbf{k} = \mathbf{k}_i + \mathbf{k}_j, \omega = \omega_i + \omega_j) : \mathbf{E}(\mathbf{k}_i, \omega_i) \mathbf{E}(\mathbf{k}_j, \omega_j)\tag{2.3}$$

For the higher-order contributions to the nonlinear polarization, similar expressions hold. In the above equations $\chi^{(n)}$ is the n^{th} order susceptibility. The time and position dependent polarization is given by:

$$\begin{aligned}\mathbf{P}(\mathbf{r}, t) &= \int_{-\infty}^{\infty} \chi^{(1)}(\mathbf{r} - \mathbf{r}', t - t') \cdot \mathbf{E}(\mathbf{r}', t) d\mathbf{r}' dt \\ &+ \int_{-\infty}^{\infty} \chi^{(2)}(\mathbf{r} - \mathbf{r}_1, t - t_1; \mathbf{r} - \mathbf{r}_2, t - t_2) \\ &\quad : \mathbf{E}(\mathbf{r}_1, t_1) \mathbf{E}(\mathbf{r}_2, t_2) d\mathbf{r}_1 dt_1 d\mathbf{r}_2 dt_2 \\ &+ \dots\end{aligned}\tag{2.4}$$

The linear polarization is responsible for optical effects like light absorption and refraction, while the nonlinear polarization forms the basis of effects like multiwave mixing and many spectroscopic techniques like photon echoes, coherent anti-Stokes Raman scattering and saturation spectroscopy.

All materials possess higher order susceptibilities, although their values are in general so small that their effect is negligible using low-intensity light sources. The development of lasers, however, provided intensities that are so high that the higher order susceptibilities have become important. This has led to the discovery of many new effects and has subsequently given the field of optics a new impulse.

2.2 Linear absorption

The wave equation which describes the propagation of optical waves in a medium, can be extracted from the Maxwell equations:

$$\nabla \times \nabla \times \mathbf{E}(\mathbf{r}, t) + \frac{1}{c^2} \frac{\partial^2}{\partial t^2} \mathbf{E}(\mathbf{r}, t) = -\frac{1}{\epsilon_0 c^2} \frac{\partial^2}{\partial t^2} \mathbf{P}(\mathbf{r}, t) \quad (2.5)$$

If the nonlinear polarization can be neglected, the polarization is given by:

$$\mathbf{P} = \epsilon_0 \chi^{(1)} \mathbf{E} \quad (2.6)$$

Now, assume that a solution of wave equation 2.5 is given by a traveling wave in the z direction:

$$E(z, t) = \tilde{E}(k, \omega) = \frac{1}{2\pi} \int E(k, \omega) e^{ikz - i\omega t} d\omega \quad (2.7)$$

Substitution of this solution in the Maxwell equation with \mathbf{P} given by Eq. 2.2, and making use of $\nabla \times \nabla \times \mathbf{E} = \nabla(\nabla \cdot \mathbf{E}) - \nabla^2 \mathbf{E} = -\nabla^2 \mathbf{E}$ for insulating media, leads to:

$$\begin{aligned} k &= \frac{\omega}{c} \sqrt{\epsilon(k, \omega)} = \frac{\omega}{c} \sqrt{1 + \chi^{(1)}(k, \omega)} = \frac{\omega}{c} \sqrt{1 + \chi' + i\chi''} \\ &= \frac{\omega}{c} (n(\omega) + i\kappa(\omega)) \end{aligned} \quad (2.8)$$

where we have split up the susceptibility in its real and complex part: $\chi = \chi' + i\chi''$. Furthermore, ϵ is the complex dielectric function, n is the index of refraction and κ the extinction coefficient. As one can see, the index of refraction and the absorption index are described by the real and imaginary parts of the linear susceptibility, respectively. The E-field thus reads:

$$E(z, t) = \frac{1}{2\pi} \int E(\omega, k) e^{-i\omega t} e^{i\omega n z / c - \alpha z / 2} d\omega \quad (2.9)$$

with $\alpha \equiv 2\omega\kappa/c$, the absorption coefficient.

Since the intensity is proportional to the square of the absolute value of the E-field, we get for the transmittance of the sample:

$$T = I(z)/I_0 = e^{-\sigma(\omega)\rho_0 z} \quad (2.10)$$

with I_0 the intensity of the light without sample. In the above formula ρ_0 is the number density of absorbers and $\sigma(\omega) = \alpha/\rho_0$ the absorption cross section. The above formula is known as the Lambert-Beer law.

2.3 Wave coupling

For the generation of mid-infrared laser pulses, we make use of different wave-mixing techniques, as will be explained in Chapter 3. In a wave-mixing technique incoming fields with a high intensity will generate a new outgoing field by means of the nonlinear polarization $\mathbf{P}^{(NL)}$. In order to calculate the newly generated fields, it is necessary to know what wave equation the E-fields obey. We start with the Maxwell wave equation (2.5) and using $\mathbf{D} = \epsilon\mathbf{E} = \epsilon_0(1 + \chi)\mathbf{E} = \epsilon_0\mathbf{E} + \mathbf{P}^{(1)}$, with \mathbf{D} the displacement vector, we get:

$$\frac{\partial^2}{\partial z^2}\mathbf{E}(\mathbf{r}, t) - \frac{1}{\epsilon_0 c^2} \frac{\partial^2}{\partial t^2}\mathbf{D}(\mathbf{r}, t) = \frac{1}{\epsilon_0 c^2} \frac{\partial^2}{\partial t^2}\mathbf{P}^{(NL)}(\mathbf{r}, t) \quad (2.11)$$

Suppose the incoming E-field can be written as:

$$E(z, t) = \mathcal{E}(z, t)e^{ikz-i\omega t} + c.c. \quad (2.12)$$

then the first term of Eq. 2.11 gives:

$$\frac{\partial^2}{\partial z^2}E(z, t) = \left(\frac{\partial^2 \mathcal{E}}{\partial z^2} + 2ik\frac{\partial \mathcal{E}}{\partial z} - k^2\mathcal{E}\right)e^{ikz-i\omega t} \quad (2.13)$$

If we write the E-field as a Fourier integral: $E(z, t) = \int \mathcal{E}(\omega + \eta)e^{ikz-i(\omega+\eta)t} d\eta + c.c.$, the displacement is given by:

$$D(z, t) = \int \epsilon(\omega + \eta)\mathcal{E}(\omega + \eta)e^{ikz-i(\omega+\eta)t} d\eta + c.c. \quad (2.14)$$

The second second term of Eq. 2.11 is:

$$\begin{aligned} \frac{\partial^2}{\partial t^2}D(z, t) &= - \int (\omega + \eta)^2 \epsilon(\omega + \eta)\mathcal{E}(\omega + \eta)e^{ikz-i(\omega+\eta)t} d\eta + c.c. \\ &= - \int (\omega^2 \epsilon(\omega) + 2\omega\eta\epsilon(\omega) + \omega^2\eta\frac{\partial\epsilon}{\partial\omega})\mathcal{E}(\omega + \eta)e^{ikz-i(\omega+\eta)t} d\eta + c.c. \\ &= -[\omega^2\epsilon(\omega)\mathcal{E}e^{ikz-i\omega t} + (2\omega\epsilon(\omega) + \omega^2\frac{\partial\epsilon}{\partial\omega})] \\ &\quad \times \int \eta\mathcal{E}(\omega + \eta)e^{ikz-i(\omega+\eta)t} d\eta + c.c. \end{aligned} \quad (2.15)$$

In the above equations we have assumed that the dielectric constant weakly depends on the frequency ω and can therefore be written as $\epsilon(\omega + \eta) = \epsilon(\omega) + \eta\frac{\partial\epsilon}{\partial\omega}$. The term in between the parentheses equals $\partial\omega^2\epsilon(\omega)/\partial\omega = 2kc^2\frac{\partial k}{\partial\omega} = \frac{2kc^2}{v_g}$, with v_g the group velocity. Terms of second or higher order in η can be neglected.

Wave coupling in a nonlinear medium leads to energy transfer among waves. Wave amplitudes are expected to change in propagation. This transfer of energy will only be significant after the waves travel over a distance much longer than their wavelengths. Therefore,

$$\left| \frac{\partial^2 \mathcal{E}(z, t)}{\partial z^2} \right| \ll \left| k \frac{\partial \mathcal{E}}{\partial z} \right| \quad (2.16)$$

This approximation is known as the slowly varying amplitude approximation [84]. Because the following holds:

$$\int \eta \mathcal{E}(\omega + \eta) e^{ikz - i(\omega + \eta)t} d\eta = i e^{ikz - i\omega t} \frac{\partial \mathcal{E}(z, t)}{\partial t}, \quad (2.17)$$

the wave equation (2.11) in the slowly varying amplitude approximation reads:

$$\left(\frac{\partial}{\partial z} + \frac{1}{v_g} \frac{\partial}{\partial t} \right) \mathcal{E}(z, t) e^{ikz - i\omega t} = \frac{1}{2i\epsilon_0 k c^2} \frac{\partial^2 P^{(NL)}(z, t)}{\partial t^2} \quad (2.18)$$

The nonlinear polarization generated by the incident fields acts as a source for new frequencies. These newly generated E-fields obey the above equation.

Different combinations of incoming fields lead to a variety of new frequencies and wave-vectors:

$$k_s = \pm k_1 \pm k_2 \dots \pm k_n \quad (2.19)$$

$$\omega_s = \pm \omega_1 \pm \omega_2 \dots \pm \omega_n \quad (2.20)$$

The wave-vectors of the nonlinear polarization and the generated E-fields are close to each other, but due to frequency dispersion and the geometry of the experiment not exactly the same. The wave-vector mismatch $\Delta k = k_s - \sum_i k_i$ determines the efficiency of the energy conversion process [7, 61, 84]. When the wave-vector mismatch $\Delta k = 0$, the *phase-matching condition* is fulfilled and energy is efficiently transferred among waves, see also Section 3.1.

2.4 Nonlinear response theory

The experiments described in this thesis are all performed with the pump-probe technique. An intense pump pulse is used to excite part of the molecules to an excited state. Because this excited population does not form an equilibrium situation, it will decay to the ground state. The second pulse, the probe pulse, monitors the absorption changes caused by the excitation with the pump pulse. In this section, we will show how the pump-probe signal can be described in terms of the generated nonlinear polarization. Because the liquids and solutions we studied form an isotropic medium with inversion symmetry, the second order polarization $P^{(2)}$ vanishes. Therefore, the

lowest order nonlinear contribution to the polarization arises from the third-order polarization $P^{(3)}$. This third-order polarization is measured in the same direction as the probe, i.e. the nonlinear polarization induces absorption changes measured by the probe pulse. The phase-matching condition therefore requires that the pump pulse interacts twice with the sample and the probe pulse once. The layout of the pump-probe setup is shown in Figure 2.1.

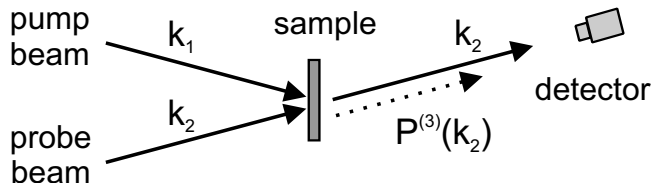


Figure 2.1. Beam configuration for pump-probe spectroscopy.

2.4.1 The coupled Maxwell-Liouville equations

This section gives a microscopic treatment of the interaction of matter with electromagnetic waves, leading to the generation of a third-order polarization, which contains all the system-specific information and acts as a source for the radiation field.

We will study the relaxation dynamics of a molecule in a bath. This bath can be formed by the solvent molecules surrounding a solute or by neighboring, identical molecules. Because the external interaction is resonant with one vibrational mode in particular, we will denote that mode as the system.

The Hamiltonian for this kind of systems is given by:

$$H = H_0 + H_{\text{bath}} + H_{\text{int}} \quad (2.21)$$

In the above equation the first term represents the molecular Hamiltonian of the single oscillator under study, the second term accounts for the random perturbations of the system by the thermal reservoir around the system (bath modes). The last term represents the interaction between the external field and the system-bath complex. The coupling between the radiation field and the material is given by

$$H_{\text{int}} = - \int d\mathbf{r} \mathbf{P}(\mathbf{r}) \cdot \mathbf{E}(\mathbf{r}, t) \quad (2.22)$$

For particles smaller than the optical wavelength, the dipole approximation can be applied. For a single particle located at \mathbf{r} , we get:

$$H_{int} = -\mathbf{E}(\mathbf{r}, t) \cdot \mathbf{V} \quad (2.23)$$

$$\mathbf{V} = \sum_{\alpha} q_{\alpha}(\mathbf{r} - \mathbf{r}_{\alpha}) \quad (2.24)$$

where V is the dipole operator and α runs over all electrons and nuclei with charges q_{α} and positions \mathbf{r}_{α} .

Because we are dealing with an ensemble of oscillators which all have a slightly different frequency, we have to take into account the statistical averages. Therefore we make use of density operators: $\rho(t) \equiv \sum_k P_k |\psi_k(t)\rangle\langle\psi_k(t)|$, where the summation is over the eigenstates $|\psi_k(t)\rangle$ and P_k is the probability of the system to be in state $|\psi_k(t)\rangle$

Using a density matrix formulation, the dynamics is governed by the so-called Liouville-von Neumann equation:

$$\frac{\partial \rho}{\partial t} = -i/\hbar [H_0 + H_{int}, \rho] + \left(\frac{\partial \rho}{\partial t}\right)_{\text{relax}} \quad (2.25)$$

with

$$\left(\frac{\partial \rho}{\partial t}\right)_{\text{relax}} \equiv -i/\hbar [H_{\text{bath}}, \rho] \quad (2.26)$$

For simplicity, we just take a phenomenological relaxation rate:

$$\left(\frac{\partial \rho}{\partial t}\right)_{\text{relax}, vv'} = -\Gamma_{vv'} \rho_{vv'} \quad (2.27)$$

with the dephasing rate:

$$\Gamma_{vv'} = \frac{1}{2}(\gamma_v + \gamma_{v'}) + \hat{\Gamma}_{vv'} \quad (2.28)$$

γ_v is the inverse lifetime for population relaxation of level v , and $\hat{\Gamma}_{vv'}$ is the pure dephasing rate of the vv' transition. For $v = v'$: $\hat{\Gamma}_{vv} = 0$. Equation 2.28 can be rewritten to the well known form $1/T_2 = 1/2T_1 + 1/T_2^*$.

Finally, the polarization is given by the expectation value of the dipole operator V :

$$P(\mathbf{r}, t) = Tr[V\rho(t)] \quad (2.29)$$

The last equation together with the wave equation (2.5) and the Liouville-von Neuman equation (2.25) form the semi-classical coupled Maxwell Liouville equations.

2.4.2 Pump-probe response and Feynman diagrams

For the calculation of the higher order polarizations, it is assumed that the radiation fields are weak in comparison with the fields of the atoms. This enables us to treat the effect perturbatively. The nonlinear response theory provides an expression for the n th order polarization and can be found in textbooks on nonlinear optics [61, 84]. To describe pump-probe signals, it is sufficient to evaluate the third order polarization $P^{(3)}$. It is given by:

$$\begin{aligned}
 P^{(3)}(t) = & \int_0^\infty dt_3 \int_0^\infty dt_2 \int_0^\infty dt_1 S^{(3)}(t_3, t_2, t_1) \\
 & \times E(t - t_1) E(t - t_1 - t_2) \\
 & \times E(t - t_1 - t_2 - t_3)
 \end{aligned} \tag{2.30}$$

with the response function:

$$\begin{aligned}
 S^{(3)}(t_3, t_2, t_1) = & \langle [[[[V(t_1 + t_2 + t_3), V(t_2 + t_3)], V(t_3)], V(0)] \rho(-\infty)] \rangle \\
 & \times \left(\frac{i}{\hbar}\right)^3 \theta(t_1) \theta(t_2) \theta(t_3)
 \end{aligned} \tag{2.31}$$

with $\rho(-\infty)$ the canonical density operator in thermal equilibrium and $\theta(t)$ the Heaviside step function. The polarization at a given time can only depend on the electric fields at earlier times. Therefore, if one of the t_j becomes negative, the response function is zero.

The embedded commutators give rise to the eight so called Liouville-space pathways that contribute to the third-order nonlinear polarization. These pathways can be described by double-sided Feynman diagrams, which we will discuss in detail for pump-probe spectroscopy. The nonlinear response functions can also be written in frequency-domain by Fourier transforms. This leads to Lorentzian lineforms [61, 84] when dealing with homogeneously broadened absorption bands showing mono-exponential relaxation behavior.

As an example, we will now show the third-order nonlinear response function of a three level system. This system consist of a ground state ($v=0$), the first excited state ($v=1$) and the overtone ($v=2$). The anharmonicity Δ is defined by $\Delta = \epsilon_{01} - \epsilon_{12}$, see Figure 2.2.

As stated before, the pump-probe signal depends on the third-order polarization $P^{(3)}$. The required polarization can be set up by different time orderings of the incoming fields, which are either pump or probe fields. The pump-probe signal is acquired in the probe direction, k_2 , which means that, in order to fulfill the phase matching condition, either the pump pulse has two interactions with the sample and the probe only one ($k_2=k_1-k_1+k_2$) or the probe pulse has three interactions and the pump zero

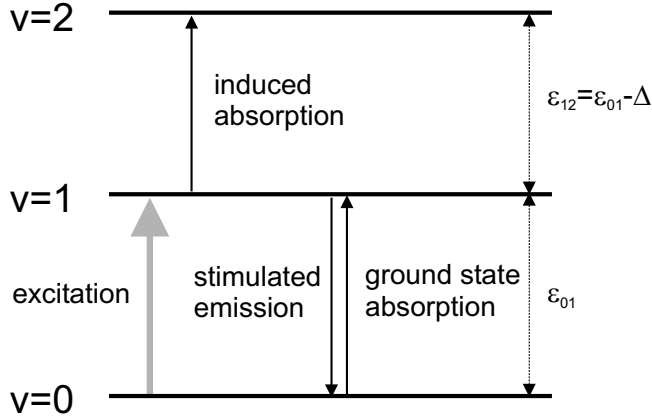


Figure 2.2. Energy levels relevant for pump-probe spectroscopy.

($k_2 = k_2 - k_2 + k_2$). The latter option can be neglected because the probe pulse is much weaker than the pump pulse. The first option gives 6 different time orderings of the incoming fields. These field combinations together with the eight double-sided Feynman diagrams that form the third order response function are shown in Fig. 2.3.

The following rules are connected with the use of the double-sided Feynman diagrams. The density operator is indicated by the two vertical lines, the line on the left represents the ket, the one on the right the bra. Time runs vertically from bottom to top. The arrows represent an interaction with the radiation field. Added to the arrow is the corresponding frequency ω_j . If the arrow points to the right it contributes $\mathcal{E}_j \exp(-i\omega_j t + ik \cdot r)$ to the polarization. An arrow pointing to the left contributes $\mathcal{E}_j^* \exp(i\omega_j t - ik \cdot r)$. Each diagram has an overall sign $(-1)^n$, where n is the number of interactions from the right. The overall frequency of the term is the sum of the three frequencies with their appropriate signs. The last interaction stems from $Tr(\rho V)$ and is therefore represented by a dashed line. An ingoing arrow represents a photon absorption, an outgoing arrow photon emission.

Diagram R_1 represents stimulated emission. Two combinations of incoming fields are responsible for the R_1 contribution to $P^{(3)}$: $1*12$ (pump-pump-probe) in which the pump pulse interacts twice with the sample, before the probe pulse arrives, and $1*21$ (pump-probe-pump), which will only give a contribution when the pump and probe pulses overlap in time. The diagram shows the creation of population in the excited state. If different levels are excited, say $|1\rangle$ and $\langle 1'|$ when there are two or more oscillators present, the diagrams implies the creation of a coherence, as will be shown in Chapter 9. Diagram R_4 also represents stimulated emission, generated

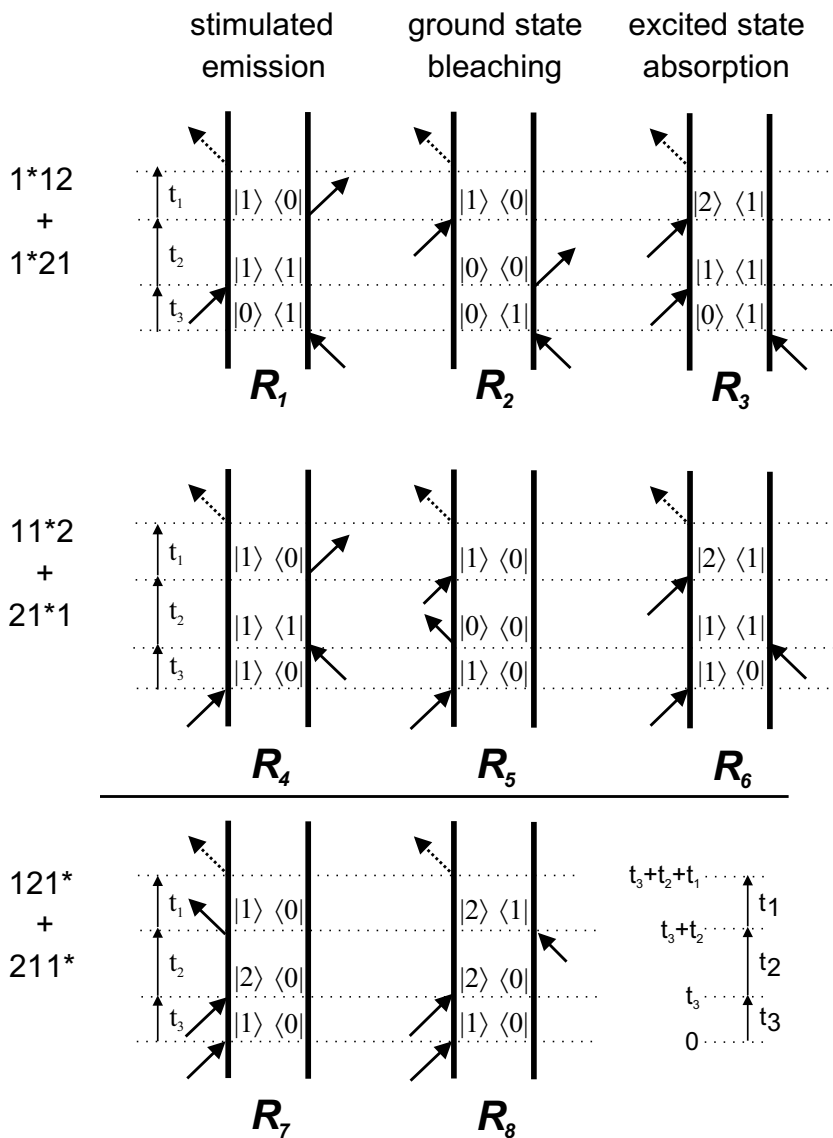


Figure 2.3. Feynman diagrams for pump-probe spectroscopy.

by a different time ordering. Diagrams R_2 and R_5 describe ground state bleaching, while R_3 and R_6 describe excited state absorption. The 1*21 and 21*1 interactions with diagrams R_1 - R_6 describe the generation of a population grating by the pump and probe pulse. The second interaction with the pump leads to diffraction in the direction of the probe, leading to a contribution to the coherent artifact. Clearly, this contribution is only non-zero, when pump and probe pulse overlap in time (provided that the absorption bands are broader than the pulse spectrum) [31]. Time orderings 121* and 211* with diagrams R_7 and R_8 describe a third order polarization generated via a coherence of the $v = 0$ and $v = 2$ state. This signal is only present when pump and probe overlap in time and also contributes to the coherent artifact.

Following the rules for the use of these Feynman diagrams we get the following response functions:

$$R_1(t_3, t_2, t_1) = |\mu_{01}|^4 e^{i\epsilon(t_3-t_1)} e^{-(t_1+t_3)/T_2-t_2/T_1} \quad (2.32)$$

$$R_2(t_3, t_2, t_1) = |\mu_{01}|^4 e^{i\epsilon(t_3-t_1)} e^{-(t_1+t_3)/T_2-t_2/T_1} \quad (2.33)$$

$$R_3(t_3, t_2, t_1) = -|\mu_{01}|^2 |\mu_{12}|^2 e^{i\epsilon(t_3-t_1)} e^{i\Delta t_1} e^{-(t_1+t_3)/T_2-t_2/T_1} \quad (2.34)$$

$$R_4(t_3, t_2, t_1) = |\mu_{01}|^4 e^{-i\epsilon(t_1+t_3)} e^{-(t_1+t_3)/T_2-t_2/T_1} \quad (2.35)$$

$$R_5(t_3, t_2, t_1) = |\mu_{01}|^4 e^{-i\epsilon(t_1+t_3)} e^{-(t_1+t_3)/T_2-t_2/T_1} \quad (2.36)$$

$$R_6(t_3, t_2, t_1) = -|\mu_{01}|^2 |\mu_{12}|^2 e^{-i\epsilon(t_1+t_3)} e^{i\Delta t_1} e^{-(t_1+t_3)/T_2-t_2/T_1} \quad (2.37)$$

$$R_7(t_3, t_2, t_1) = |\mu_{01}|^2 |\mu_{12}|^2 e^{-i\epsilon(t_3+2t_2+t_1)} e^{i\Delta t_2} e^{-(t_3+t_1)/T_2-t_2/T_{2,02}} \quad (2.38)$$

$$R_8(t_3, t_2, t_1) = -|\mu_{01}|^2 |\mu_{12}|^2 e^{-i\epsilon(t_3+2t_2+t_1)} e^{i\Delta(t_2+t_3)} e^{-(t_3+t_1)/T_2-t_2/T_{2,02}} \quad (2.39)$$

where Δ is the anharmonicity, μ_{ij} the transition dipole moment between state i and j , $T_2 = T_{2,01} = T_{2,12}$ the dephasing time of the $0 \rightarrow 1$ and $1 \rightarrow 2$ transition, $T_{2,02}$ is the dephasing time of the $0 \rightarrow 2$ coherence, T_1 is the vibrational lifetime of the population. Furthermore, $\epsilon = \epsilon_{01}$, $\epsilon_{12} = \epsilon_{01} - \Delta = \epsilon - \Delta$. In the above equations we have assumed that the dephasing time of the $1 \rightarrow 2$ transition is the same as for the $0 \rightarrow 1$ transition. These response functions can be grouped together:

$$\sum_{l=1}^3 R_l = |\mu_{01}|^2 e^{i\epsilon(t_3-t_1)} [2|\mu_{01}|^2 - |\mu_{12}|^2 e^{i\Delta t_1}] e^{-(t_1+t_3)/T_2-t_2/T_1} \quad (2.40)$$

$$\sum_{l=4}^6 R_l = |\mu_{01}|^2 e^{-i\epsilon(t_1+t_3)} [2|\mu_{01}|^2 - |\mu_{12}|^2 e^{i\Delta t_1}] e^{-(t_1+t_3)/T_2-t_2/T_1} \quad (2.41)$$

$$\sum_{l=7}^8 R_l = |\mu_{01}|^2 |\mu_{12}|^2 e^{-i\epsilon(t_3+2t_2+t_1)} e^{i\Delta t_2} [e^{i\Delta t_3} - 1] e^{-(t_1+t_2+t_3)/T_{2,02}} \quad (2.42)$$

From the above expression it is clear that in case of an harmonic oscillator, i.e. $\Delta=0$ and $|\mu_{12}|^2=2|\mu_{01}|^2$, all nonlinear response functions vanish.

The third-order polarization in the direction of the probe is given by the convolution of the response functions with the E-fields:

$$\begin{aligned}
 P^{(3)}(k_2, t) \propto & \int_0^\infty dt_1 \int_0^\infty dt_2 \int_0^\infty dt_3 \\
 & [\mathcal{E}_2(t-t_1)e^{-i\omega_2(t-t_1)}\mathcal{E}_1(t-t_1-t_2)\mathcal{E}_1^*(t-t_1-t_2-t_3) \\
 & \times e^{-i\omega_1 t_3} \\
 & + \mathcal{E}_1(t-t_1)\mathcal{E}_2(t-t_1-t_2)e^{-i\omega_2(t-t_1-t_2)}\mathcal{E}_1^*(t-t_1-t_2-t_3) \\
 & \times e^{-i\omega_1(t_2+t_3)}] \\
 & \times \sum_1^3 R_i(t, t_1, t_2, t_3) + \\
 & [\mathcal{E}_2(t-t_1)e^{-i\omega_2(t-t_1)}\mathcal{E}_1^*(t-t_1-t_2)\mathcal{E}_1(t-t_1-t_2-t_3)e^{i\omega_1 t_3} \\
 & + \mathcal{E}_1(t-t_1)\mathcal{E}_1^*(t-t_1-t_2)e^{-i\omega_1 t_2}\mathcal{E}_2(t-t_1-t_2-t_3) \\
 & \times e^{-i\omega_2(t-t_1-t_2-t_3)}] \\
 & \times \sum_4^6 R_i(t, t_1, t_2, t_3) + \\
 & [\mathcal{E}_1^*(t-t_1)\mathcal{E}_2(t-t_1-t_2)e^{-i\omega_2(t-t_1-t_2)} \\
 & \times \mathcal{E}_1(t-t_1-t_2-t_3)e^{i\omega_1(t_2+t_3)} \\
 & + \mathcal{E}_1^*(t-t_1)\mathcal{E}_1(t-t_1-t_2)e^{i\omega_1 t_2} \\
 & \times \mathcal{E}_2(t-t_1-t_2-t_3)e^{-i\omega_2(t-t_1-t_2-t_3)}] \\
 & \times \sum_7^8 R_i(t, t_1, t_2, t_3) + \text{c.c.} \tag{2.43}
 \end{aligned}$$

The transmission change ΔT can be calculated as the ratio between the intensity of the probe pulse with and without interaction of the pump pulse [92]:

$$\frac{T}{T_0} \propto \int \frac{|\mathcal{E}_2(t) + iP^{(3)}(t)|^2}{|\mathcal{E}_2(t)|^2} dt \approx 1 - \frac{2\text{Im} \int dt P^{(3)} \mathcal{E}_2}{|\mathcal{E}_2|^2} \propto \text{Im} \int dt P^{(3)} \mathcal{E}_2 \tag{2.44}$$

In the above formula, we have added the out of phase component of the nonlinear polarization to the E-field. Pump-probe spectroscopy is usually performed with resonant frequencies. Therefore the real part of the susceptibility is zero, and only the out-of-phase component of the nonlinear polarization has to be taken into account.

This equation together with the nonlinear polarizations describes the measured pump-probe signal.

In practice, many of the total of 16 pathways can be neglected. Time orderings in which the probe pulse precedes the pump pulse, will only give a signal for negative delay times, while other interaction orderings only contribute when the pump and probe pulses overlap. The ordinary pump-probe signal is described by diagrams R_1 - R_6 with time orderings 1^*12 and 11^*2 .

The anharmonicity combined with the spectral width of the pulses applied in a one-color experiment ($\omega_1 = \omega_2$) determine whether the $1 \rightarrow 2$ transition can be reached by the same pulses that excite the $0 \rightarrow 1$ transition. If not, the excited state absorption diagrams can be disregarded, in this case. They should be taken into account, however, in a two-color pump-probe experiment where $\omega_1 \neq \omega_2$.

In Chapter 9, we will address a system in which pump pulses have such a large spectral width that they excite two different oscillators, which have their resonance frequency within the pulse. In this case, the response function will show oscillatory terms stemming from quantum beats.

2.5 Pump-probe spectroscopy

The description of the pump-probe signal can be simplified for some experiments described in this thesis. We assume that pump and probe pulse are only resonant with one transition in the molecule. Furthermore, the time scale of the relaxation is comparable or longer than the pulse duration.

In this case the transmission of a probe pulse at time t after excitation is given by the following convolution [2]:

$$T(t) = \int dt' I_{probe}(t-t') e^{-\alpha(t')} \quad (2.45)$$

where I_{probe} is the input probe energy and $\alpha(t)$ the transient absorption. The absorption can be written as:

$$\alpha(t) = \alpha_0 [1 - 2f_e \int_0^\infty dt'' I_{pump}(t-t'') e^{-t''/T_1}] \quad (2.46)$$

where $\alpha_0 = n\sigma_{01}L$ is the equilibrium absorbance with n the density of oscillators, σ_{01} the absorption cross section of the $\nu=0 \rightarrow \nu=1$ transition and L the optical path length. The part of the molecules that is excited by the pump pulse is indicated by f_e . The relaxation process is assumed to be single exponential with characteristic time T_1 . The factor 2 in the above formula stems from the fact that the absorption change depends on the population difference between the ground and excited state. Or, in other words, the bleaching signal depends both on absorption from the ground state and on stimulated emission from the excited state to the ground state, as indicated

in Figure 2.2. In a pump-probe measurement the transmission of a probe pulse is measured with and without excitation pulse. In the latter case the probe pulse transmission reads $T_0(t) = \int dt' I_{probe}(t-t')e^{-\alpha_0}$. Assuming that the induced absorption changes are small, it follows that:

$$\frac{T(t)}{T_0} = \frac{\int dt' I_{probe}(t-t')e^{-\alpha_0} [1 + 2f_e \alpha_0 \int_0^\infty dt'' I_{pump}(t-t'')e^{-t''/T_1}]}{\int dt' I_{probe}(t-t')e^{-\alpha_0}} \quad (2.47)$$

This expression can be rearranged to:

$$\ln \frac{T(t)}{T_0} = \ln \left(1 + \frac{\int dt' \int_0^\infty dt'' I_{probe}(t-t') I_{pump}(t-t'') e^{-\alpha_0} 2f_e \alpha_0 e^{-t''/T_1}}{\int dt' I_{probe}(t-t') e^{-\alpha_0}} \right) \quad (2.48)$$

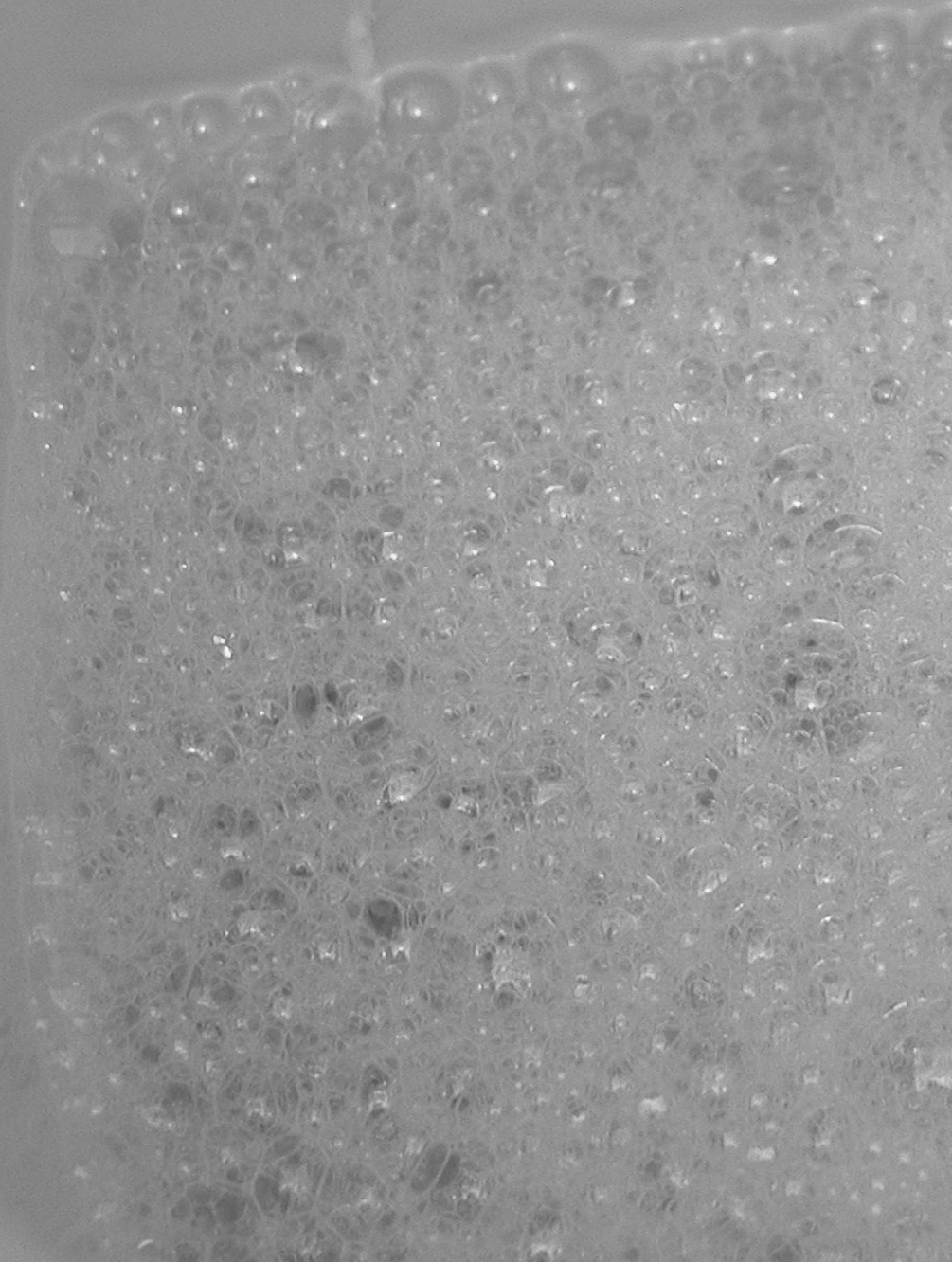
It now follows that:

$$\ln \frac{T(t)}{T_0} \propto \int dt' \int_0^\infty dt'' I_{probe}(t-t') I_{pump}(t-t'') e^{-\alpha_0} 2f_e \alpha_0 e^{-t''/T_1} \quad (2.49)$$

The measured signals can thus be described by the convolution of both the pump and probe pulse with the supposed relaxation behavior. In other words, the relaxation behavior is convolved with the cross correlation of the pump and the probe pulse.

3 Experimental

Wave coupling in a nonlinear medium, described in the previous chapter, can not only be used for nonlinear spectroscopy studies, but also for the generation of light pulses in the infrared. Here, we show how the incident and generated E-fields are intertwined and under what conditions energy transfer among waves is efficient. The second part of this chapter gives a description of the experimental setup used for the pump-probe experiments.



3.1 Nonlinear optical interactions in crystals

There are no laser sources that directly emit intense and ultrashort (fs) laser pulses at wavelengths in the mid-infrared region. The experimentalist is, therefore, forced to search for other methods to generate light with wavelengths around $3 \mu\text{m}$. The general way is to make use of the nonlinear polarization that is generated in certain materials under the influence of intense light, as shown in the previous chapter. In particular, three wave mixing processes, in which two incoming fields generate a nonlinear polarization $P^{(2)}$, that acts as a source for a new, third E-field, are used to generate infrared pulses. The second order nonlinear polarization generated by the fields E_i and E_j is given by:

$$P^{(2)}(k, \omega) = \epsilon_0 \chi^{(2)}(\omega = \omega_i + \omega_j, k = k_i + k_j) : E(k_i, \omega_i) E(k_j, \omega_j) \quad (3.1)$$

where $\chi^{(2)}$ is the frequency and wavevector dependent second-order susceptibility. We describe the E-fields by:

$$E_i(z, t) = \mathcal{E}_i(z, t) e^{ik_i z - i\omega_i t} \quad (3.2)$$

for $i = 1, 2, 3$. \mathcal{E}_i represents the pulse envelope function. As shown in the previous chapter, the newly generated E-field obeys the wave equation (2.18):

$$\left(\frac{\partial}{\partial z} + \frac{1}{v_g} \frac{\partial}{\partial t} \right) \mathcal{E}(z, t) e^{ikz - i\omega t} = \frac{1}{2i\epsilon_0 k c^2} \frac{\partial^2 P^{(2)}}{\partial t^2} \quad (3.3)$$

If we make use of the slowly varying amplitude approximation (see section 2.3) for the term on the right-hand side, and fill in Eq. 3.1 and 3.2, we get the following coupled wave equations:

$$\left(\frac{\partial}{\partial z} + \frac{1}{v_g} \frac{\partial}{\partial t} \right) \mathcal{E}_1 e^{ikz - i\omega t} = \frac{\chi^{(2)}(\omega_1 = \omega_3 - \omega_2)}{2n_1 c} e^{i\Delta k z} (i\omega_1 \mathcal{E}_2^* \mathcal{E}_3 - 2 \frac{\partial}{\partial t} (\mathcal{E}_2^* \mathcal{E}_3)) \quad (3.4)$$

$$\left(\frac{\partial}{\partial z} + \frac{1}{v_g} \frac{\partial}{\partial t} \right) \mathcal{E}_2 e^{ikz - i\omega t} = \frac{\chi^{(2)}(\omega_2 = \omega_3 - \omega_1)}{2n_1 c} e^{i\Delta k z} (i\omega_3 \mathcal{E}_1^* \mathcal{E}_3 - 2 \frac{\partial}{\partial t} (\mathcal{E}_1^* \mathcal{E}_3)) \quad (3.5)$$

$$\left(\frac{\partial}{\partial z} + \frac{1}{v_g} \frac{\partial}{\partial t} \right) \mathcal{E}_3 e^{ikz - i\omega t} = \frac{\chi^{(2)}(\omega_3 = \omega_1 + \omega_2)}{2n_1 c} e^{-i\Delta k z} (i\omega_3 \mathcal{E}_1 \mathcal{E}_2 - 2 \frac{\partial}{\partial t} (\mathcal{E}_1 \mathcal{E}_2)) \quad (3.6)$$

$\Delta k = k_3 - k_2 - k_1$, the wave vector mismatch. In these equations, two fields generate a nonlinear polarization that is a source for the third field.

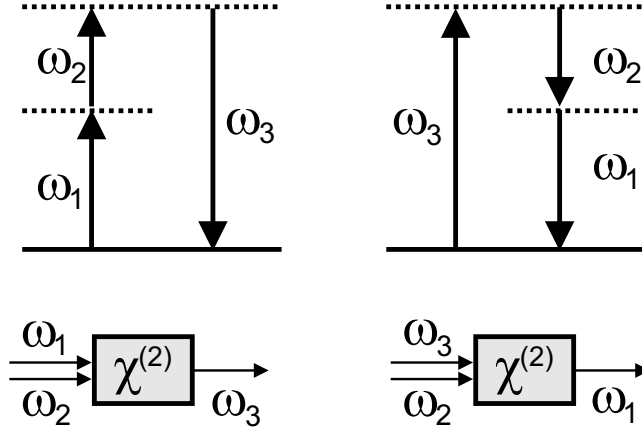


Figure 3.1. Energy level description of sum (left) and difference frequency generation and outline of the beams in the crystals.

The processes involved in a three wave mixing process are depicted in Figure 3.1. If the incoming fields are identical, i.e. $\omega_1 = \omega_2$, the generated $\omega_3 = 2\omega_1$ wave is the second harmonic of the input beam. More general is the sum frequency generation (SFG) process where two different photons add up to a new field at $\omega_3 = \omega_1 + \omega_2$. Alternatively, two incoming fields ω_3 and ω_2 can generate a field at ω_1 (difference frequency generation, DFG) following the energy conservation condition $\omega_3 = \omega_1 + \omega_2$. Because the DFG process leads to an increase in the number of photons with frequency ω_1 , it is also known under the name optical parametrical amplification (OPA).

The two-photon emission may even occur when the ω_1 and ω_2 fields are not initially present. In this case, the zero-point fluctuations of the electric field, which arise in the quantum description of light, are responsible for the spontaneous birth of an ω_1 , ω_2 couple of photons. The lower of the two frequencies is called the idler, the higher of the two the signal pulse. As soon as some of the photons are generated at the right frequencies, they are amplified by means of OPA. This process is known as parametric superfluorescence [33, 53] and forms the basis of the OPG/OPA stages discussed in the next section.

The generation of electric fields at new frequencies does not only depend on the energy conservation law, but, in order to be efficient, also on the phase matching condition. Only when $\Delta k = 0$, constructive interference of the three waves over a longer propagation length will occur. For perfect phase-matching of collinear beams, the phase-matching condition reads:

$$n_1\omega_1 + n_2\omega_2 = n_3\omega_3 \quad (3.7)$$

It is clear that this condition together with energy conservation ($\omega_3 = \omega_1 + \omega_2$) can never be fulfilled in ordinary dispersive materials, for which the refractive index increases with ω . Birefringent crystals, i.e. crystals for which the refractive index differs for different polarizations of the incoming light can solve this problem. Most crystals used for nonlinear optics are uniaxial crystals having two indices of refraction, n_o , the ordinary refractive index, for polarizations orthogonal to the plane containing the wavevector k and the optical axis of the crystal, and $n_e(\theta)$, the extraordinary refractive index, for polarizations parallel to this plane. If the highest frequency wave ω_3 is polarized in the direction that gives the lower of the two refractive indices, the ordinary dispersion can be compensated and phase-matching is possible.

Uniaxial crystals are divided in positive ($n_e > n_o$) and negative ($n_e < n_o$) uniaxial crystals. Furthermore, difference is made between type I, type II and type III phase matching. Type I phase matching stands for the situation where the two lower frequency waves (ω_1 and ω_2) have the same polarization, perpendicular to the pump; in type II phase matching the signal polarization is perpendicular to pump and idler and in type III phase matching the idler polarization is perpendicular to pump and signal. The phase-matching condition is fulfilled by changing the orientation of the crystal with respect to the propagation direction of the incident light. It can be shown that light polarized in the plane containing k and the crystal axis, experiences an extraordinary refractive index [113]:

$$\frac{1}{n_e(\theta)^2} = \frac{\sin^2\theta}{\bar{n}_e^2} + \frac{\cos^2\theta}{\bar{n}_o^2} \quad (3.8)$$

with \bar{n}_e the principal value of the extraordinary refractive index. By changing the angle θ , a value of $n_e(\theta)$ can be chosen such that the phase-matching condition is fulfilled.

3.2 Setup for femtosecond mid-infrared pump-probe spectroscopy

This section describes the generation of mid-infrared pulses that are resonant with the OH-stretch vibrational modes of hydrogen-bonded liquids and short enough to follow their dynamics [15]. Furthermore, a description of the pump-probe setup and the preparation of the samples is given .

3.2.1 Generation of mid-infrared laser pulses

The basis of our setup is formed by a commercial regenerative amplifier system (Quantronix Titan). The RGA is seeded by 800 nm light from a Ti:Sapphire oscilla-

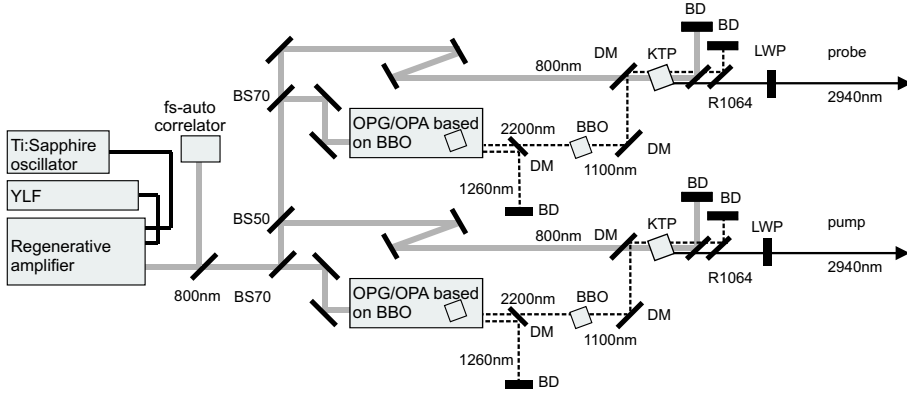


Figure 3.2. The experimental setup used for the generation of femtosecond mid-infrared pulses. For a description of the setup see text. BS70: beam splitter reflection 70%; DM: dichroic mirror; BD: beam dump; R1064: Nd:YAG mirror; LWP: long wave pass filter; BBO and KTP: crystals; black bars without name: dielectric 800 nm mirrors

tor (Spectra Physics Tsunami) pumped by a Millennia (Spectra Physics). The seed pulses are centered around 800 nm and have a spectral width of 14 nm (FWHM). In the Titan system, they are first stretched in time and then amplified in a Ti:Sapphire crystal by means of 527 nm light from a Nd:YLF-laser. As a last step before the compression of the pulses, they pass a Multipass Amplifier (MPA), based on Ti:Sapphire and also pumped by part of the Nd:YLF light. The generated 800 nm pulses have a duration of 130 fs, a repetition rate of 1 kHz and a pulse energy of 3 mJ. A beam sampler sends a small part of the outcoming light to a femtosecond autocorrelator to measure the pulse duration.

The 800 nm pulses are split into a probe and a pump part by means of a beam-splitter directly after the regenerative amplifier. To generate the mid-infrared pump pulses, a commercial 5-pass OPG/OPA stage (TOPAS) is used. This stage is based on a BBO crystal and generates signal and idler pulses that are tunable between 1 and 2.6 μm . This is a type II phase-matching process, implying that the polarization of the signal is perpendicular to that of the idler and the pump. The total energy of the generated pulses is approximately 250 μJ . An 800 nm filter inside the TOPAS blocks the remaining pump light. Typical wavelengths for signal and idler pulses, are 1260 and 2200 nm, respectively.

The idler pulses are separated from the signal pulses by a dichroic mirror and subsequently frequency-doubled in a second BBO-crystal. The resulting 1100 nm light is mixed with a fresh part of the 800 nm beam in a difference frequency generation

process in a KTiOPO_4 (KTP) crystal, giving pulses with a central wavelength near $3 \mu\text{m}$. The unwanted wavelengths are subsequently filtered out by different filters: an 800 nm mirror reflects the remaining pump light, a Nd:YAG-mirror (1064 nm) reflects the 1100 nm light, and finally a long wave pass filter filters out residual light at all wavelengths shorter than 2500 nm.

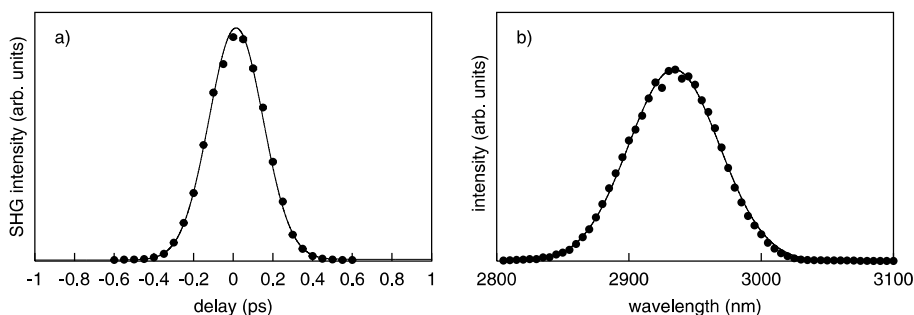


Figure 3.3. Cross correlation trace of pump and probe measured with a LiIO_3 -crystal (a), and a typical power spectrum of an infrared pulse (b). The fitted curves are Gaussians with a FWHM of 330 fs and 80 nm, respectively.

The probe pulses are generated in the same way, but with less pump energy. The TOPAS is a three-pass OPG/OPA-stage, giving about $140 \mu\text{J}$ of energy for signal plus idler. Due to the use of two different OPG/OPA-stages the wavelengths of the pump and probe pulses can be tuned independently. The pulses can be tuned between 2700–3300 nm ($3000\text{--}3700 \text{ cm}^{-1}$). Figure 3.3 shows typical pulse characteristics. In the left part, pump and probe pulses were crossed under a small angle in a LiIO_3 to generate the sum-frequency. The intensity of the SFG signal is measured as a function of delay time between pump and probe pulse. Assuming Gaussian time profiles, the duration of the generated infrared pulses is $330/\sqrt{2}=230$ fs. The spectral width of the pulses is 80 nm (FWHM), which is sufficiently small in comparison with the absorption bandwidth of the OH-stretch vibration in pure water (400 nm) to enable the probing of different spectral regions. Typical energies are $20 \mu\text{J}$ for the pump and $\leq 1 \mu\text{J}$ for the probe.

3.2.2 Two color pump-probe setup

Figure 3.4 shows the pump-probe setup. The pump pulse is focussed by a CaF_2 lens on the sample to excite part of the molecules and is blocked afterwards by a beam block. The probe pulses pass a delay-line and are focussed and overlapped with the pump focus in the sample. To assure that the probe pulses monitor a homogeneously

excited part of the sample, lenses with different focal lengths are used to focus pump and probe. In this way a larger focus for the pump pulse was achieved. The typical sizes of the foci of pump and probe pulses are 200 and 75 μm , respectively. To avoid thermal lensing effects, we collimate and focus the probe beam on a PbSe-detector.

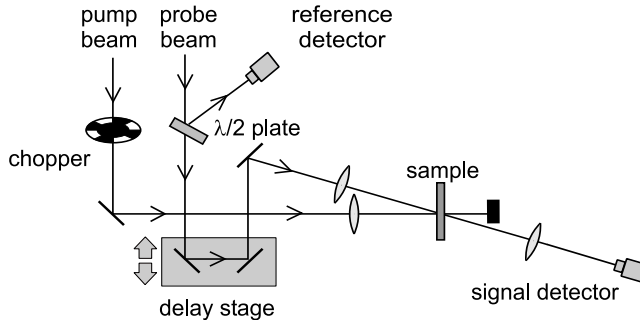


Figure 3.4. Pump-probe setup, for description see text.

The intensity of the probe beam I is measured with a PbSe-detector as a function of delay between pump and probe pulses. In order to compensate for the pulse to pulse intensity fluctuations in the probe beam, we use a single detector to measure the reference intensity I_{ref} . Using a chopper, both the transmission of the probe beam in the presence of the pump beam (T) and in the absence of the pump beam (T_0) are measured. The transmission change $\ln(T/T_0)$ is calculated as a function of delay between pump and probe pulse, where $T=I/I_{\text{ref}}$ and $T_0=(I_0/I_{\text{ref}})$.

To cancel the effect of orientational relaxation on the observed dynamics and to probe only the vibrational relaxation, the polarization of the probe pulse is set at the magic angle (54.7°) with respect to the polarization of the pump pulse [24] by means of a zero-order $\lambda/2$ plate. If the orientational dynamics is measured, the probe polarization is set at an angle of 45° with respect to the pump polarization. In this case, a polarizer is placed after the sample, which enables the measurement of the transmission changes for the probe polarization parallel to the pump polarization ($(T/T_0)_\parallel$) and perpendicular to the pump polarization ($(T/T_0)_\perp$). The rotational anisotropy is calculated [24] as follows:

$$R(t) = \frac{\ln(T/T_0)_\parallel - \ln(T/T_0)_\perp}{\ln(T/T_0)_\parallel + 2\ln(T/T_0)_\perp} \quad (3.9)$$

The denominator represents the rotation free signal and is the same as the signal measured with magic angle polarization.

To avoid the accumulation of heat from pump pulses during the experiment, the sample was rotated. In this way, every pump pulse sees a fresh part of the sample.

We use a nitrogen flow box when pump and probe pulses have frequencies between 3600–3900 cm^{-1} . In this spectral region, rovibrational transitions of gas-phase water molecules present in air lead to the absorption of the ir-light. Without nitrogen flow box, the intensity of the ir-pulses decreases and their power spectrum show dips corresponding to the rovibrational transitions. The nitrogen box provides a water-poor environment.

3.3 Sample preparation

The linear absorption spectra were measured using a Perkin-Elmer spectrometer. The transmittance of the sample was calculated by dividing the intensity of the light with ($I(z)$) and without (I_0) sample. As shown in the previous chapter, the Lambert-Beer law applies for this situation:

$$T = I(z)/I_0 = e^{-\sigma_{01}(\omega)\rho_0 z}, \quad (3.10)$$

where ρ_0 is the density of the absorbers and σ_{01} the absorption cross section. The samples used in this thesis consist of a thin layer of liquid in between two sapphire or CaF_2 windows. Depending on the density of OH-groups different, spacers are used. For a dilution of pinacol molecules, for example, a spacer of 500 μm was used, whereas for liquid water the number of OH-groups was too high to use the thinnest spacer available (15 μm). In that case, we pressed the two windows to a separation of a few μm in order to get a transmission of approximately 10% at the OH-stretch absorption peak, which is a typical value for most samples used.

4

Temperature Dependence of Vibrational Relaxation in Liquid H₂O

We have determined the lifetime of the OH-stretch vibration in pure liquid water as a function of temperature using femtosecond mid-infrared pump-probe spectroscopy. The lifetime T_1 increases from 260 ± 18 fs at $T = 298$ K to 320 ± 18 fs at $T = 358$ K. The increase in lifetime with temperature can be quantitatively explained from the decrease in overlap between the OH-stretch vibration and the overtone of the H-O-H bending mode.

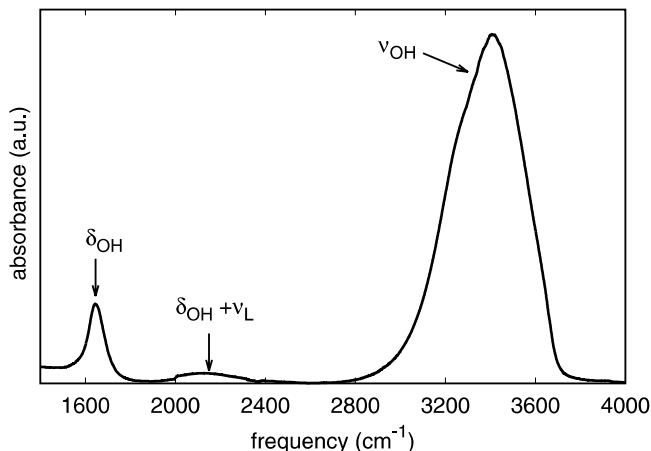


Figure 4.1. The linear absorption spectrum of liquid water in the mid-infrared region showing three peaks: the symmetric and antisymmetric stretch bands around 3400 cm^{-1} (ν_{OH}), the bending mode (δ_{OH}) at about 1640 cm^{-1} , and a small combination band of the bending mode with the librational mode ($\delta_{\text{OH}}+\nu_{\text{L}}$) at 2150 cm^{-1} .

4.1 Introduction

Infrared spectroscopy is a key tool in understanding the structure and composition of gas phase molecules, liquids, biomolecules and peptides. An additional tool is the use of isotopic substitution, which allows for a separation of groups that are otherwise very similar. For the study of the vibrations in liquid water, for example, an often used isotopic variation is HDO molecules dissolved in D₂O (HDO:D₂O) [17, 18, 100]. At low HDO concentrations, this system makes it possible to observe the behavior of an isolated OH-group, because the normal mode vibrations of the surroundings do not have spectral overlap with that of the OH-group.

As shown in Chapter 1, the H₂O molecule has three normal mode vibrations [35]: for an isolated molecule in the gas phase the asymmetric stretch vibration ν_3 has a frequency of 3756 cm^{-1} , the symmetric stretch vibration ν_1 has a frequency of 3657 cm^{-1} and the bending mode ν_2 has a frequency of 1595 cm^{-1} . The positions and shapes of the vibrational bands change when going from the gas to the liquid phase, mainly due to hydrogen bonding. The mid-infrared absorption spectrum of liquid H₂O is depicted in Figure 4.1. The spectral position of these bands changes due to hydrogen bonding: the two stretch modes undergo a red shift and overlap to form a band centered around 3400 cm^{-1} with a FWHM of about 400 cm^{-1} . The bending mode undergoes a blue shift towards 1643.5 cm^{-1} . Due to the broad distribution of hydrogen bond lengths in liquid water, the lines become bands. In Figure 4.1, there

is a third band centered around 2150 cm^{-1} that has been assigned to a combination tone of the bend mode and the librational band (500 cm^{-1}) [55, 56]. For HDO:D₂O the situation is completely different: there is no symmetric and antisymmetric normal mode, but an OH-stretch and an OD-stretch mode. The OH-stretch band lies at 3400 cm^{-1} , the OD-stretch band at 2500 cm^{-1} , and the HOD bending mode at 1450 cm^{-1} .

Information on the mechanism of vibrational relaxation can be obtained by studying its temperature dependence. The general trend for the temperature dependence of the vibrational relaxation rate is that the rate increases with temperature, i.e. the lifetime gets shorter as the temperature gets higher. This has been theoretically described for the so-called vibron-phonon system, for which a distinction is made between the excited high frequency vibrational mode and the accepting low-frequency phonon modes [50]. Raising the temperature leads to an increase of the occupation in the low-frequency accepting modes, causing a stronger anharmonic interaction between the donor and acceptor modes, which results in a shorter lifetime. The predicted decrease of the lifetime has experimentally been confirmed for various systems. The OH-groups in fused silica [34] show a decrease in relaxation time from 110 ps at 100 K to about 15 ps for 1450 K. For liquid hydrogen chloride [8] the lifetimes are 2.1 and 1.0 ns at $T = 173$ and 248 K, respectively. The lifetime of the SH-stretch mode in an As₂S₃ glass [32] decreases from 2.0 to about 0.58 ps when going from 5 to 300 K.

In view of the above, it is surprising that the OH-stretch vibration of HDO:D₂O shows a different behavior [108]. Below the solid-liquid phase transition, there is no significant temperature dependence of the lifetime. At the transition, the lifetime T_1 jumps from 384 ± 16 to 745 ± 47 fs. Increasing the temperature in the liquid phase leads to a further increase of the lifetime to 900 fs. The explanation for this anomalous behavior is that the average hydrogen bond strength decreases with temperature. Staib and Hynes made a theoretical study on the vibrational relaxation of the OH-stretch vibration of an O-H···O group [88]. They calculated the anharmonic interaction between the OH-stretch mode and the hydrogen bond stretch mode (200 cm^{-1}), as a result of which the energy is transferred to the hydrogen bond mode. With increasing temperature, the hydrogen bonds become weaker, which leads to a decrease of the anharmonic interaction and thus to an increase of the vibrational lifetime.

Another method to unravel the relaxation scheme is the detection of the intermediate level directly, as has been done by Deàk et al. [12]. Using time-resolved anti-Stokes Raman scattering on the OH-stretch vibration of HDO:D₂O and of pure H₂O, a strong response of the bending mode for pure H₂O was observed and a weaker response of the same mode for HDO:D₂O. These observations do not exclude, however, that the hydrogen bond stretch mode still plays a role in the relaxation. It is therefore interesting to measure the lifetime of the OH-stretch vibration in liquid H₂O as a function of temperature, in addition to the study performed by Deàk et al. [12], in which all experiments were performed at room temperature and the time resolution

was insufficient to extract the time scale of the relaxation.

4.2 Experimental

In the experiment, the OH-stretch vibration of a subset of water molecules is excited to the $\nu_{\text{OH}} = 1$ state with an intense femtosecond mid-infrared pulse. This excitation leads to a bleaching of the $0 \rightarrow 1$ transition and to an induced absorption of the $1 \rightarrow 2$ transition, which is red-shifted by about 300 cm^{-1} with respect to the $0 \rightarrow 1$ transition [25]. The dynamics of the excitation are measured with time-delayed probe pulses by measuring the transmission change as a function of time.

The experimental setup is described in Chapter 3, here we just focus on the aspects that are important for the results obtained. The probe polarization was set at the magic angle with respect to the polarization of the pump pulse by means of a zero-order $\lambda/2$ plate, to rule out the effects of orientational relaxation [24]. To avoid thermal lensing effects, we collimate and focus the probe beam on the PbSe-detector. The sample used was a thin layer of pure liquid water (Aldrich, HPLC grade) in between two sapphire windows. The transmission at the center of the OH-stretch absorption band was a few percent typically. The transmission through a pinhole with a $100 \mu\text{m}$ diameter was 80% for the probe and 50% for the pump. The excitation by the pump eventually leads to a local increase in temperature. From the linear absorption spectrum and from the measured relative change in transmission, $\ln(T/T_0) = 0.1$ typically, we deduce a value for the single-pulse temperature increase of approximately 30 K. In order to avoid the accumulation of heat, the sample is rotated.

4.3 Results

Pump-probe scans for a pump frequency of 3250 cm^{-1} and eight different probe frequencies are displayed in Figure 4.2. In these scans, the final level of transmission is observed to be increased or decreased, depending on the probe frequency. This observation can be explained from the increase in temperature that results after the thermalization of the excitation. The behavior at short delay times also depends on the probe frequency. When probing at the red side of the absorption band (upper two curves in the left panel of Figure 4.2), an induced $\nu_{\text{OH}} = 1 \rightarrow 2$ absorption is observed. When probing at the blue side of the absorption band (upper two curves in the right panel), a clear bleaching peak around $t = 0$ is observed. Near the center of the absorption band (lower two curves in the left panel), this peak is hidden under the thermalization effect. Next to these two effects, i.e. the long-time transmission increase or decrease and the bleaching or induced absorption peak around $t = 0$, there is a coherent interaction. This effect is most clearly observed at the two most blue probing wavelengths. Around $t = 0$ the transmission change shows a wiggle, which is negative for $t < 0$ and positive for $t > 0$. At a wavelength of 3200 cm^{-1} the

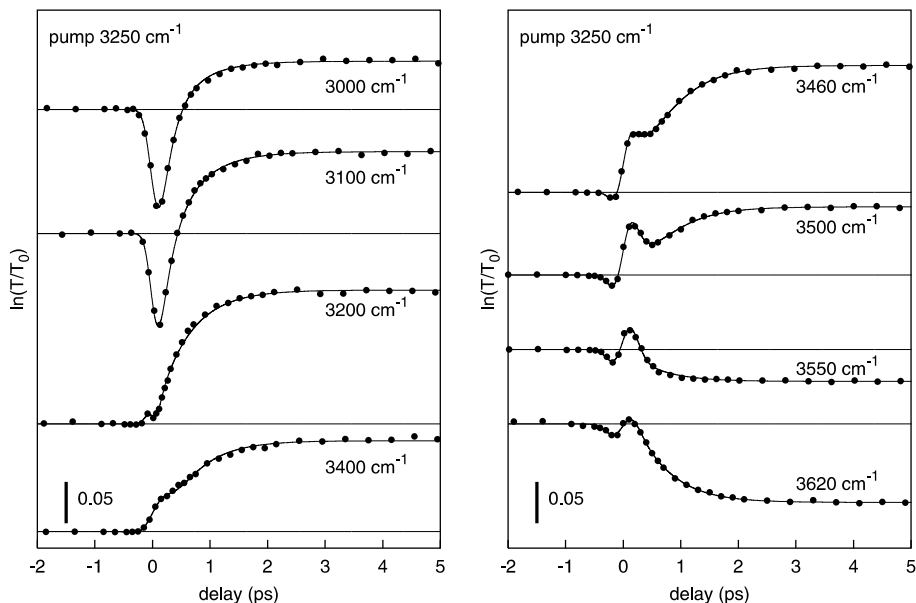


Figure 4.2. Pump-probe scans for different probe frequencies at $T = 298$ K. The pump frequency was 3250 cm^{-1} .

situation is reversed: positive for $t < 0$ and negative for $t > 0$. This coherent effect results from induced phase modulation [13]. The pump pulse changes the phase of the probe pulse, and can thus affect its frequency spectrum. As a result, this pulse comes into better or worse resonance with the OH-stretch vibration, which causes an additional change in transmission.

The data show that there are two time scales present in the relaxation. The first relaxation step is from the $\nu_{\text{OH}} = 1$ state to an intermediate state with a time constant T_1 , the lifetime of the OH-stretch vibration. This first time scale is seen as the decay of the bleaching in Figure 4.2 (right panel), and as the decay of the induced absorption (left panel, upper two scans). The relaxation of this intermediate level leads to a complete equilibration and is characterized by a time constant τ_{eq} . The equilibrated state represents a situation in which the excitation energy is thermally distributed over all degrees of freedom in the focus. This dumping of energy leads to a temperature increase in the sample, which will affect the linear absorption spectrum of the OH-stretch band. An increase in temperature leads to a decrease of the absorption cross section and a shift of the absorption maximum to the blue, as is illustrated in Figure 4.3. A blue shift of the OH-stretch band indicates that the hydrogen bonds have become weaker and longer [67, 28]. In this case, the excess energy is delivered on a

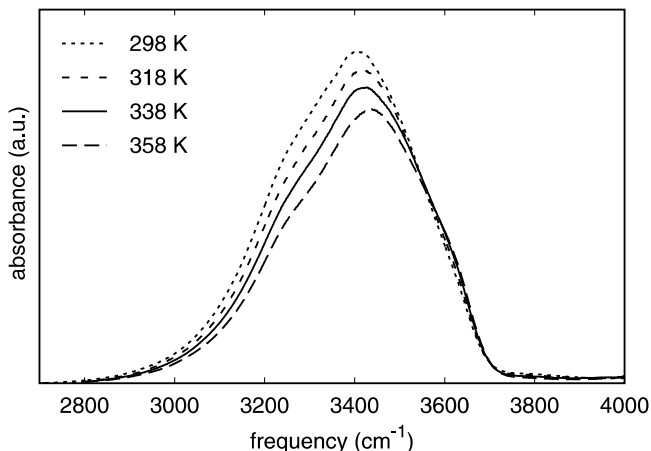


Figure 4.3. The OH-stretch absorption band at different temperatures. With increasing temperature, the absorption cross section decreases and the maximum of the absorption band shifts to the blue.

femtosecond time scale, so that there is no time for volume expansion. This means that the average oxygen-oxygen distance between the water molecules cannot increase. Hence, the blue shift cannot result from a lengthening of the average hydrogen bond length, but is likely caused by a change of the angle between the OH-bond and the hydrogen bond. An increased bending of the O–H···O system results in a weakening of the hydrogen bond interaction. The blue shift of the OH-stretch band means that a probe pulse in the red or center part of the band will see fewer molecules absorbing at that specific wavelength, which explains the higher final level of transmission. For probe pulses in the blue, the situation is reversed. Here, the pulse will see extra molecules at longer delay times, which gives rise to a lower final level of transmission, as can be seen in Figure 4.2 (right panel, lower two scans).

The temperature dependence of the thermalization process can best be determined in the red wing of the absorption band, i.e. near 3300 cm^{-1} , because at this frequency the thermalization effect completely dominates the observed dynamics. Transients of this frequency are shown in Figure 4.4, for three different temperatures. For comparison, the measured scans are scaled in such a way that at all temperatures, the final transmission change is the same. It is clear from Figure 4.4 that the equilibration time has no significant temperature dependence. For the lifetime of the OH-stretch vibration, however, we do find a temperature dependence, as is shown in Figure 4.5. Here, scans are shown at two temperatures: 298 and 358 K measured at a probe wavelength of 3000 cm^{-1} , which is resonant with the $\nu_{\text{OH}} = 1 \rightarrow 2$ absorption.

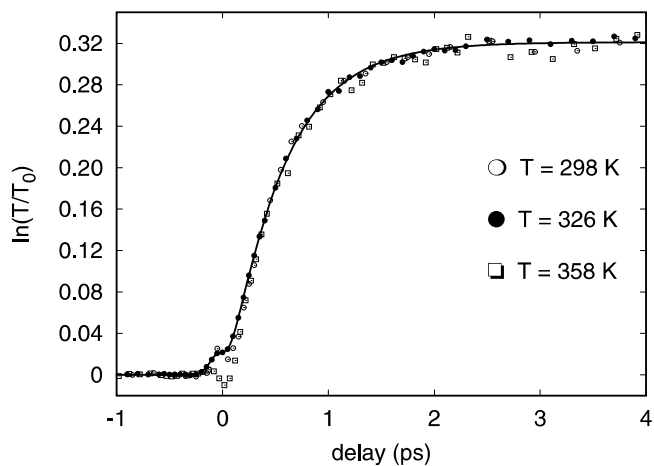


Figure 4.4. Delay time scans at different temperatures measured with pump and probe frequencies of 3400 and 3300 cm^{-1} , respectively.

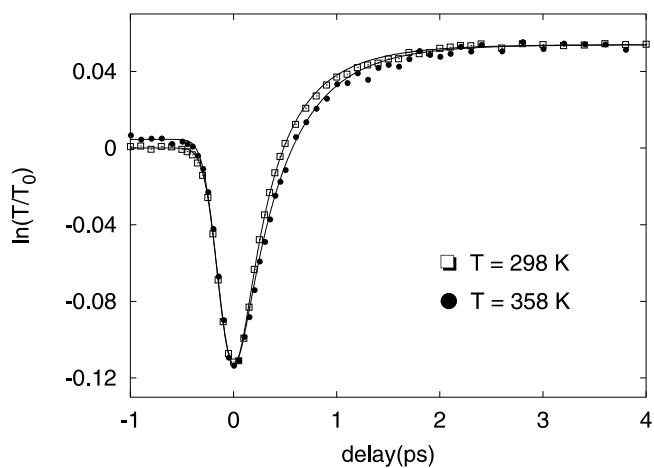


Figure 4.5. Transmission change $\ln(T/T_0)$ as a function of delay between pump and probe pulse at two different temperatures. The pump frequency was 3400 cm^{-1} , the probe frequency 3000 cm^{-1} .

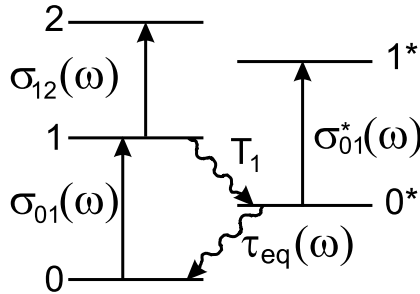


Figure 4.6. Energy level scheme used for fitting the data.

4.4 Kinetic modeling

To fit the data we use a model depicted in Figure 4.6 and fully described in Ref. [64]. It consists of the vibrational ground state (0), the first excited state (1), populated by the pump pulse, the second excited state (2) and the intermediate level 0* to which the population of state 1 relaxes with a time constant T_1 . In this model, the decay of the intermediate 0*-state leads to a full thermalization of the system. The associated time scale τ_{eq} represents the equilibration or thermalization time. The absorption cross sections for the $0 \rightarrow 1$ and $0^* \rightarrow 1^*$ transitions are $\sigma_{01}(\omega)$ and $\sigma_{01}^*(\omega)$, respectively.

The absorption of a probe beam by the sample can be denoted as follows

$$\alpha(\omega) \propto \sigma_{01}(\omega)(n_0 - n_1) + \sigma_{01}^*(\omega)(n_0^* - n_1^*) \quad (4.1)$$

where n_i denotes the population of state i . We can set $n_1^*(t) = 0$ because there is no thermal population of 0* and excitation by the probe beam will be negligible. When we substitute $n_0 = N - n_1 - n_0^*$, with N the total number of molecules and subtract the absorption of the probe without excitation by the pump pulse ($\alpha \propto \sigma N$), we get for the absorption change

$$-\Delta\alpha_{01}(\omega, t) \propto \sigma_{01}(\omega)[2n_1(t) + (1 - \frac{\sigma_{01}^*(\omega)}{\sigma_{01}(\omega)})n_0^*(t)] + N\delta\sigma_{01}(\omega, t) \quad (4.2)$$

The $\delta\sigma_{01}(\omega)$ in the last term of Equation (2) represents the change in cross section due to the temperature increase that results after the thermalization. Depending on the probe frequency this change will be positive (at the blue side of the absorption band) or negative (at the red side of the absorption band). Because the cross section change is proportional to the number of molecules relaxed from 0*, the last term can be written as:

$$N\delta\sigma_{01}(\omega, t) \propto \int_{-\infty}^t \frac{n_0^*(t')}{\tau_{eq}} dt' \quad (4.3)$$

If the probe pulse only probes the 1→2 transition, the absorption change reads as follows:

$$\Delta\alpha_{12}(\omega, t) \propto \sigma_{12}(\omega)n_1(t) + N\delta\sigma_{01}(\omega, t) \quad (4.4)$$

We have neglected $n_2(t)$ in the above equation, which is a good approximation since the excitation fraction of $\nu_{\text{OH}} = 1$ is only about 1 %. The last term again represents the effect of the change of the absorption band due to thermalization. The population numbers for the different states satisfy the following rate equations:

$$\frac{dn_1}{dt} = -\frac{n_1}{T_1} \quad (4.5)$$

$$\frac{dn_0^*}{dt} = \frac{n_1}{\tau_1} - \frac{n_0^*}{\tau_{\text{eq}}}, \quad (4.6)$$

$$\frac{dn_0}{dt} = \frac{n_0^*}{\tau_{\text{eq}}} \quad (4.7)$$

$$N = n_0 + n_1 + n_0^* \quad (4.8)$$

The rate equations can be solved leading to

$$n_1(t) = n_1(0)e^{-t/T_1} \quad (4.9)$$

$$n_0^*(t) = \frac{1}{\frac{T_1}{\tau_{\text{eq}}} - 1}(e^{-t/T_1} - e^{-t/\tau_{\text{eq}}})n_1(0) \quad (4.10)$$

$$n_0(t) = N - n_1(t) - n_0^*(t) \quad (4.11)$$

These functions are convolved with the measured cross correlation function of the pump and probe beam to account for the nonzero pulse widths. This gives us the full expressions for $-\Delta\alpha_{01}(\omega, t)$ and $\Delta\alpha_{12}(\omega, t)$ which can be compared to the measured $\ln(T/T_0)$. Fitting these functions to the actual data gives us the time constants T_1 and τ_{eq} , as well as the ratio $\sigma_{01}^*/\sigma_{01}$ at the probe frequency.

At some specific pump/probe combinations, an extra wiggle around $t = 0$ is observed, the induced phase modulation artifact [13] (see Section 4.3). We account for this effect by adding the derivative of the cross correlation function to the fit function, as an approximation.

A difficulty in fitting T_1 is the overwhelming contribution of the thermalization effect to the measured transmission change. This makes it impossible to get a reasonable T_1 value from the fits for probe frequencies larger than 3200 cm^{-1} . The best way to get an accurate value for T_1 is by fitting the scans which probe the 1→2 transition (Figure 4.2, upper scans of left panel). We take the value for the equilibration time τ_{eq} from the measurements at 3300 cm^{-1} where the temperature effect is so large that a precise determination of this value is possible. Using this value as a constant in the fit for the 1→2 transition, we obtain the value for T_1 .

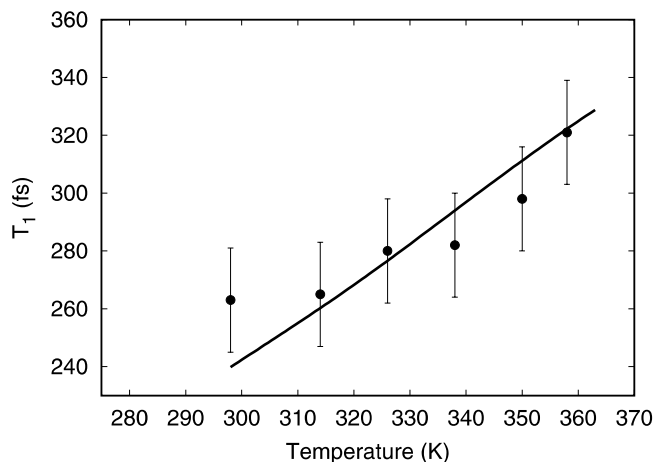


Figure 4.7. The lifetime of the OH-stretch vibration of H₂O as a function of temperature. The drawn curve represents the calculated behavior according to the Fermi's Golden rule expression of Equation 4.12 (see text).

As will be shown in the next chapter, for liquid water $\tau_{\text{eq}} = 0.55 \pm 0.05$ ps, independent of probe wavelength and of the amount of energy to be equilibrated [52]. All data of Fig. 4.2 can be well fitted with a τ_{eq} of 0.55 ± 0.05 ps and a lifetime T_1 of 260 ± 18 fs. The results displayed in Figure 4.4 can all be well described with a τ_{eq} of 0.55 ± 0.05 ps for all temperatures. The measured lifetimes T_1 are depicted in Figure 4.7 as a function of temperature. The increase of 20% is comparable with the increase measured in HDO:D₂O dilutions [108]. The relaxation in liquid water is three times faster than that of HDO:D₂O, where a lifetime of 740 fs was measured at room temperature [108].

4.5 Relaxation mechanism for the OH-stretch vibration

Deák et al. found that the relaxation of the OH-stretch vibration of H₂O results in a significant response of the H–O–H bending mode (δ) [12]. If the bending mode would be the main accepting mode, normally a decrease of the lifetime T_1 is expected as a function of temperature, because this mode has nearly harmonic character [36, 65]. This expectation is based on a theory that assumes that the excited mode is resonant with a large number of excitations in low-frequency accepting modes. However, the bending mode has a high frequency of about 1650 cm^{-1} , so that this mode can accept only one or two quanta. Hence, if the bending mode is one of the accepting modes, the relaxation rate will also strongly depend on the energy mismatch between donor

and acceptor modes.

The energy mismatch can be accounted for by calculating the following overlap integral, which results from Fermi's Golden Rule, and which gives an expression for the relaxation rate ($\propto 1/T_1$):

$$1/T_1 \propto 2\pi/\hbar \int \frac{e^{\frac{E_\nu}{kT}} - 1}{\prod [e^{\frac{E_\delta}{kT}} - 1]} |\langle 1_\nu 0_\delta | R_\nu R_\delta^2 | 0_\nu 2_\delta \rangle|^2 \delta(E_\nu - E_{2\delta}) \rho(E_\nu = E_{2\delta}) dE \quad (4.12)$$

where R_ν is the OH-stretch coordinate, R_δ the bending coordinate, $|0_\nu\rangle$ and $\langle 1_\nu|$ the wave functions of the ground and excited state of the OH-stretch vibration, and $|2_\delta\rangle$ and $\langle 0_\delta|$ the wave functions of the ground and second excited state of the bending mode. $\rho(E_\nu = E_{2\delta})$ is the density of states. The term preceding the anharmonic coupling matrix element represents the effect of the thermal population of the accepting mode on the relaxation [66]. This term assumes the transfer of one OH-stretch quantum to two quanta of the bending mode. Raising the temperature from 298 to 358 K, this term increases by 0.1%, which means that this term has a negligible effect on the relaxation rate.

The anharmonic coupling matrix element $|\langle 1_\nu 0_\delta | R_\nu R_\delta^2 | 0_\nu 2_\delta \rangle|^2$ can be written as $|\langle 1_\nu | R_\nu | 0_\nu \rangle|^2 |\langle 0_\delta | R_\delta | 2_\delta \rangle|^2$. The spectral dependence of $|\langle 1_\nu | R_\nu | 0_\nu \rangle|^2$ can be approximated by the linear absorption spectrum of the OH-stretch, provided that the spectral diffusion within this band is very rapid. Similarly, the spectral dependence of $|\langle 0_\delta | R_\delta | 2_\delta \rangle|^2$ can be approximated by the absorption or Raman spectrum of the overtone of the bending mode. The presence of the function $\delta(E_\nu - E_{2\delta})$ implies that the integral in Eq. 4.12 will only be nonzero if the absorption bands of the OH-stretch and the overtone of the bending mode overlap. The temperature dependence of Eq. 4.12 can thus be approximated by calculating the overlap as a function of temperature [1].

For the calculation of the overlap of the spectra we have used the measured temperature dependent absorption spectra as displayed in Figure 4.3, where a decrease of the absorption cross section and a slight blue shift is observed. The reason for this change of the linear absorption spectra is that the hydrogen bonds get weaker [67]. With increasing temperature, the position of the bending mode slightly shifts to the red (from 1644.5 at $T = 298$ K to 1642.3 cm^{-1} at $T = 348$ K) [16] and the band gets somewhat narrower (83 cm^{-1} FWHM at $T = 348$ K instead of 88 cm^{-1} FWHM at $T = 298$ K) [16]. The intensity of this band does not depend on temperature [55, 5, 4]. The spectrum of the bending mode can be well fitted with a Lorentzian line shape. We calculate the convolution of this spectrum with itself to estimate the absorption profile for the overtone.

The result of the calculation of the overlap of the spectrum of the OH-stretch and the overtone of the bending mode is displayed in Figure 4.7. The only free parameter in the comparison between experiment and theory is the absolute value of T_1 . Clearly, the calculation gives a good description of the observed temperature dependence of

T_1 . The increase in T_1 with temperature can thus be explained from the blue shift of the OH-stretch band, the red shift of the overtone of the H-O-H bend mode, and the decrease in cross section of the OH-stretch mode. These changes in the spectra all follow from the weakening of the hydrogen bonds with temperature. This means that, although practically all of the energy of the excited OH-stretch of the H₂O molecule is transferred to the bending mode, the hydrogen-bond interaction still plays an important role in determining the rate of energy transfer, since it influences the energy mismatch and the magnitude of the anharmonic coupling.

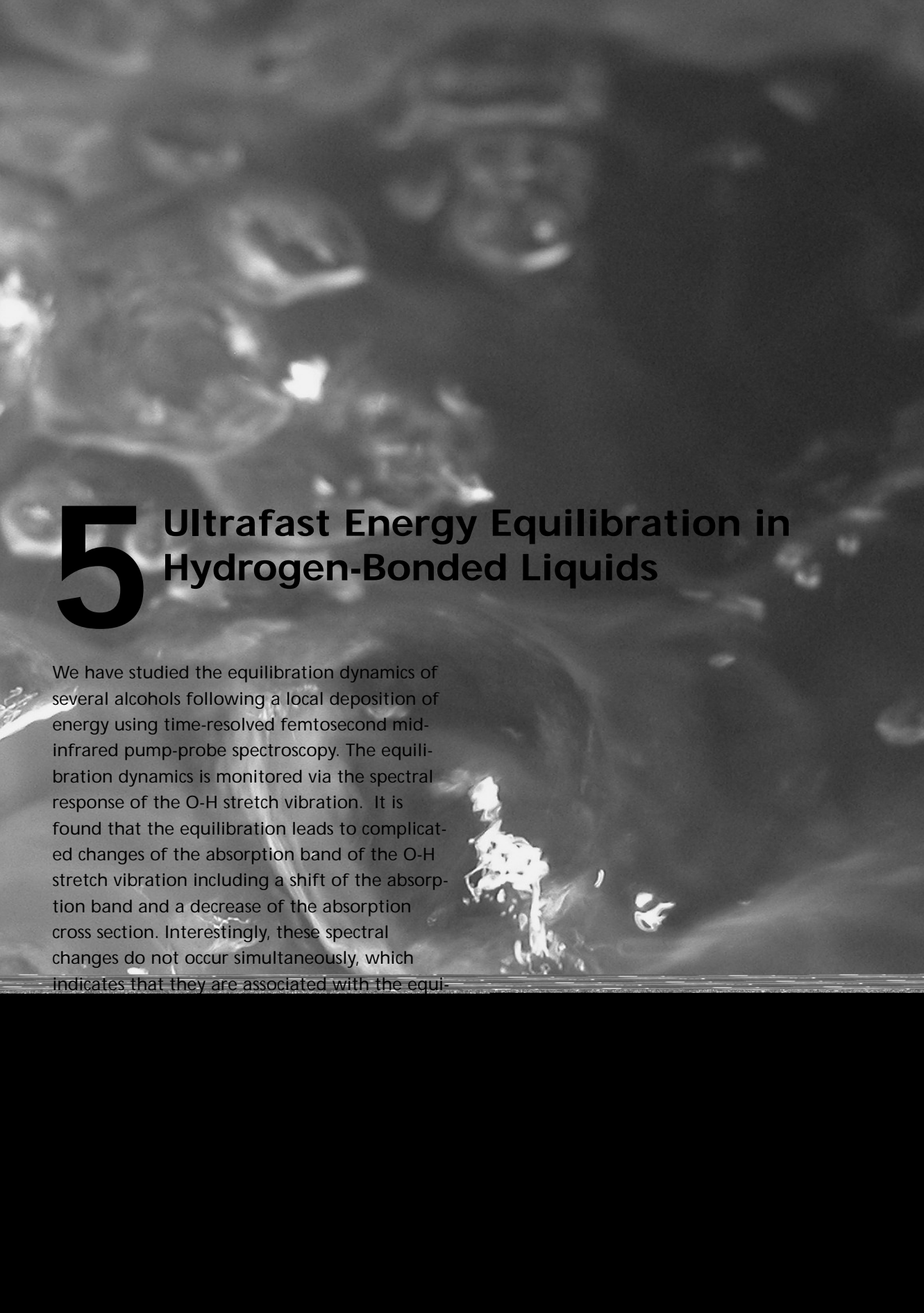
In the next chapter [52], we will show that the energy relaxation of the intermediate state likely forms the rate limiting step of the equilibration. The combination of that result with the present findings on the nature of the intermediate state, suggests that the vibrational lifetime of the bending mode is 550 fs. This value agrees quite well with the interval of $0.6 < T_\delta < 1.2$ ps (with T_δ the lifetime of the bending vibration) found by Deàk et al. [12].

Based on the present findings for the relaxation mechanism of pure H₂O, one could ask the question whether the bending mode forms also the accepting mode in HDO:D₂O. Pure liquid water has the special feature that the overtone of the bending mode (2δ) is in resonance with the OH-stretch vibration (ν). For HDO:D₂O, however, the resonance frequency of the bending mode is 1450 cm^{-1} , which gives rise to a frequency mismatch of more than 500 cm^{-1} between the OH-stretch and the overtone of the bending mode. Therefore extra excitation in other modes is needed to overcome this energy mismatch, a reasonable candidate is the hydrogen bond stretch mode (200 cm^{-1}). Hence, we must conclude that for HDO:D₂O the relaxation mechanism is still not completely clear. It is not possible yet to decide whether the accepting mode is a combination of the bending mode and the hydrogen bond stretch mode, or both this combination tone and a relaxation channel in which all the energy is transferred to the hydrogen bond mode.

4.6 Conclusions

We performed mid-infrared pump-probe spectroscopy to study the temperature dependence of the lifetime of the OH-stretch vibration in pure liquid water (H₂O). We observed two time scales in the relaxation process, the lifetime of the OH-stretch vibration T_1 and the equilibration time τ_{eq} . For the equilibration time constant no temperature dependence of the equilibration time was observed. For the lifetime of the OH-stretch vibration, an increase is observed from 260 ± 18 (at 298 K) to 320 ± 18 fs (at 358 K). This means that the relaxation in pure H₂O is three times faster than in HDO:D₂O; the increase with temperature, however, is comparable, 20% in both cases. We were able to give an accurate description of the observed lifetime increase for pure H₂O by calculating the overlap integral between the overtone of the bending mode and the stretch mode as a function of temperature. The spectral positions and shapes

of both absorption bands alter as a function of temperature due to changes in the hydrogen bond interactions. This means that for H₂O the OH-stretch vibrations relax by energy transfer to the overtone of the bending mode, but the rate at which this transfer takes place strongly depends on the hydrogen-bond interaction, since this interaction determines the energy mismatch and the magnitude of the anharmonic coupling.



5 Ultrafast Energy Equilibration in Hydrogen-Bonded Liquids

We have studied the equilibration dynamics of several alcohols following a local deposition of energy using time-resolved femtosecond mid-infrared pump-probe spectroscopy. The equilibration dynamics is monitored via the spectral response of the O-H stretch vibration. It is found that the equilibration leads to complicated changes of the absorption band of the O-H stretch vibration including a shift of the absorption band and a decrease of the absorption cross section. Interestingly, these spectral changes do not occur simultaneously, which indicates that they are associated with the equi-

5.1 Introduction: water as solvent for (bio)chemical reactions

By a rearrangement of the water molecules in the surroundings of the reactive intermediates of chemical reactions, water is able to stabilize these intermediates and to lower the energy barrier for the reaction. The dynamics of chemical reactions in aqueous solution will be governed both by the dynamics of the solvation interactions and the rate at which water molecules can accept the energy dissipated in the reaction. The solvation dynamics of water has been investigated by probing the response of solvating water molecules to an electronic rearrangement in a dissolved dye molecule [39, 70]. The solvation dynamics were observed to consist of a fast inertial component with a time response of ≈ 50 femtoseconds and two slower, diffusive components with subpicosecond response times.

Several theoretical studies have been performed on the role of liquid water as a solvent for different solutes, ranging from peptides and biomolecules [9, 74] to organic molecules [102] and HDO [76]. In Ref. [9] a combined quantum mechanical and classical mechanical (QM/MM) method is used. The active part of the system, for example an excited state, is treated quantum-mechanically, while the environment can be treated with molecular dynamics simulations. With this technique normal modes, potential energy surfaces and solvent-induced spectral shifts can be obtained. The importance of water as a solvent is also illustrated in Ref. [102] where the relaxation of vibrationally excited CH_3Cl molecules in water is studied. It was shown that a large number of water molecules participate in the redistribution of the vibrational energy. In Ref. [76] molecular dynamics simulations were used to investigate the rate and mechanism of the vibrational relaxation of HDO molecules dissolved in D_2O . In this study the OH-stretch was found to relax to the first overtone of the bending mode with a time constant of 7.5 ps. The excess energy of the bending mode will be accepted by the so-called bath modes, which are the low frequency modes, like rotations and translations of all molecules, but no time scale was given for this process of equilibration.

The outcome of molecular dynamics simulations on liquid water strongly depends on the modeling of the interactions between the water molecules [60]. Hence, there is a strong need for experimental information. In particular one would like to know the time scale on which low-frequency water modes, like librations and hydrogen-bond translations, respond to a local deposition of energy induced by a (bio)chemical reaction. In this respect, linear spectroscopic studies are not very informative due to the large inhomogeneity of aqueous systems. Therefore, nonlinear spectroscopic techniques using intense ultrashort pulses should be employed. Unfortunately, it is difficult to probe the response of low-frequency water modes directly on an ultrashort time scale. A solution to this problem is to follow a higher-frequency mode that is strongly coupled to these modes. For the case of the hydrogen bond, the OH-stretch vibration (ν_{OH}) forms a suitable probe, because the frequency of the OH-stretch vibration depends linearly on the hydrogen-bond length [28, 67]. Hence, this

vibration can be used as a probe for low-frequency hydrogen-bond dynamics that in turn represent changes in orientation and position of the water molecules.

Until now not much is known about the time scale on which water molecules react to an ultrafast dissipation of energy. Vodopyanov performed saturation studies in which water and ethanol layers were excited with intense picosecond laser radiation [95, 96, 97, 98]. In these studies a blue shift of the OH-stretch absorption band was observed due to a rise in temperature after irradiation. From the intensity dependence of the saturation, the vibrational lifetime T_1 of the OH-stretch vibration of HDO dissolved in D_2O was estimated to be between 0.3 and 0.6 ps and the lifetime of the OH-stretch vibrations of pure H_2O was estimated to be <3 ps [98]. A major problem in these studies was that it was not possible to separate the time scale of the relaxation of the OH-stretch excitation from that of the full equilibration of the energy in the liquid. If the OH-stretch vibration relaxes to some non-thermal intermediate state, these time scales will be different. Recently, the vibrational lifetime T_1 of the OH-stretch vibration of HDO dissolved in D_2O was measured using femtosecond mid-infrared pulses and was found to have a value of 740 ± 20 femtoseconds at room temperature [108]. Since the system studied was a dilute solution of HDO, the temperature increase of the sample due to the relaxation was negligibly small and no information on the equilibration dynamics of the water was obtained.

Here we present a study on the equilibration dynamics of water and alcohols at room temperature following a local dissipation of energy. The equilibration dynamics are monitored by probing the spectral changes of the OH-stretch absorption band with femtosecond mid-infrared laser pulses. It is found that the equilibration dynamics in water is exceptionally fast in comparison to the alcohols.

5.2 Experimental

The setup used for the results presented in this chapter, is depicted in Figure 5.1. We use a Ti:Sapphire based laser system that delivers 800 nm, 1 mJ pulses at a repetition rate of 1 kHz and a duration of about 110 fs. All of the 800 nm light is sent into one optical parametrical amplification and generation (OPA/OPG) stage based on β -BaB₂O₄. Part of the pump light is converted into signal and idler pulses with a central wavelength for the signal of 1.1 μ m. A beam splitter divides the signal pulses into two parts. The strongest part of the signal is used, together with the remaining 800 nm pump light, in a second parametric amplification process in a KTiOPO₄-crystal to generate pulses near 3 μ m [15]. The pulses have typical energies of 15 μ J, a FWHM duration of 220 fs and a spectral width of 80 cm^{-1} . The infrared pulses generated as described above (pump pulses) are focused into the sample and are used to excite a fraction of the molecules from the vibrational ground state to the $\nu_{OH} = 1$ state. Thereby energy is put into a specific degree of freedom.

By the same generation mechanism the second weaker part of the signal is con-

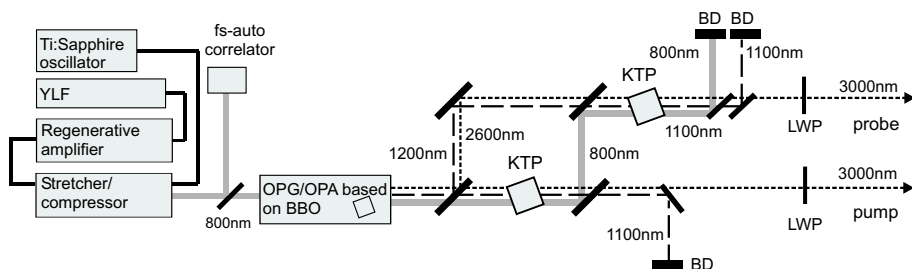


Figure 5.1. Generation of mid-infrared laser pulses. See text for the description of the generation. BD: beam dump; LWP: long wave pass filter; BBO and KTP: crystals

verted to pulses around $3 \mu\text{m}$. These pulses have the same duration and spectral width as the pump pulses and an energy per pulse of approximately $1 \mu\text{J}$. They are also focused on the sample and are used to monitor the thermalization of the excitation of the pump pulse. The transmission of the probe and pump pulses through a $200 \mu\text{m}$ pinhole was typically 50%. The probe polarization was set at the magic angle with respect to the polarization of the pump pulse by means of a zero-order $\lambda/2$ plate.

We investigated the equilibration dynamics of pure water, methanol, ethanol and 1-propanol. The samples consisted of a thin layer of liquid ($\approx 1 \mu\text{m}$ for water, $15 \mu\text{m}$ for the alcohols) between two sapphire windows. In order to avoid heating in the sample due to former excitation pulses, the sample was rotated. The temperature rise due to a single pump pulse is calculated to be approximately 30 K for water.

5.3 Results

The conventional infrared absorption spectrum of the OH-stretch band of water is depicted in the previous chapter, Figure 4.3. The absorption band has its maximum at 3410 cm^{-1} and has a width of 420 cm^{-1} at room temperature. It consists of two sub-bands stemming from the symmetric and antisymmetric stretching normal modes. In Figure 4.2, the transmission change $\ln(T/T_0)$ as a function of delay time is shown for pure water. The molecules are excited with a pump pulse with a central frequency of $\nu = 3250 \text{ cm}^{-1}$ and are probed at eight different frequencies. Let's resume the observations from that figure. All displayed curves show a higher or lower final level of transmission for long delay times. This level remains constant on a very long time scale, which indicates that this level of transmission results from the complete thermalization of the system. Probing at the red side of the absorption band (upper two curves, left panel) shows an induced $1 \rightarrow 2$ absorption around $t = 0$. At the blue side (upper two curves right panel) a bleaching peak is observed around $t = 0$. For probe frequencies in the center of the absorption band (3200 and 3400 cm^{-1}), the

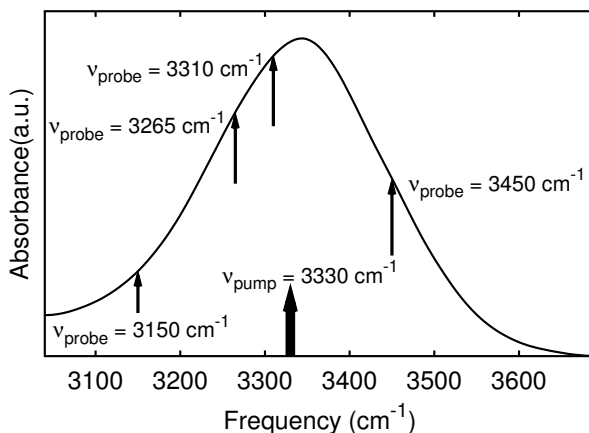


Figure 5.2. Absorption spectrum of the OH-stretch vibration of pure ethanol. The maximum of the band is at 3330 cm^{-1} . The pump and probe frequencies are indicated with arrows.

bleaching peak is overwhelmed by the thermalization effect.

Here, we compare the measured signals for water with results obtained for methanol, ethanol and 1-propanol for which the hydrogen-bond strength is similar to that of water. In Figure 5.2, the OH-stretch absorption spectrum of pure ethanol ($\text{C}_2\text{H}_5\text{OH}$) is presented. The absorption spectra of methanol (CH_3OH) and 1-propanol ($\text{C}_3\text{H}_7\text{OH}$) are very similar to that of ethanol. Again we pump at the center frequency of the band, which is at 3330 cm^{-1} for these three alcohols. The frequencies of the probe pulses (3150 , 3265 , 3310 and 3450 cm^{-1}) are indicated by arrows in Figure 5.2.

Figure 5.3 shows delay time scans for pure ethanol. The observed relaxation behavior is very similar to that of water. For Figure 5.3b and 5.3c, we again observe after a bleaching at $t = 0$ and a decay at short delay times, a rise towards a permanent bleaching signal. Clearly, the same process of equilibration is observed as in water, but the time scale is dramatically different. In Figure 5.3d, the probe wavelength is in the red wing of the absorption band. We observe an induced $\nu_{\text{OH}} = 1 \rightarrow 2$ absorption, followed by a rise to an increased level of transmission, as was observed for water in Figure 4.2 (upper curves, left panel). In Figure 5.3a, where the probe wavelength is in the blue wing of the OH-stretch absorption band, the observed signal decreases to a negative final value.

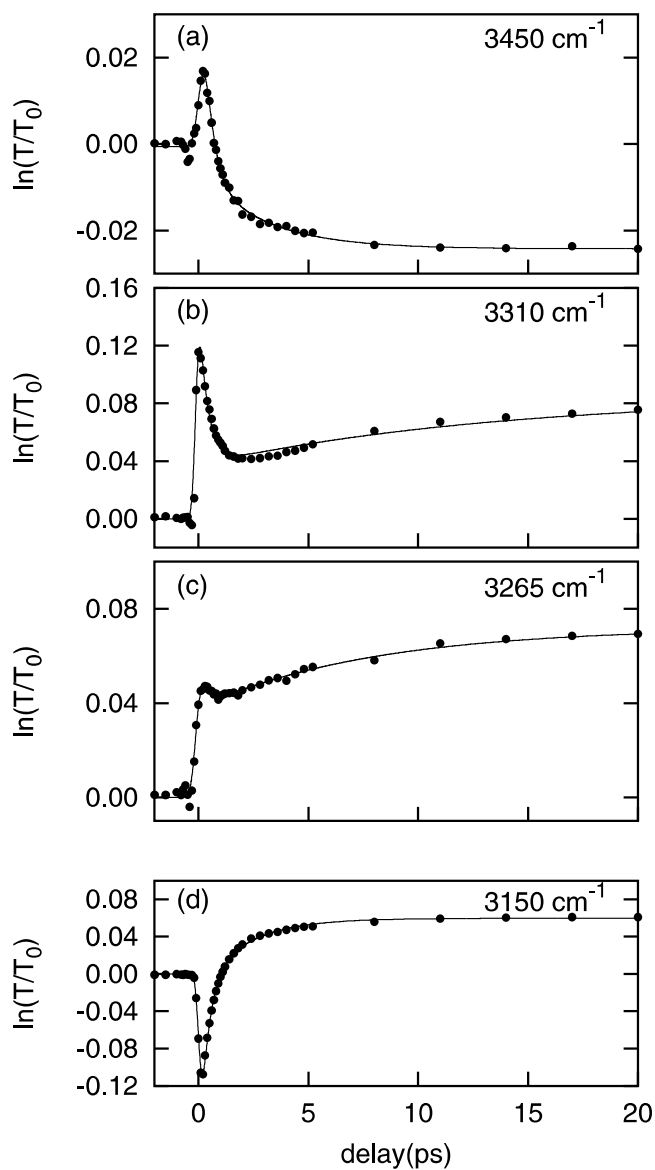


Figure 5.3. Delay time scans for pure ethanol after excitation with a 3330 cm^{-1} pump pulse. Transmission changes were recorded with probe pulses at the blue (a) 3450 cm^{-1} , center (b) 3310 cm^{-1} and (c) 3265 cm^{-1} and at the red (d) 3150 cm^{-1} of the absorption band.

5.4 Kinetic modeling

The results are interpreted in the same way as in the previous chapter. The pump pulse excites molecules from the $\nu_{\text{OH}} = 0$ to the $\nu_{\text{OH}} = 1$ state. This excited population relaxes with a time constant T_1 to an intermediate level, which is the vibrational (OH-stretch) ground state combined with (an)other vibrational mode(s). The exact nature of the intermediate level is not crucial here. It is only essential that the intermediate level does not yet represent thermal equilibrium, implying that only very specific combination tones get directly excited by the relaxation of the OH-stretch vibration.

The relaxation of the intermediate level leads to a full thermalization, i.e. a redistribution of the energy over all degrees of freedom. This thermalization occurs with a time constant τ_{eq} . After equilibration, the temperature of the sample is increased, which leads to weaker hydrogen bonds and therefore to a blue shift of the OH-stretch resonance frequency [28, 67]. As a result, the transmission at the center frequency and at the red side is strongly increased at longer delay times, while at the blue side of the OH-absorption band an induced absorption is observed (Figure 5.3a). By changing the pump intensity we found that the thermalization (equilibration) time does not depend on the amount of energy to be equilibrated.

Table 5.1. Fit results for different hydrogen-bonding liquids

	T_1 (fs)	τ_{eq} (ps) 1 \rightarrow 2	τ_{eq} (ps) red	τ_{eq} (ps) center	τ_{eq} (ps) blue
H ₂ O	260 \pm 20	0.55 \pm 0.05	0.55 \pm 0.05	0.55 \pm 0.05	0.55 \pm 0.05
CH ₃ OH	250 \pm 100	1.5 \pm 0.5	-	7.0 \pm 0.5	-
C ₂ H ₅ OH	450 \pm 100	2.1 \pm 0.5	7 \pm 1	13 \pm 2	3.2 \pm 0.5
C ₃ H ₇ OH	500 \pm 100	3.0 \pm 0.5	-	15 \pm 2	-

We have fitted the data on the alcohols with the model presented in the previous chapter (see Section 4.4). We followed the same procedure to extract the parameters T_1 and τ_{eq} . Because the measurement showing induced absorption, Figure 5.3d, is most sensitive to T_1 , we fitted Eq. 4.4 to this measurement to extract both T_1 and τ_{eq} . Due to the large contributions of the thermalization signals, the fitted T_1 was taken constant in fitting Figure 5.3a-c with Eq. 4.2. The results of the fits are shown in Table 5.1. The results for water are obtained in Chapter 4. In this table, 1 \rightarrow 2, red, center and blue mean probing at 3150, 3265, 3310, and 3450 cm⁻¹, for ethanol. For methanol and 1-propanol 1 \rightarrow 2 and center stand for 3150 and 3310 cm⁻¹, respectively.

5.5 Discussion

In our experiment the response of the OH-stretch vibration is used to monitor the equilibration process. This OH-stretch vibration is very sensitive to changes in the relative positions of the water and alcohol molecules. The observed blue shift of the OH-stretch absorption band and the decrease of the cross-section thus directly reflect the repositioning of the molecules that follows from the dissipation of energy.

5.5.1 Energy redistribution and repositioning

It should be noted that the equilibration involves two subsequent processes. The first process is formed by the energy redistribution in which the energy of the non-thermal intermediate level becomes thermally distributed over all degrees of freedom. After this redistribution the equilibration is not yet complete because putting energy in a particular degree of freedom does not imply that the coordinate corresponding to this degree of freedom instantaneously finds its new equilibrium position. For instance, if a molecule is excited with a short pulse to a dissociative potential, it still takes some time, determined by the time scale of the nuclear motion, before the molecule is really dissociated. In a similar fashion it takes some time after the energy has been redistributed before the low-frequency translational and rotational degrees of freedom have acquired their new equilibrium positions. Hence, after the first process of energy redistribution, the equilibration involves a second process in which the molecules reposition at their new equilibrium positions. This repositioning of the molecules is directly observed in our experiment, since this process affects the cross section and spectral position of the OH-stretch absorption band.

The question arises whether the energy redistribution or the repositioning forms the rate-limiting step of the overall equilibration. It is to be expected that the three-dimensional hydrogen-bonded network of water allows for a much faster redistribution of energy than the one-dimensional hydrogen bonded chains [40, 45, 82] of methanol, ethanol and propanol. Hence, if the energy redistribution would form the rate-limiting step of the equilibration, water is expected to show a faster equilibration than the three alcohols, as indeed is observed. However, in that case the three alcohols are expected to have very similar equilibration times, which is certainly not the case. If on the other hand, the repositioning of the molecules forms the rate-limiting step of the equilibration, the equilibration rate is expected to scale inversely with the mass of the molecules. This agrees quite well with the observation that the equilibration time constant increases going from water to methanol, ethanol and propanol. If the overall equilibration time is indeed determined by the rate of the repositioning of the molecules, the time scales of the equilibration of water, methanol, ethanol and propanol should correlate with those observed in dielectric relaxation and rotational correlation experiments.

Dielectric relaxation measurements [3, 42] on the pure liquids show Debye relax-

ation times of about 8 ps for water, 50 ps for methanol, about 160 ps for pure ethanol and about 320 ps for 1-propanol. Debye relaxation times calculated from NMR spectroscopy yield about 10 ps for water [3, 6], 41 ps for methanol [19], 190 ps for ethanol [19] and 560 ps for 2-propanol [19]. Hence, dielectric relaxation measurements show a very similar increase in time constant going from water to methanol to ethanol to 1-propanol as we observe for the equilibration. This strongly suggests that at least for the alcohols the repositioning of the molecules forms the rate-limiting step in the equilibration. However, for the fastest liquid, being liquid water, the rate of equilibration could still be limited by the rate of energy redistribution.

It should be noted that, although the trend matches, the absolute values of the Debye relaxation time and the equilibration time do not match. Here it should be realized that reorientation, as it is measured in Debye relaxation and rotational correlation experiments, and thermalization are not defined in the same way. The repositioning of the molecules in a thermalization process mainly involves a small change (a few degrees) in the angle the hydrogen-bond makes between donor and acceptor groups to make an appreciable difference in absorption cross section. In NMR and dielectric relaxation measurements, reorientation times are defined on the basis of a rotation of the whole molecule; rotation angles are in this case more in the order of 90 degrees. Hence, it is not surprising that the time scales measured for the equilibration process are much shorter than the Debye relaxation and orientational relaxation time constants.

5.5.2 Low frequency hydrogen-bond modes

A striking difference between the equilibration of the alcohols and liquid water is the frequency dependence of the equilibration time. For the alcohols the equilibration time constant strongly depends on the probe frequency, in the wings of the OH-stretch absorption band the equilibration time constant is much shorter than in the center of the absorption band. In contrast, for water the equilibration time constant is the same at all frequencies. A closer look at the fits to the alcohol data also shows that the equilibration process is not truly singly exponential, in the early stages of the equilibration the equilibration is somewhat faster than the fitted exponential function and at longer times the equilibration is somewhat slower than the fitted function.

The frequency dependence of the fitted equilibration time constant and the non-exponential character of the equilibration of the alcohols indicates that at least two time scales are involved in the equilibration process of the alcohols, i.e. in the repositioning of the molecules. It should be realized that shifts of the absorption spectrum will much more affect the transmission measured in the wings of the absorption than in the center, whereas a decrease in the absorption cross-section will have a similar effect on all probe frequencies. The fact that the fitted equilibration time constant is much shorter in the wings (Figures 5.2a,d) than in the center (Figures 5.2b,c) thus indicates that the blue shift of the absorption band occurs on a shorter time scale

than the decrease of the absorption cross-section.

The total picture is now as follows. After the energy has been redistributed over all degrees of freedom, the coordinates of the low-frequency modes should find their new equilibrium positions. The most obvious candidate low-frequency mode that could influence the position of the OH-stretch band would be the hydrogen-bond stretching vibration. However, the blue shift of the OH-stretch band due to lengthening of the hydrogen-bond, can only be due to thermal expansion, which is a process that takes place on nano- or microsecond time-scales. Hence, the a stretching of the hydrogen bond is not responsible for the fast blue shift of the stretch band.

The only coordinates that can be responsible for both the decrease in cross section as well as the blue shift of the OH-stretch band are the hydrogen-bond bending and librational coordinates. Both affect the angle between the OH-group and the O-H...O hydrogen-bond. Apparently, the first small change of this angle, which affects the charge density on the hydrogen atom and hydrogen bond acceptor oxygen atom, leads to the blue shift. A further change in the hydrogen-bond bending coordinate decreases the amount in which the OH-groups on different alcohol molecules are in line. Thereby the conjugation of the OH-stretch vibrations is reduced which leads to a decrease of the absorption cross-section.

For water the equilibration time hardly depends on the probe frequency which strongly suggests that for water the rate of equilibration is not limited by the rate at which the water molecules attain their new positions in the liquid but rather by the rate of energy redistribution. Hence for water the observed equilibration time constant is mainly determined by the relaxation rate of the non-thermal intermediate state. This means that the observed time scale of ≈ 0.55 ps presents an upper limit for the time scale on which the molecules in liquid water reposition following a dissipation of energy.

5.6 Conclusions

Using two-color femtosecond mid-infrared pump-probe spectroscopy, we investigated the equilibration dynamics of water, methanol, ethanol and 1-propanol, following a local deposition of energy. In the experiments, the OH-stretch vibration is excited that relaxes to a non-thermal intermediate state, which is formed by specific combination tone(s) of excited intra- and intermolecular vibrations. The relaxation of this non-thermal intermediate state leads to a complete (thermal) equilibration of the energy. The dynamics of the latter equilibration process is monitored via the spectral response of the OH-stretch vibration. We observe that the equilibration leads to a blue shift of the OH-stretch absorption band and a decrease of the absorption cross section. Using a kinetic modeling of the experimental data we find that the time constants of equilibration of water, methanol, ethanol and 1-propanol are 0.55, 1.5-7, 2.1-13 and 3.0-15 ps, respectively. The equilibration time scale increases with increasing

molecular mass, which indicates that for the alcohols the rate of equilibration is determined by the rate at which the molecules can change their relative orientations and positions in the liquid.

For the alcohols the frequency dependence of the equilibration time constant suggests that the blue shift of the absorption band is much faster than the decrease in absorption cross-section. The hydrogen-bond bending coordinate is responsible for both processes.

For water, we observe a very short equilibration time constant of 0.55 ps, which, in contrast to the alcohols, hardly depends on frequency. This suggests that for water the equilibration rate is not determined by the repositioning of the molecules (as for the alcohols) but rather by the rate of energy relaxation from a non-thermal intermediate state. Hence, the reposition of the molecules in liquid water probably occurs on a time scale that is shorter than 0.55 ps. This means that water can adapt extremely fast, much faster than alcohols, to a deposition of energy.

6

Comment on: Vibrational relaxation and spectral evolution following ultrafast OH stretch excitation of water by A. Pakoulev, Z. Wang, D.D. Klott



In a recent Letter by Pakoulev et al. (Chem. Phys. Lett. 371 (2003) 594), time-resolved anti-Stokes Raman measurements of the spectral evolution and relaxation of the OH stretch vibrations of pure H₂O were presented. These measurements led the authors to reinterpret the results presented in Chapter 4. Here we show that this reinterpretation is incorrect.

6.1 Introduction

In a recently published Letter [69], time-resolved anti-Stokes Raman measurements of the spectral evolution and vibrational relaxation of pure H₂O were presented. It was observed that the spectrum of the OH-stretch excitation undergoes a rapid blue shift with a time constant of ~ 0.4 picoseconds (ps), and that the vibrational lifetime is ~ 0.7 ps. These results are quite surprising, since they appear to be contradictory to the results we obtained in Chapter 4 in which the vibrational dynamics of H₂O were probed with femtosecond mid-infrared pump-probe spectroscopy [51]. In the latter study, the vibrational lifetime of H₂O was found to be only 0.26 ± 0.02 ps, and it was observed that the vibrational relaxation was followed by a slower thermalization process with a time constant τ_{eq} of 0.55 ± 0.05 ps.

The authors of Ref. [69] reinterpret the 0.26 ps time constant of Chapter 4 as spectral diffusion, and the 0.55 ps time constant as the true vibrational lifetime of the O–H stretch vibration of water. However, in this reinterpretation they overlooked several essential elements of the mid-infrared pump-probe results that disprove this reinterpretation.

In our femtosecond mid-infrared pump-probe experiments on water, the O–H stretch vibrations ($3000\text{--}3600\text{ cm}^{-1}$) of water were excited with an intense infrared pump pulse (pump). This excitation results in a bleaching of the fundamental $v = 0 \rightarrow 1$ transition and in an induced absorption of the $v = 1 \rightarrow 2$ transition. The $v = 1 \rightarrow 2$ transition is red-shifted by $\sim 250\text{ cm}^{-1}$ with respect to the $v = 0 \rightarrow 1$ transition. The transmission changes were probed with a second, independently tunable femtosecond mid-infrared pulse (probe). The change in absorbance induced by the pump is given by $\ln[T(\tau)/T_0]$, with $T(\tau)$ the transmission of the sample in presence of the pump, and T_0 the transmission of the sample in absence of the pump.

In Fig. 6.1 femtosecond pump-probe data are shown obtained for a sample of pure H₂O using a pump pulse with a central frequency of 3550 cm^{-1} and four different probe frequencies. The pump pulse had a pulse duration of 220 fs and an energy of $\sim 10\text{ }\mu\text{J}$. The probe had a pulse duration of 220 fs and an energy $< 1\text{ }\mu\text{J}$. The results shown in Fig. 6.1 show the presence of two relaxation processes: a first fast process with a time constant of 0.30 ± 0.05 ps, and a second, slower process with a time constant of 0.55 ± 0.05 ps. These results are very similar to the results reported in Chapter 4.

6.2 Spectral diffusion or vibrational relaxation

Pakoulev et al. [69] suggested that the fast decays of the absorption at frequencies $< 3100\text{ cm}^{-1}$ and of the bleaching at frequencies $> 3500\text{ cm}^{-1}$ we observed, could result from spectral diffusion within the $v = 1 \rightarrow 2$ band.

For our results, spectral diffusion will lead to a shift to higher frequencies, because in this study the pump pulse had a central frequency of 3250 cm^{-1} (see Fig. 4.2), which is at the red side of the O–H stretch absorption band. A frequency of 3100

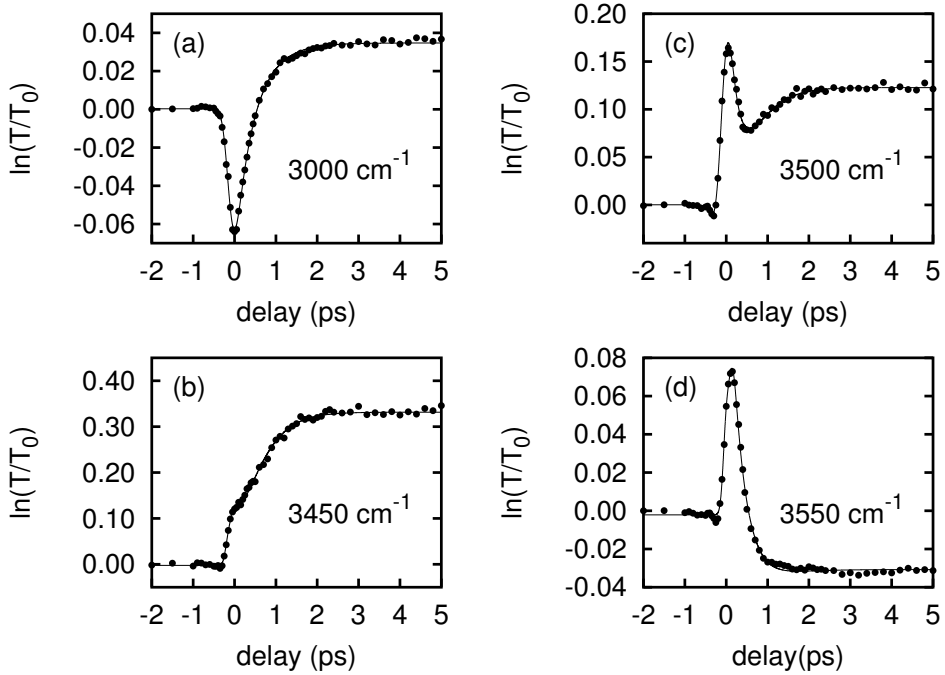


Figure 6.1. Femtosecond mid-infrared pump-probe scans of liquid water at 298 K. The central frequency of the pump is 3550 cm^{-1}

cm^{-1} corresponds to the high-frequency side of the $v = 1 \rightarrow 2$ transition. Hence, a shift of the $v = 1 \rightarrow 2$ response to higher frequencies is expected to lead to a *rise* of absorption with a time constant of ~ 0.3 ps, and not, as is observed, to a *decay* with ~ 0.3 ps. In addition, at 3500 cm^{-1} the response of the $1 \rightarrow 2$ transition will be much weaker than the response of the fundamental $v = 0 \rightarrow 1$ transition. Hence, spectral diffusion to higher frequencies with a time constant of ~ 0.3 ps should result in a *rise* of a bleaching signal at 3500 cm^{-1} , and not, as is observed, in a *decay* with this time constant. Finally, pumping at 3550 cm^{-1} (Fig. 6.1) is observed to lead to the same results as pumping at 3250 cm^{-1} [51], which indicates that for H_2O spectral diffusion within the O–H stretch absorption band is extremely fast with a time constant < 100 fs. This notion agrees with the results of a previous study of the depolarization of vibrational excitations in water [104]. In view of the above, the relaxation process with a time constant of ~ 0.3 ps cannot be explained from spectral

diffusion. Instead, the decay of the absorption observed at 3100 cm^{-1} and of the bleaching at frequencies $>3500\text{ cm}^{-1}$ with time constant $0.30\pm 0.05\text{ ps}$ must represent the population relaxation of the $v = 1$ state.

In the discussion of Ref. [69] it is stated that we would claim the region between 3200 and 3400 cm^{-1} to be insensitive to the T_1 process. This is an incorrect citation: in Chapters 4 and 5 it was stated that in this frequency region the effect of the thermalization is so large that the measured signals are *dominated* by the thermalization process. In fact, the region between 3200 and 3400 cm^{-1} is about as sensitive to the T_1 process as the regions $<3100\text{ cm}^{-1}$ and $>3400\text{ cm}^{-1}$. At 3300 cm^{-1} the signal due to the direct bleaching of the $v = 0 \rightarrow 1$ transition is observed as a weak shoulder on the very strong thermalization signal (see Fig. 6.1b, note also the differences in magnitude of the overall signals in Fig. 6.1). The signal level of this shoulder is about the same as that of the bleaching at 3500 cm^{-1} and that of the induced absorption at 3100 cm^{-1} .

6.3 Population relaxation or equilibration

In Ref. [69] the second, slower process with a time constant of 0.55 ps is interpreted as the population relaxation of the O–H stretch vibrations. This interpretation is mainly based on the magnitude of the time constant of the slower process, that is quite similar to the decay time constant of $\sim 0.7\text{ ps}$ of the anti-Stokes Raman scattering signal. However, if the 0.55 ps process would indeed be the vibrational relaxation, a *decay* of a bleaching with this time constant should be observed in the frequency region $3200\text{--}3400\text{ cm}^{-1}$. Instead, a *rise* of a bleaching signal with 0.55 ps is observed in this frequency region. Hence, the 0.55 ps process does not represent the vibrational relaxation, but rather the relaxation of an intermediate state (likely the overtone of the bending vibration of H_2O) that gets populated by the relaxation of the O–H stretch vibration. As a result of this second relaxation process with $\tau_{\text{eq}} = 0.55\pm 0.05\text{ ps}$, the H_2O sample gets heated by $\sim 30\text{ K}$, which results in a decrease and a blue shift of the O–H stretch vibrational absorption band. Hence, the 0.55 ps process induces a rise of a bleaching at frequencies $<3500\text{ cm}^{-1}$, and an induced absorption at frequencies $>3500\text{ cm}^{-1}$, as is observed in Fig. 6.1 and in Chapters 4 and 5.

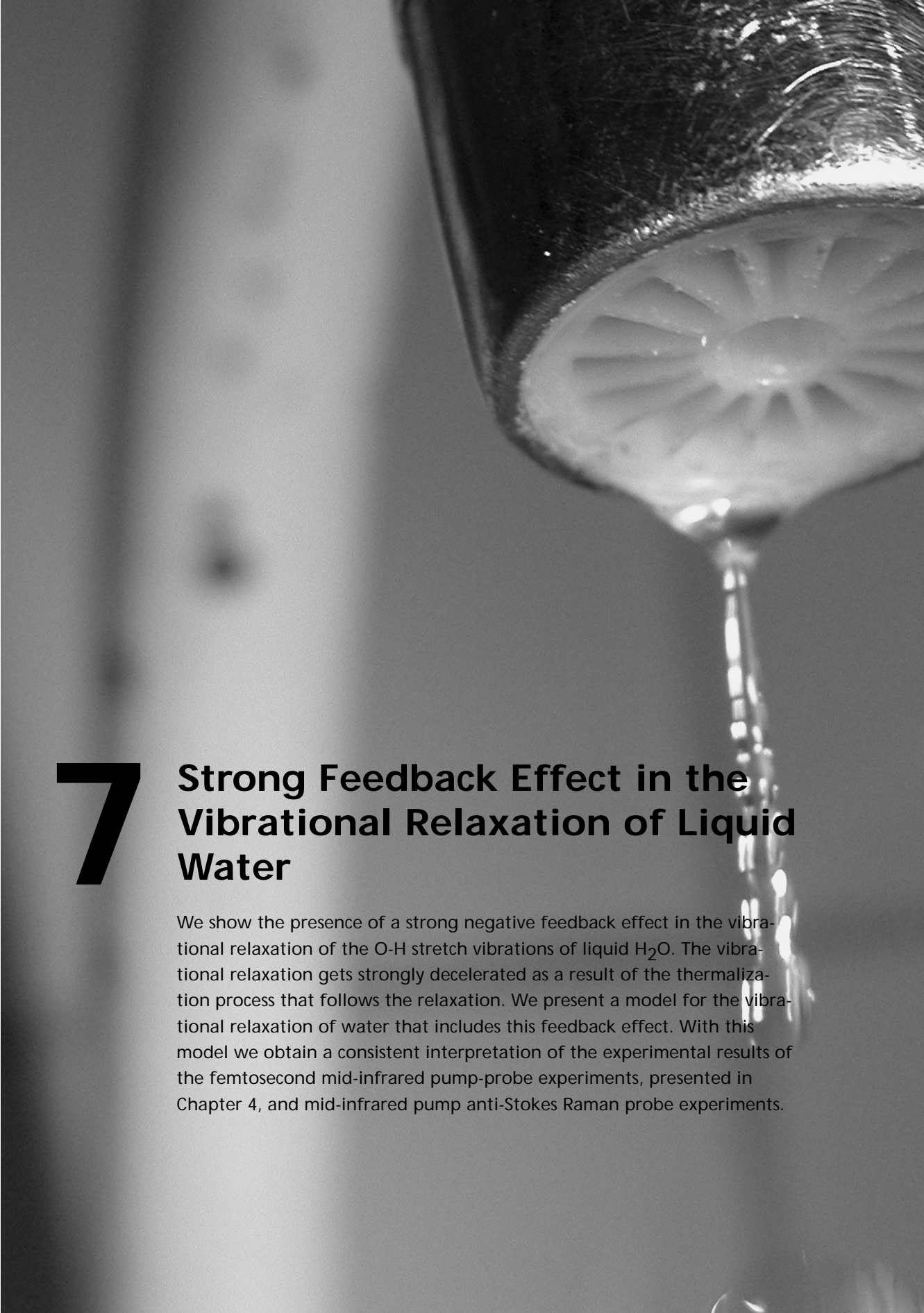
Pakoulev et al. claim that their anti-Stokes Raman measurements would be totally insensitive to the thermalization process. In our opinion this claim is not correct. Liquid H_2O possesses an extremely high density of O–H oscillators, which implies that the relaxation of an O–H oscillator will immediately affect the response of nearby O–H oscillators. In the experiments of Ref. [69], there will indeed be a strong effect of relaxing O–H vibrations on the dynamics of other excited O–H vibrations, because the infrared pulses used in these experiments are long (1.4 ps) compared to the time scales of vibrational relaxation and thermalization. Hence, a large part of the signal observed in Ref. [69] will be formed by water molecules for which the O–H spectrum

has been shifted to the blue as a result of the relaxation of molecules that were excited by the front part of the pulse. This also means that the rapid spectral blue shift observed by Pakoulev et al. likely does not represent a single spectral diffusion process, but forms the result of the consecutive action of the vibrational relaxation of room temperature water and the thermalization. Here it should also be noted that the cross-correlation of 1.8 ps of the pulses used in the experiments of Pakoulev et al. is too long to distinguish the two relaxation processes.

Following this interpretation, the rate limiting step of the blue shift is formed by the thermalization process. Indeed, the value of τ_{eq} of 0.55 ± 0.05 ps of this process is quite similar to the time constant of the blue shift of ~ 0.4 ps reported in Ref. [69]. The blueshift probably also affects the rate of vibrational relaxation of the O–H stretch vibration, which could explain why the anti-Stokes Raman signals measured in Ref. [69] show a relatively slow decay, especially at the blue side of the spectrum.

6.4 Conclusion

In conclusion, we demonstrated that the reinterpretation given in Ref. [69] of the results of previous femtosecond mid-infrared pump-probe studies is incorrect. In addition, we argued that, in view of the pulse durations used, the fast spectral blue shift with ~ 0.4 ps observed in Ref. [69] likely results from the subsequent action of the vibrational relaxation of room temperature water ($T_1 = 0.3 \pm 0.05$ ps) and a thermalization process ($\tau_{\text{eq}} = 0.55 \pm 0.05$ ps).



7 Strong Feedback Effect in the Vibrational Relaxation of Liquid Water

We show the presence of a strong negative feedback effect in the vibrational relaxation of the O-H stretch vibrations of liquid H_2O . The vibrational relaxation gets strongly decelerated as a result of the thermalization process that follows the relaxation. We present a model for the vibrational relaxation of water that includes this feedback effect. With this model we obtain a consistent interpretation of the experimental results of the femtosecond mid-infrared pump-probe experiments, presented in Chapter 4, and mid-infrared pump anti-Stokes Raman probe experiments.

7.1 Introduction

Many of the anomalous properties of liquid water (H_2O) results from its extremely high density of O–H groups and strong directional hydrogen-bonds. These high densities lead for instance to exceptionally rapid energy transfer and relaxation dynamics. As a result of the rapid resonant intermolecular (Förster) energy transfer, an excitation of the O–H stretch vibration gets rapidly delocalized over many water molecules [104].

The energy relaxation of the O–H stretch vibrations of liquid water is also very fast, as has been shown with femtosecond mid-infrared pump-probe spectroscopy [51, 52] in Chapters 4 and 5 and with mid-infrared pump anti-Stokes Raman probe experiments in Refs. [12, 69, 101]. In Chapters 4 and 5, the relaxation was observed to take place in two subsequent processes. In a first process with a time constant of ~ 300 femtoseconds, the O–H stretch vibration transfers its energy to a particular combination of accepting modes. This combination of accepting modes also relaxes, leading to an equilibration of the energy over all degrees of freedom. This equilibration takes place with a time constant of ~ 550 fs, which is very fast in comparison to other hydrogen-bonded liquids. The same process takes about 3 picoseconds for methanol and 8 picoseconds for ethanol, see Chapter 5. In the mid-infrared pump anti-Stokes Raman probe studies by the group of Dlott [69, 101] a different relaxation behavior is reported. In these studies, the excitation of the O–H stretch mode is observed to lead to a blue shift of the anti-Stokes Raman spectrum with a time constant of ~ 400 fs, and a vibrational relaxation with a time constant of ~ 700 fs, that depends on frequency [69, 101]. The observations of the mid-infrared pump anti-Stokes Raman probe studies clearly differ from what is observed in the femtosecond mid-infrared pump-probe experiments. So far these differences are not understood.

An important consequence of the delocalized character of the O–H stretch vibrations in water is that the relaxation of an excited O–H stretch vibration will affect the relaxation of other still excited O–H stretch vibrations. For pure liquid bromoform (CHBr_3), a positive feedback effect was observed for the relaxation of the C–H stretch vibration, i.e. the relaxation was observed to get accelerated with an increasing occupation of the accepting modes [22]. For water a similar feedback effect is to be expected: the vibrational relaxation and thermalization processes will lead to the excitation of modes that affect the rates of these processes. This means that the relaxation dynamics of water will be essentially different from those of an electronically excited dye molecule in dilute solution, or even of the excited O–H stretch vibration of an HDO molecule in dilute solution in D_2O .

In this Chapter, we present a model that provides a complete picture of the vibrational dynamics of the O–H stretch modes of liquid water including the feedback effect on the vibrational relaxation. We will show that this model allows for a consistent description of all the experimental observations of recent femtosecond mid-infrared pump-probe studies and mid-infrared pump anti-Stokes Raman probe studies of the

vibrational dynamics of liquid water.

7.2 Model for the vibrational relaxation of liquid H₂O

Following the results of Chapters 4 and 5, the vibrational relaxation of pure liquid H₂O occurs in two subsequent relaxation processes. In the first process the population n_1 of the excited $v = 1$ state of the O–H stretch vibration is transferred with time constant T_1 to an intermediate state. In the second process, the population n_0^* of this state relaxes with time constant τ_{eq} , leading to an increase in temperature that can change the vibrational lifetime T_1 of the first process. In view of the above, the vibrational excitation and relaxation of water can be described with the following four coupled equations:

$$\frac{dn_0}{dt} = -I_p(t)\sigma_{0\rightarrow 1}(\omega, T)n_0 + \frac{n_0^*}{\tau_{\text{eq}}}, \quad (7.1)$$

$$\frac{dn_1}{dt} = I_p(t)\sigma_{0\rightarrow 1}(\omega, T)n_0 - \frac{n_1}{T_1(T)}, \quad (7.2)$$

$$\frac{dn_0^*}{dt} = \frac{n_1}{T_1(T)} - \frac{n_0^*}{\tau_{\text{eq}}}, \quad (7.3)$$

$$\frac{dT}{dt} = \frac{bn_0^*}{\tau_{\text{eq}}}, \quad (7.4)$$

with n_0 the population of the $v = 0$ (ground) state, $I_p(t)$ the intensity profile of the pump pulse, T the temperature, $\sigma_{0\rightarrow 1}(\omega, T)$ the infrared cross-section depending on frequency ω and temperature T , and b a parameter relating the relaxed population n_0^* to a temperature increase. The cross-section $\sigma_{0\rightarrow 1}(\omega, T)$ is obtained from an interpolation of the infrared absorption spectra at 25°C and 85°C that are shown in Fig. 7.1a.

The O–H stretch vibrations of liquid H₂O show an extremely rapid spectral diffusion. This diffusion is even faster than that of a dilute solution of HDO in D₂O, because for H₂O the spectral diffusion results from both the hydrogen-bond dynamics and the rapid intermolecular (Förster) energy transfer. This latter transfer takes place with a time constant <100 fs [104]. As a result of the rapid spectral diffusion, excitation of the O–H stretch absorption band with a narrow-band pump pulse does not lead to the formation of a spectral hole [101]. In fact, already at short delays after the excitation, the observed spectral response is very similar to the linear spectrum, and shows very little dependence on the pump frequency [12, 69, 101]. The vibrational dynamics also shows little dependence on the pump frequency: very similar time constants for T_1 and τ_{eq} are observed when the O–H stretch vibration is excited at 3250 cm⁻¹ (Chapter 4) and when it is excited at 3550 cm⁻¹ (Chapter 6).

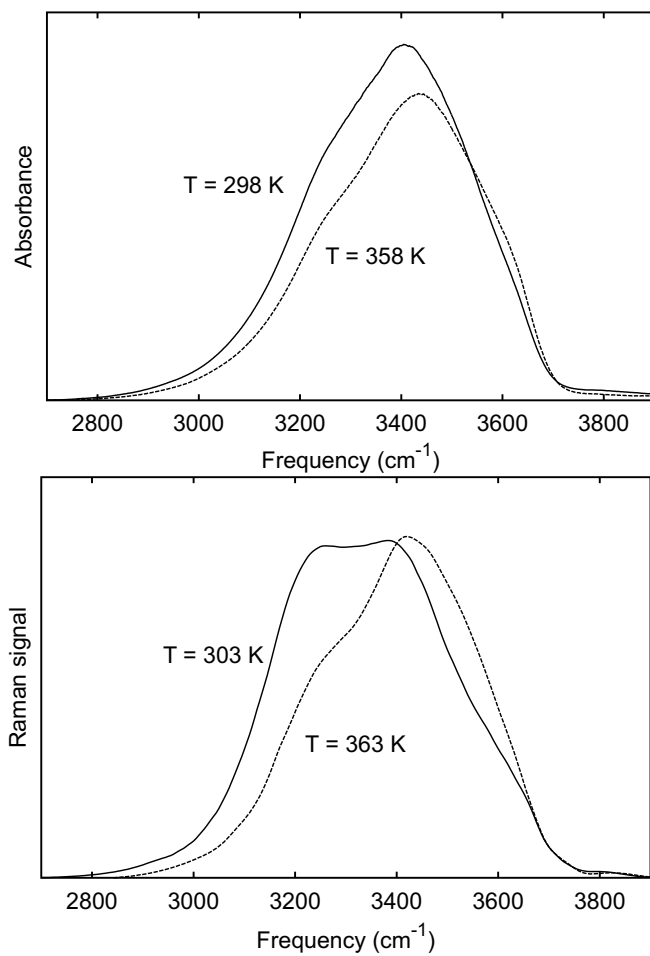


Figure 7.1. Infrared absorption spectra of liquid water at 25 and 85 °C (a), and Raman (Stokes) spectra of liquid water at 30 and 90 °C (b).

Because of the rapid spectral equilibration of liquid H₂O, the experimentally observed T_1 represents an average over the spectral distribution of O–H oscillators. The experimentally observed relaxation rate $T_1^{-1}(T)$ can thus be approximated by integrating over the spectral distribution $S(\omega, T)$ of O–H oscillators multiplied by the frequency-dependent relaxation rate $T_1^{-1}(\omega)$ that would be observed if there were no spectral diffusion:

$$1/T_1(T) = \int d\omega S(\omega, T) T_1^{-1}(\omega) / \int d\omega S(\omega, T), \quad (7.5)$$

The experimentally observed value of T_1 will depend on temperature T because the spectral distribution $S(\omega, T)$ depends on temperature. In the calculations we approximate the temperature-dependent spectral distribution with the cw Raman spectrum $R(\omega, T)$. A similar temperature dependence of T_1 is obtained when the calculations are performed when the temperature-dependent infrared absorption spectrum $\sigma(\omega, T)$ is used to describe the spectral distribution.

The use of Equation 7.5 to approximate the experimentally observed T_1 does not critically depend on the spectral diffusion time constant. The equation can be used provided that the spectral diffusion time is shorter than the durations of the pulses used in the experiment. There is no lower limit to the spectral diffusion time constant: Equation 7.5 can be used even if the spectral diffusion is so fast that the spectrum would be significantly homogeneously broadened.

From measurements on many hydrogen bonded O–H groups the following empirical relation was derived [59]:

$$T_1(\omega) = a(\omega - \omega_{\text{OH,g}})^{-1.8}, \quad (7.6)$$

with a a constant, ω the O–H stretch vibrational frequency of the hydrogen-bonded O–H group, and $\omega_{\text{OH,g}}$ the vibrational frequency of the same group in the gas phase. Equation 7.6 is also valid for aqueous systems. For a solution of HDO in D₂O the value of T_1 of the O–H stretch vibration was observed to increase from 750 fs at 273 K to 950 fs at 373 K, and to decrease to 380 fs when the HDO:D₂O liquid solution was frozen to ice [108]. For pure liquid H₂O, T_1 was observed to increase from 260 fs at 293 K to 320 fs at 353 K [51], see Chapter 4. These changes in T_1 are all accurately described by the combination of Equations 7.5 and 7.6.

The coupled Equations 7.1-6 cannot be solved analytically because T_1 depends on temperature, and thus on time. Hence, we solve these equations numerically using a fourth-order Runge-Kutta scheme. In addition, because the absorption spectrum, the Raman spectrum, and T_1 all depend on temperature, the shape of the focus of the infrared pump pulse should be accounted for. Therefore, Equations 7.1-6 are solved for a Gaussian distribution of pump pulse intensities $I_p(t)$. The final calculated result is the sum of all responses within this distribution. The results of the model are fitted to the experimental results of Chapter 4 and Ref. [69]. Most of the parameters

entering the model are obtained from independent experimental results. In calculating T_1 at different temperatures, we use for $\omega_{\text{OH,g}}$ the average frequency of the symmetric and the antisymmetric O–H stretch vibration of water in the gas phase: $\omega_{\text{OH,g}} = 3706 \text{ cm}^{-1}$. The Raman spectra $R(\omega, T)$ at different temperatures are obtained from an interpolation of cw (Stokes) Raman spectra reported in the literature. In this interpolation, we used the Raman spectra measured at 30°C and 90°C of Ref. [83]. These spectra are shown in Fig. 7.1b. The parameter a that enters Equation 7.6 is chosen such that $T_1 = 0.3 \text{ ps}$ at 298 K, and the equilibration time τ_{eq} is set to a temperature independent value of 0.55 ps.

7.3 Results and comparison with experiments

In the studies on the vibrational relaxation of liquid water, the O–H stretch vibrations ($3000\text{--}3600 \text{ cm}^{-1}$) were resonantly excited with an intense mid-infrared pulse. This pulse had different parameters in the different studies reported. In Chapters 4 and 5, the pulse had a duration of $\sim 200 \text{ fs}$ and an energy of $\sim 10 \mu\text{J}$ [51, 52]. In the mid-infrared pump anti-Stokes Raman probe studies the pulse had a duration of $\sim 1.4 \text{ ps}$ and an energy of $40\text{--}50 \mu\text{J}$ [12, 69], or a duration of $\sim 0.7 \text{ ps}$ and an energy of $\sim 25 \mu\text{J}$ [101]. The excitation by the intense infrared pulse results in a bleaching of the fundamental $v = 0 \rightarrow 1$ transition and in an induced absorption of the $v = 1 \rightarrow 2$ transition. This $v = 1 \rightarrow 2$ transition is redshifted by $\sim 250 \text{ cm}^{-1}$ with respect to the $v = 0 \rightarrow 1$ transition [104]. The reported experiments differed in their method of probing. In the Chapters 4 and 5, the infrared transmission changes were probed with a weak, time-delayed probing pulse with a duration of $\sim 200 \text{ fs}$. In the mid-infrared pump anti-Stokes probe experiments of Refs. [12, 69, 101] the residual population of the $v = 1$ state of the O–H stretch vibration was probed by measuring the anti-Stokes Raman spectrum with an intense delayed visible pulse with a duration of $\sim 1.4 \text{ ps}$ [12, 69] or $\sim 0.7 \text{ ps}$ [101].

To enable a comparison between the model and the results of the mid-infrared pump-probe experiments, the calculated populations n_0 and n_1 should be transferred into transient changes in the infrared absorption $\Delta\alpha(\omega, t)$:

$$\begin{aligned} \Delta\alpha(\omega, t) = & n_1(t)\{\sigma_{1\rightarrow 2}(\omega, T(t)) - \sigma_{0\rightarrow 1}(\omega, T(t))\} + \\ & n_0(t)\sigma_{0\rightarrow 1}(\omega, T(t)) - n_0(-\infty)\sigma_{0\rightarrow 1}(\omega, T = 298\text{K}). \end{aligned} \quad (7.7)$$

The terms at the right hand side represent the induced excited state $v = 1 \rightarrow 2$ absorption, the $v = 1 \rightarrow 0$ stimulated emission, the modified ground state $v = 0 \rightarrow 1$ absorption, and the reference ground state absorption, respectively.

In Fig. 7.2 femtosecond pump-probe data are shown obtained for a sample of pure H_2O at four different probe frequencies. The pump pulses had a central frequency of 3250 cm^{-1} . The solid curves are calculated with the model of the previous section. At a probe frequency of 3100 cm^{-1} , the signal is initially dominated by the induced

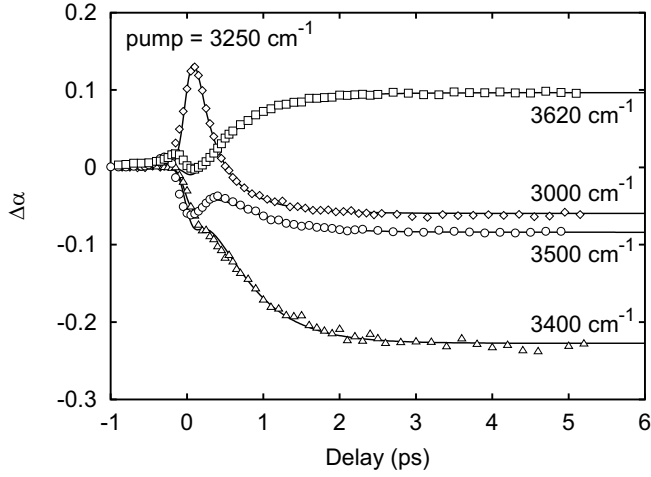


Figure 7.2. Femtosecond mid-infrared pump-probe scans of liquid water at 298 K. Shown is the absorption change as a function of delay at four different probe frequencies. The central frequency of the pump is 3250 cm^{-1} . The solid curves are calculated with the model described in the text.

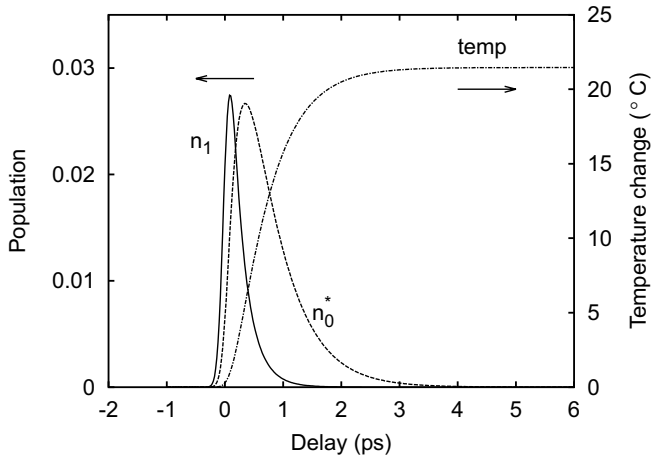


Figure 7.3. Calculated populations n_1 of the excited $v = 1$ state and n_0^* of the intermediate state as a function of delay. These populations are calculated with the pulse parameters of the femtosecond mid-infrared pump-probe experiments shown in Fig. 7.2. Also shown is the increase in temperature that results from the relaxation of the intermediate level.

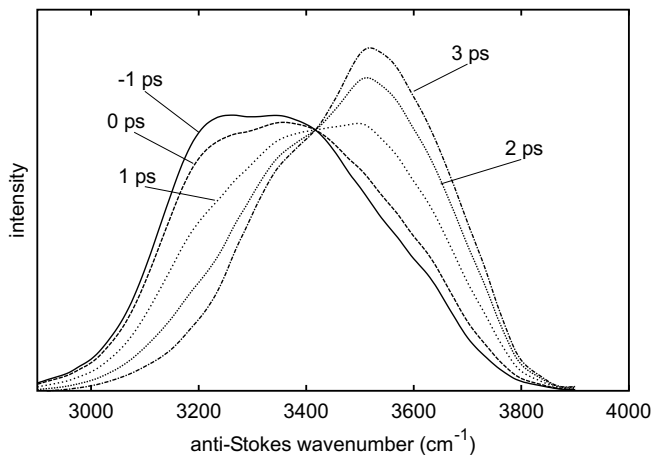


Figure 7.4. Calculated anti-Stokes Raman scattering spectra at different delays. The spectra are calculated using the model described in the text and the pulse parameters of the experiments of Ref. [69].

$v = 1 \rightarrow 2$ absorption that decays to zero with T_1 . At longer delays, the signal further decays to a decreased absorption due to the temperature increase that results from the thermalization process. At 3400 cm^{-1} , the signal is dominated by the thermalization process that at this frequency leads to a large decrease in absorption. The initial bleaching of the $v = 0 \rightarrow 1$ transition is only observed as a small shoulder. The signal at 3500 cm^{-1} most clearly shows that the relaxation involves two subsequent processes. First there the bleaching of the $v = 0 \rightarrow 1$ decays with T_1 , then there is again a decrease in absorption due to the thermalization with τ_{eq} . At 3620 cm^{-1} the signal is dominated by the thermalization effect that at this frequency leads to a final induced absorption. It is clear that the model provides a quantitative description of all thermally induced transmission changes. In Fig. 7.3 the time-dependent populations n_1 and n_0^* are shown together with the time-dependent change in temperature at the maximum intensity of the pump focus.

In Fig. 7.4 calculated anti-Stokes Raman scattering spectra $I_A(\omega, t)$ at different delays are presented. These spectra are calculated using $I_A(\omega, t) \sim n_1(t)R(\omega, T)$. The anti-Stokes Raman spectrum is constructed from an interpolation of the continuous wave Raman spectra shown in Fig. 7.1b. In this calculation we used the pulse parameters used in the experiments described in Ref. [69]. To get an accurate description of the shape of the spectra measured by Pakoulev et al. [69], we had to shift the Raman spectrum at 90°C by 70 cm^{-1} to higher frequencies (see next section). As in Ref. [69], all spectra were normalized to constant area. The calculated spectral dynamics show

great similarity with the transient spectra shown in Fig. 5b of Ref. [69]. The spectra clearly shift to the blue with increasing delay. In Refs. [69] and [101] this blue shift was interpreted as a single spectral diffusion process with a time constant of ~ 0.4 ps. However, here we find that this blue shift is in fact not a single process but the result of the consecutive action of the vibrational relaxation of room temperature water and the thermalization. It should be realized that the cross-correlations of 1.8 ps [69] and 1.1 ps [101] of the infrared pump pulse and the visible probing used in Refs. [69, 101] are too long to resolve these two processes. Therefore, the vibrational relaxation and thermalization are observed as a single process giving rise to a blue shift. This also means that the blue shift is not the result of a vibrational Stokes shift within the excited $v = 1$ state [69, 101], but rather a shift of the complete spectrum to higher frequencies. This mechanism for the blue shift also explains the observation reported in Ref. [101] that the magnitude of the blue shift depends on the excitation intensity, i.e. on the amount of energy dissipated. In the case of a vibrational Stokes shift, the magnitude of the shift should not depend on the excitation intensity, whereas in the case of a thermal shift such a dependence is obvious.

The rate limiting step of the blue shift is the thermalization process. Indeed, the value of τ_{eq} of 0.55 ± 0.05 ps of this process is similar to the time constant of the blue shift of ~ 0.4 ps reported in Ref. [69]. It is even strikingly similar to the time constant of 0.55 ps reported for the rise of a blue-shifted absorption component in Ref. [101]. In Ref. [101] this blue-shifted component is interpreted as being a sub-band of the absorption spectrum of water. From our calculations we find that the apparent rise of a blue-shifted component with $\tau \sim 0.55$ ps can be very well explained from a thermally induced blue shift of the *complete* O–H spectrum. Moreover, if there really would exist a blue-shifted sub-band, then pumping of this band should inevitably lead to population transfer to red-shifted sub-bands, which is not observed in Ref. [101].

In Fig. 7.5, the calculated delay dependence of the anti-Stokes Raman scattering signal $I_A(\omega, t)$ at particular frequencies ω is shown. These delay curves are also calculated with the pulse parameters of the experiments reported in Ref. [69]. The decays represent the combined action of vibrational relaxation of the $v = 1$ state of the O–H stretch vibration and of the thermally induced spectral shift to the blue. The calculated curves are in excellent agreement with the experimental results of Fig. 3b of Ref. [69]. In Fig. 7.6 the time-dependent populations n_1 and n_0^* are shown together with the time-dependent change in temperature at the maximum intensity of the pump focus. The final calculated increase in temperature amounts to 78 K which is in excellent agreement with the estimated experimental temperature increase of the experiments of Ref. [69].

The solid lines in Fig. 7.5 represent exponential fits to the points that are calculated with the model of the previous section. At 3200 cm^{-1} the decay obtained with the model can be quite well fitted with an exponential decay with a time constant of 0.7 picoseconds. At 3520 cm^{-1} , the best fit is obtained with an exponential with a time constant of 1.1 picoseconds. These values are surprisingly long in comparison to the

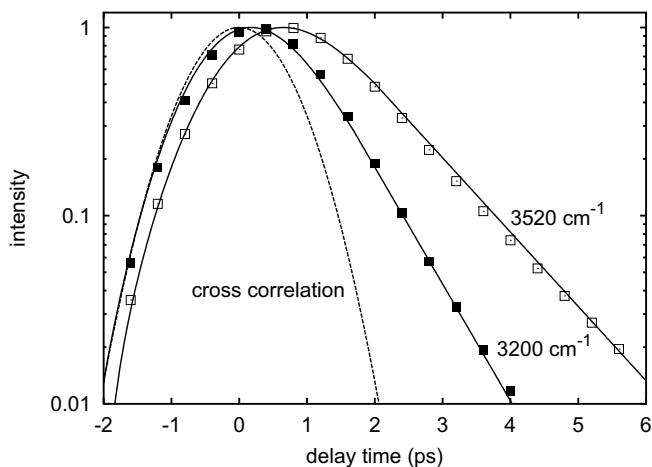


Figure 7.5. Calculated anti-Stokes Raman scattering signal at 3200 cm^{-1} (solid squares) and 3520 cm^{-1} (open squares) as a function of delay between an exciting infrared pulse and a probing visible pulse. The calculation is performed using the pulse parameters of Ref. [69]. Also shown is the cross-correlation of the infrared pump and visible probe with a full-width-at-half-maximum of 1.8 ps (dashed line). The calculated signals can be well described by convolutions (solid lines) of the cross-correlation function and exponential decays with time constants of 0.7 and 1.1 ps for the signals at 3200 and 3520 cm^{-1} , respectively.

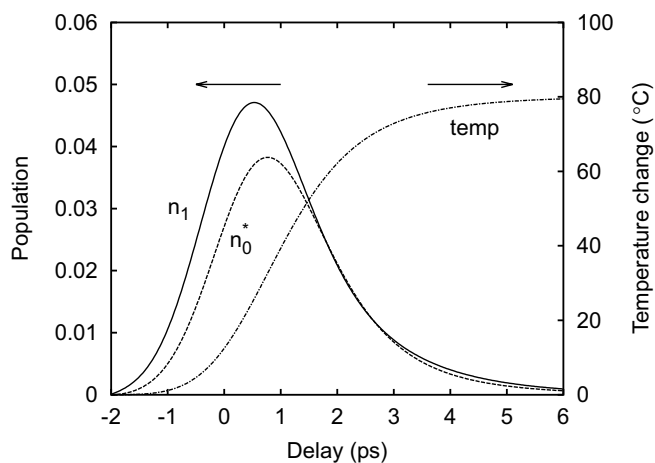


Figure 7.6. As Fig. 7.3, but calculated for the pulse parameters used in the time-resolved anti-Stokes Raman spectra of Ref. [69].

value of T_1 of 0.3 ps at 298 K. This slowing down is largely due to the increase of T_1 that results from the strong increase in temperature. This increase of T_1 also explains the observation in Ref. [101] that a doubling of the pump pulse energy led to an increase of the observed vibrational lifetimes with 15%. This directly shows that the claim in Ref. [69] that the dynamics observed in the anti-Stokes Raman experiments would be insensitive to the thermalization process, is not correct. In fact, the dynamics observed are very sensitive to the thermalization and the negative feedback effect: the negative feedback can lead to an increase of T_1 by a factor of four.

The effect of the thermalization on T_1 will be much smaller in the femtosecond mid-infrared pump-probe experiments shown in Chapters 4 and 5, because the pulses were significantly shorter than the thermalization time. In Fig. 7.3 it is seen that there is indeed very little population n_1 left at the delay at which the temperature rise becomes significant and starts to affect the spectrum and T_1 time constant. In contrast, in the anti-Stokes Raman scattering experiments of Refs. [69] and [101] the used infrared pump pulses are longer (1.4 and 0.7 ps) than the thermalization time (0.55 ps), so that many O–H stretch vibrations are excited for which the rate of vibrational relaxation has been changed due to the relaxation of excitations by the front wing of the pump pulse. In Fig. 7.6 it is indeed clearly seen that the population n_1 is still significant at delay times at which there already is a substantial increase in temperature.

At the blue side (3520 cm^{-1}), the decay of the anti-Stokes Raman signal is slower (1.1 ps) than at the centre and at the red side of the spectrum. This frequency dependence seems to be in conflict with the concept of a rapid spectral equilibration of the O–H stretch excitation and a frequency-independent effective T_1 . However, the frequency dependence of the decay time of the calculated results of Fig. 7.5 and the experimental results of Refs. [69, 101] does not result from the inhomogeneous character of the O–H absorption spectrum, but from another type of inhomogeneity. The excitation by the infrared pump pulse leads to a spatial distribution of dissipated energies and thus of temperature increases in the focus. At the highest intensities, the temperature increase, the spectral blue shift, and the time constant T_1 , all have the largest values. Hence, the signal at 3520 cm^{-1} is dominated by the part of the focus where the infrared pump pulse is most intense, whereas the signal at 3200 cm^{-1} represents the regions of the focus where the pump is less intense. In the experiments of Refs. [69] and [101] the probe focus ($400\text{ }\mu\text{m}$) was of about the same size as the pump focus ($370\text{ }\mu\text{m}$) so that the measured signal indeed contains contributions from regions with strongly different pump intensities. An additional minor effect that contributes to the frequency dependence of the decay is the dynamics of the spectral blue shift. In the experiments reported in Refs. [69] and [101] the vibrational relaxation is significantly slowed down due to the increase in temperature. Hence, the spectral blue shift takes place on the same time scale as the vibrational relaxation and thus leads to an apparent faster decay at the red side and a slower decay at the blue side of the spectrum. In the femtosecond mid-infrared pump-probe experiments the effect

of the blue shift on the observed decay times is much smaller, because in those experiments the vibrational relaxation is almost finished before the blue shift due to the thermalization occurs (Fig. 7.3).

7.4 Discussion

The negative feedback effect is not a minor effect and can lead to an increase of T_1 from ~ 300 fs to ~ 1.1 ps. The effect is so strong because of the large blue shift of the spectrum that results from the thermalization of the excitation energy. It should be noted that the experimentally observed blue shift [69, 101] is in fact larger than one would expect from the temperature dependence of the cw Raman spectrum of water [83]. For an increase in temperature of ~ 80 K, the anti-Stokes Raman spectra measured by Pakoulev et al. shifts ~ 70 cm^{-1} more to the blue than the ordinary cw Raman spectra. The authors of Ref. [69] suggest that the large blue shift could result from the excitation of specific other modes like bending and torsion vibrations. However, in general the excitation of anharmonically coupled modes leads to a *red* shift of the O–H stretch vibrational frequency and not to a blue shift (the hydrogen bond is an exception). In addition, the subsequent relaxation of these modes is expected to lead to spectral redshifts on a picosecond time scale, which are not observed. A more likely origin of the large thermal blue shift is that the water has not yet completely equilibrated after the dissipation of the infrared pump energy. The frequency of the O–H stretch vibration is determined by the length and angle of the O–H \cdots O hydrogen bond, and increases with increasing O \cdots O distance and angle between the O–H and O \cdots O coordinates [58, 67, 77]. In the case of heat dissipation on a picosecond time scale, the volume, and thus the average oxygen-oxygen distance cannot change. Hence, dissipation of heat in a constant volume likely will lead to a very strong bending of the hydrogen bonds. At longer time scales, the oxygen-oxygen distance can expand, and the O–H and O \cdots O coordinates will get better aligned again. Hence, the strongly bent hydrogen bonds that are generated in the first picoseconds after heat dissipation, are likely weaker than the lengthened, but only slightly bent hydrogen bonds that result after volume expansion. In a recent molecular dynamics study it was shown that the strength of the hydrogen-bond interaction is indeed strongly dependent on the angle of the hydrogen bond [77]. The strong relation between hydrogen-bond angle and the strength of the hydrogen bonds can also be illustrated by comparing water to ice. Going from ice to water, the volume gets less, which implies that the average O \cdots O distance decreases, but in addition the almost perfect alignment of the O–H bond and the O \cdots O coordinate of ice is lost. The overall effect is a weakening of the hydrogen-interaction, which results in a blue shift of the O–H frequency of ~ 150 cm^{-1} . Hence, the anomalously large blue shift of the anti-Stokes Raman spectra observed in Ref. [69] is likely caused by the strong bending of the hydrogen bonds that in turn results from the dissipation of a large amount of energy in a constant volume.

7.5 Conclusions

The O–H stretch vibrations of liquid water are delocalized as a result of the strong intermolecular coupling and high density of the water molecules. An important consequence of this delocalization and high density is that there is a strong negative feedback effect on the relaxation of the O–H stretch vibrations. The heat dissipated in the vibrational relaxation and subsequent thermalization leads to a deceleration of the relaxation and a blue shift of other, still excited O–H stretch vibrations. This effect can lead to an increase of T_1 by a factor of four. We present a model for the vibrational relaxation of liquid water that includes this negative feedback effect.

In recently reported mid-infrared pump anti-Stokes Raman probe experiments [69, 101], the pulses used were longer than the time constants of the vibrational relaxation ($T_1 = 0.3 \pm 0.05$ ps at 298 K) and the thermalization ($\tau_{\text{eq}} = 0.55 \pm 0.05$ ps), leading to a strong negative feedback effect on the relaxation rate. We also find that the fast and large spectral blue shift of the anti-Stokes Raman spectrum reported in Refs. [69, 101] can be well explained from the subsequent action of the vibrational relaxation and the thermalization process. This explanation is confirmed by the observations that both the blue shift and T_1 increase with increasing energy of the excitation pulse [101]. The dependence of the blue shift and relaxation rate on the excitation energy also leads to a frequency dependence of the vibrational relaxation, because of the inhomogeneity of the dissipated energy in the focus of the pump pulse.

8

Hydrogen Bond Mediated Energy Transfer in Embedded Water Molecules

In this Chapter, we present results on embedded water molecules dissolved in a mixture of acetone and carbon tetrachloride. From both vibrational relaxation and anisotropy decay measurements, we conclude that two processes occur: the transfer of excitation energy from one OH-group to the other and the formation and breakage of hydrogen-bonds. It is shown that an intermediate state exists in which the water molecule has two hydrogen bonds, and in which the excitation energy is delocalized over the OH-groups.

8.1 Introduction

As stated in the Introduction, understanding water means understanding hydrogen-bonding in liquids. The study of the OH-stretch vibration of water is complicated due to the ultrafast energy equilibration with a time constant of 550 fs, as shown in Chapters 4 and 5, which stems from the large density of OH-oscillators and the strong inter- and intramolecular coupling present in liquid H₂O. Therefore, previous studies were mainly focused on dilute solutions of HDO in D₂O [20, 63, 64, 103, 104, 106, 108]. In this case, a single OH-oscillator is surrounded by OD-groups which makes it possible to study only the influence of the hydrogen bonding network on the OH-stretch oscillator, because there is no intra- and intermolecular OH-OH coupling. Recently, the rotational anisotropy decay was measured on pure water in a femtosecond mid-infrared pump-probe study [104]. The anisotropy is a measure for the degree of polarization induced by excitation of OH-stretch oscillators by the pump pulse. Because the transition dipole moments of the symmetric and antisymmetric OH-stretch vibration are orthogonal (see Figure 1.2), the anisotropy decay forms a measure for the population redistribution between these two modes. The anisotropy decay was observed to be instantaneous (<100 fs). This means that in pure water the vibrational energy is delocalized within the pulse duration. However, due to the large density of OH-groups and the ultrafast time scale, the intramolecular redistribution could not be distinguished from the intermolecular energy transfer.

In contrast to these measurements, the intramolecular coupling can still be studied in water monomers in apolar solutions [23, 26], because there is no influence of the hydrogen-bonding network on the OH-stretches. In a picosecond pump-probe study [26] it was shown that excitation of the antisymmetric stretch mode in a water monomer dissolved in an apolar solvent led to a fast (few ps) population redistribution with the symmetric stretch mode. It should be emphasized, that the pulse duration in this experiment was 14 ps.

Here we present a study on water-acetone complexes in apolar solution. This system enables us to study an isolated H₂O molecule with hydrogen bonds to acetone molecules. It allows for a study of both the intramolecular redistribution and the influence of hydrogen-bonding on the OH-stretch dynamics.

8.2 Experimental

The experimental setup used for the experiments described in this thesis has two major changes with respect to the setup described in Chapter 3.

First, the detection of the signal has been changed. The last mirror in the probe path (see Fig. 3.4) is replaced by a wedged CaF₂ window. The reflection from the back side forms the reference beam, which is now also focussed into the sample, but does not overlap with the pump beam. In order to measure the rotational anisotropy (see Section 3.2), the polarization of the probe beam was set at 45 degrees with

respect to the pump beam. After the sample, an infrared beam splitter splits the probe beam into two parts. Due to polarizers in both pathways, two beams with polarization components perpendicular and parallel to the pump polarization are generated. These two beams, together with the reference beam, are focussed by a 100 mm CaF_2 lens on the entrance split of an imaging spectrograph. At the image plane three MCT detector arrays consisting of 32 pixels are placed above each other. In the experiments the arrays cover a spectral width of approximately 400 nm.

The measured intensities $I(\omega)$ are amplified and sent to a computer via an A/D-converter. In order to compensate for the pulse-to-pulse intensity fluctuations in the probe beam, the reference intensity $I_{\text{ref}}(\omega)$ is measured. Using a chopper, both the transmission of the probe beam in the presence of the pump beam ($T(\omega)$), and in the absence of the pump beam ($T_0(\omega)$) are measured. The transmission change $\ln(T/T_0)$ is calculated as a function of delay between pump and probe pulse, where $T(\omega)=I(\omega)/I_{\text{ref}}(\omega)$ and $T_0(\omega)=I_0(\omega)/I_{\text{ref}}(\omega)$.

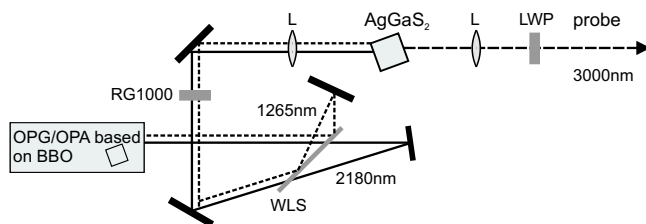


Figure 8.1. Generation of the probe pulse. DM=dichroic mirror, RG1000=longwave pass 1000nm, L=lens, LWP=longwave pass 2500nm, AgGaS_2 =nonlinear crystal, black bars represent gold mirrors.

Secondly, the probe pulse is generated in a different way, as is depicted in Figure 8.1. An OPG/OPA-stage generates signal (1265 nm) and idler pulses (2180 nm). Difference frequency generation (DFG) in an AgGaS_2 -crystal leads to pulses tunable up to 10 μm . A major advantage of using AgGaS_2 is that the generated pulses have a much larger bandwidth than pulses generated via parametric amplification in KTP. With these pulses, we can fully make use of the advantages of spectrally resolving the probe. The spectral width of the probe pulses used is approximately 300 cm^{-1} (FWHM) and the duration is 100 fs.

The sample was prepared from a 4.0 mol/l solution of acetone (CH_3COCH_3 , Biosolve, 99.8%) in carbon tetrachloride (CCl_4 , Fluka, 99.5%). Water (Lichrosolv, Merck) was added to a concentration of 0.4 mol/l. For the HDO samples, liquid H_2O was mixed in a 1:10 ratio with D_2O . The measurements were performed on a 500 μm thick sample kept in between two CaF_2 windows. The transmission of the sample is

typically 10% at 3520 cm^{-1} . In order to avoid the accumulation of heat produced by the pump pulses, the sample is rotated.

8.3 Linear absorption spectrum

The linear absorption spectra for the water-acetone complexes in carbon tetrachloride are depicted in Figure 8.2 for HDO and in Figure 8.3 for H_2O molecules. In case of HDO molecules, the OH-group is hydrogen-bonded to an acetone molecule, or it is not. In the latter case, the OH-stretch vibration is expected to behave similar as in the gas phase, i.e. it has a narrow absorption band at a high frequency. These free OH-groups are responsible for the peak at 3680 cm^{-1} . We attribute the broad absorption band at 3530 cm^{-1} to hydrogen-bonded OH-groups. The absorption band for hydrogen-bonded molecules is expected to undergo a red-shift and a broadening, as is indeed observed.

For H_2O molecules, the absorption spectrum has a richer structure. We again observe peaks at about 3520 and 3690 cm^{-1} . In analogy with the HDO molecule, we attribute these peaks to water molecules that only have one hydrogen-bond (see Fig 8.3, type A). If both OH-groups are hydrogen-bonded, the possible vibrations are the antisymmetric (ν_{as}) and the symmetric stretch mode (ν_s). We attribute the shoulder in the absorption spectrum at 3610 cm^{-1} to the antisymmetric stretch mode. The symmetric stretch mode is hidden underneath the broad band at 3520 cm^{-1} , which is in close analogy with the gas phase, where the symmetric stretch mode is shifted 100 cm^{-1} to the red with respect to the antisymmetric band[35]. Furthermore, the symmetric stretch mode is expected to have a smaller cross-section than the antisymmetric stretch mode. Hence, both the symmetric stretch of the doubly hydrogen-bonded and the hydrogen-bonded OH-stretch of the singly hydrogen-bonded water molecule absorb at 3520 cm^{-1} , but the major contribution at this frequency stems from the singly hydrogen-bonded OH-groups.

8.4 Vibrational and orientational relaxation

8.4.1 Transient spectra

In order to gain insight in the vibrational relaxation behavior of the H_2O molecule, we first present the results for the HDO molecule. Figure 8.4a shows the transient spectra for HDO after pumping at 3530 cm^{-1} , the frequency of the hydrogen-bonded OH-group. We observe a broad bleaching band around the pump-frequency and an asymmetrically shaped induced $1\rightarrow 2$ absorption at 3350 cm^{-1} . This implies that the anharmonicity for this system is 180 cm^{-1} .

Figure 8.4b shows the transient spectra after pumping of the free OH-stretch mode of the HDO sample. Immediately after excitation, bleaching is observed at the pumping frequency (3680 cm^{-1}), which decays as a function of time. At the

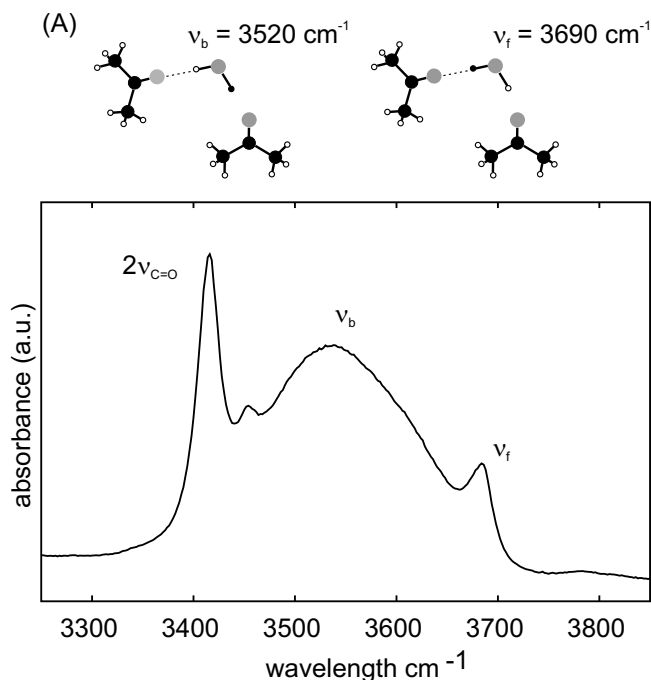


Figure 8.2. For HDO molecules, there is only one OH-stretch vibration that is either hydrogen-bonded (ν_b) or free (ν_f). Depicted is the absorption spectrum for the dilute solution of acetone-water complexes in CCl_4 . The narrow peak at 3420 cm^{-1} stems from the first overtone of the $\text{C}=\text{O}$ stretch vibration of acetone.

frequency of the hydrogen-bonded OH-groups (3530 cm^{-1}), however, an ingrowth of the bleaching is observed, which then decays for larger delay times. The induced absorption is found at 3350 cm^{-1} . Note that, for large delay times, the transient spectrum is similar to that of Fig 8.4a; the absolute signal, however, is much smaller.

The transient spectra for the H_2O molecules are displayed in Figure 8.5. The upper panel shows the results after pumping both the symmetric and hydrogen-bonded stretch mode at 3520 cm^{-1} . We observe a bleaching for frequencies higher than 3450 cm^{-1} and induced absorption for frequencies lower than this value. The bleaching shows the fingerprints of the linear absorption spectrum (Fig. 8.3): bleaching features appear at 3520 , 3610 and 3690 cm^{-1} . The induced absorption band is found at 3350 cm^{-1} , similar as in HDO. At the red side of this band at about 3180 cm^{-1} a smaller induced absorption feature is visible.

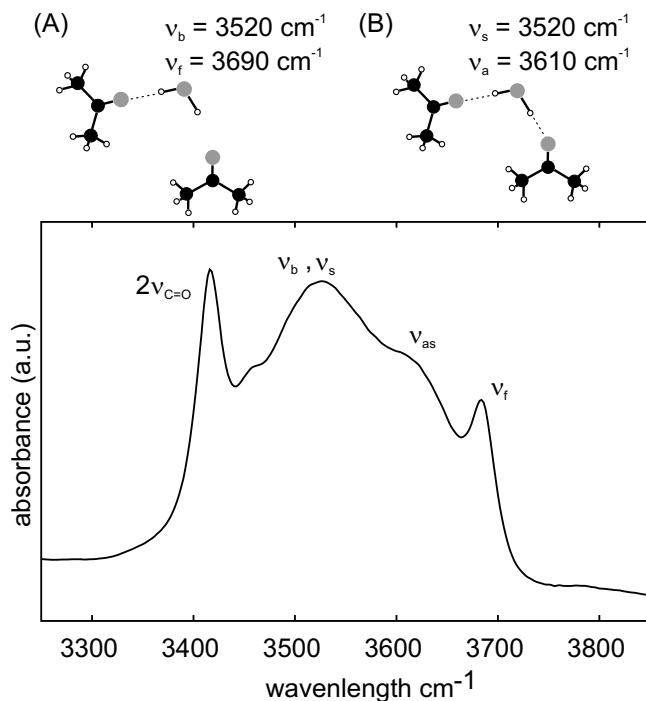


Figure 8.3. There exist two types of H₂O molecules in solution. Part of the H₂O molecules only has one hydrogen bond (type A), which gives rise to a hydrogen-bonded (ν_b) and a free (ν_f) OH-stretch mode. When both OH-groups are hydrogen bonded (type B), symmetric (ν_s) and antisymmetric (ν_a) OH-stretch modes exist. The latter absorb at 3520 and 3610 cm^{-1} , respectively. The peaks in the absorption spectrum are attributed to the four water vibrations, the narrow peak at 3420 cm^{-1} belongs to acetone.

In Figure 8.5b the transient spectra are shown for pumping the antisymmetric stretch mode (3610 cm^{-1}). At a delay of 0.4 ps, a large bleaching signal is observed at the pumping frequency, while the bleaching at 3520 cm^{-1} is negligible. For larger delay times, however, this band increases and then decays back to zero. The induced absorption is found to be centered around 3350 cm^{-1} . Furthermore, a small red-shifted induced absorption band is observed at the same frequency as in Fig. 8.5a.

Figure 8.5c displays the transient spectra after pumping the free OH-group at 3690 cm^{-1} . Here, instantaneous bleaching is observed at the pumping frequency. At 3520 cm^{-1} , bleaching is already present at short delay times. It shows an ingrowth and subsequently a decay. The response at 3610 cm^{-1} is zero for short delay times

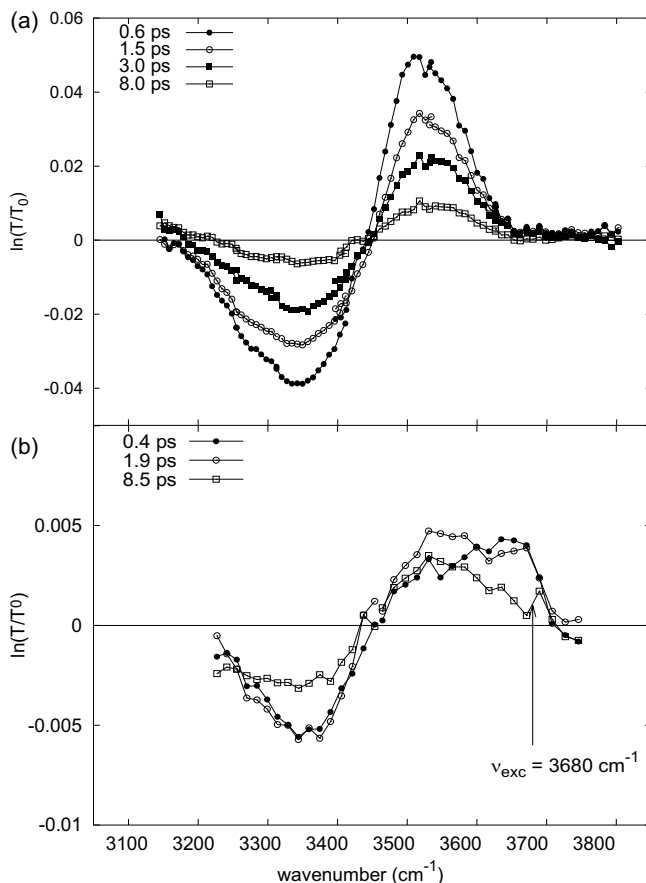


Figure 8.4. Transmission change for the HDO molecule as a function of probe frequency for different delay times after pumping at (a) 3530 cm^{-1} and (b) 3680 cm^{-1} .

and grows in for longer delay times. The induced absorption peaks at 3350 cm^{-1} and also shows an ingrowth with time. The side band at 3180 cm^{-1} is again observed.

8.4.2 Delay time scans

Figure 8.6 shows delay time scans for pumping the HDO sample at the ν_b frequency of 3530 cm^{-1} and probing in the center of the 0 \rightarrow 1 and 1 \rightarrow 2 band (upper two curves) and a delay time scan for pumping at 3680 and probing at 3530 cm^{-1} (lower curve).

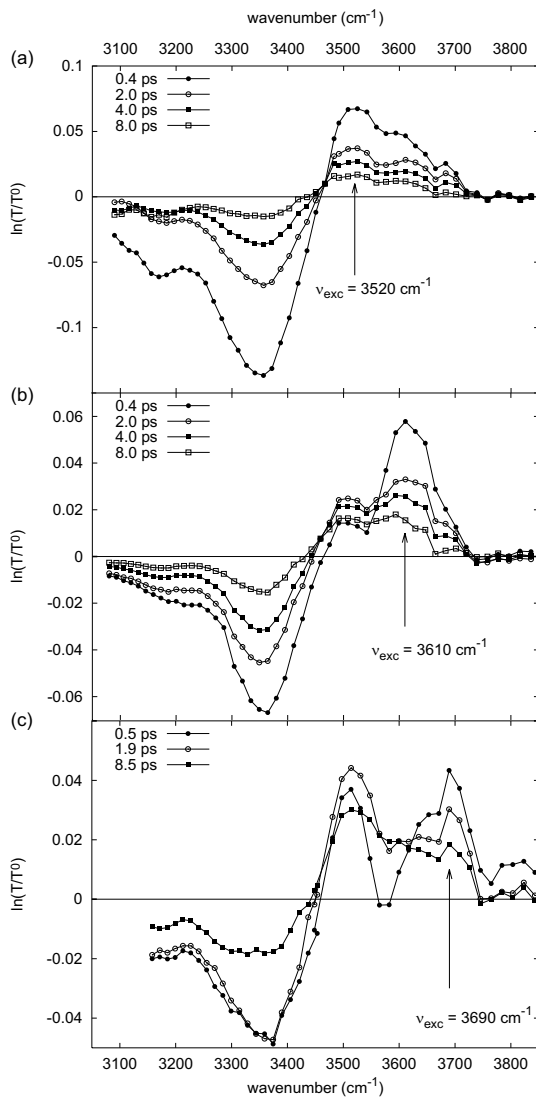


Figure 8.5. Transient spectra for H₂O at different delay times obtained after pumping (a) the symmetric and the hydrogen-bonded stretch mode at 3520 cm⁻¹, (b) the antisymmetric stretch band at 3610 cm⁻¹ and (c) the free OH-stretch band at 3690 cm⁻¹.

The upper two scans show bi-exponential decay dynamics with time constants of 1.3 ± 0.4 and 6.3 ± 0.5 ps. In the lower curve, a slow rise with a time constant of 1.3 ps is first observed followed by a decay which is similar to the long time behavior found in the upper two scans.

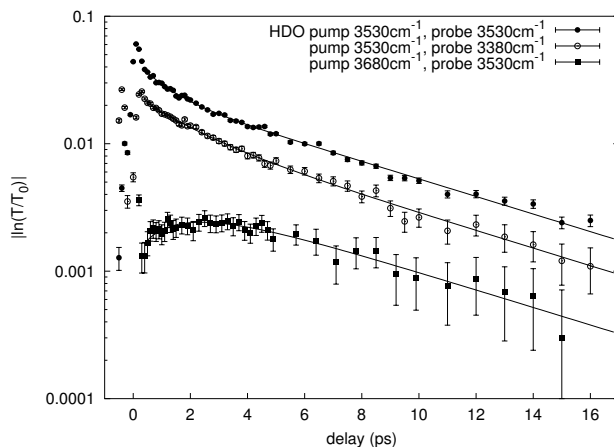


Figure 8.6. Delay time scans for HDO. Upper curve: pumping and probing the 0→1 band of the hydrogen bonded OH-group at 3530 cm^{-1} , middle curve idem now probing the 1→2 band (sign of curve inverted for clarity). The lower curve shows the response at 3530 cm^{-1} after excitation of the free OH-stretch mode at 3680 cm^{-1} . The scans are vertically scaled for clarity.

In Figures 8.7-9 delay time scans are shown for the embedded H_2O molecule. In Figure 8.7, the pump frequency is resonant with the free OH-group (3690 cm^{-1}), the probe frequencies are 3520 (ν_s and ν_b), 3610 (ν_{as}) and 3690 cm^{-1} (ν_f), respectively. We observe for H_2O an ingrowth of the bleaching at 3520 and 3610 cm^{-1} with a time constant of 1.3 ps followed by a slower decay with a time constant of 6.3 ps. The same decay behavior is observed for probing at 3690 cm^{-1} . Added to this slow relaxation behavior, is a fast decaying component for short delay times, which is similar to the rising time at the other two probe frequencies.

Figure 8.8 shows the delay times scans for pumping the antisymmetric stretch band at 3610 cm^{-1} . The upper scan shows the relaxation behavior at 3610 cm^{-1} , where a fast decay of ~ 200 fs is observed, followed by a slower decay of the bleaching with 6.3 ps. Tuning the probe to 3520 cm^{-1} leads to an ingrowth of the bleaching for short and a slow decay for long delay times. The ingrowth happens on the same ~ 200 fs observed at 3610 cm^{-1} . The induced absorption signal is displayed in the

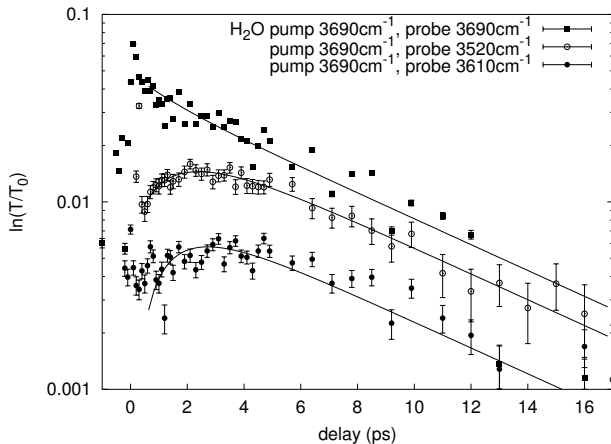


Figure 8.7. Delay time scans for H₂O. Upper curve: pumping and probing the 0→1 band of the free OH-group at 3690 cm⁻¹, middle and lower curve idem probing at 3520 and 3610 cm⁻¹, respectively. The scans are vertically scaled for clarity.

third curve of Figure 8.8. Two time scales govern the dynamics: a fast relaxation together with the slow time scale, observed for all frequencies. Figure 8.9, finally, shows the delay time scans for pumping at 3520 cm⁻¹. Probing at 3520 cm⁻¹ gives a fast decay for short delay times (1.3 ± 0.4 ps) together with the slower relaxation time of 6.3 ± 0.5 ps. Probing at 3610 cm⁻¹ shows a similar behavior, as does the 1→2 transition at 3350 cm⁻¹. Probing at 3680 cm⁻¹ shows a mono-exponential behavior with a time constant of 6.3 ps.

8.4.3 Orientational dynamics

As shown in Section 3.2, the rotational anisotropy can be calculated by measuring the signal with polarization parallel, $\ln(T/T_0)_{\parallel}$, and perpendicular, $\ln(T/T_0)_{\perp}$, to the pump pulse. The rotation free signal, i.e. the same signal as is observed in a magic angle measurement (see sections 8.4.1 and 8.4.2), is given by $\ln(T/T_0)_{\parallel} + 2\ln(T/T_0)_{\perp}$. Typical examples of $\ln(T/T_0)_{\parallel}$ and $\ln(T/T_0)_{\perp}$ are displayed in Figure 8.10.

Figure 8.11 shows the anisotropy decay curves. The probe frequencies lie for all decays in the 1→2 band at 3314 cm⁻¹, i.e. the singly hydrogen-bonded OH-group is mainly probed. In Figure 8.11a, the anisotropy decay for HDO is displayed. A mono-exponential decay is observed starting from 0.4. Figure 8.9b,c show the decay for H₂O, pumped at 3520 and 3610 cm⁻¹, respectively. In Figure 8.11b, the anisotropy

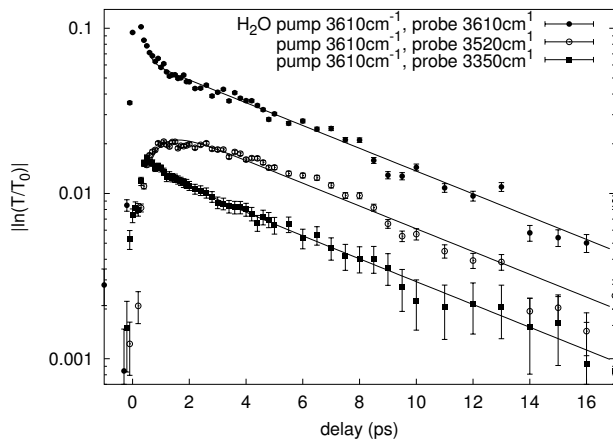


Figure 8.8. Delay time scans for H₂O: pumping the antisymmetric stretch mode at 3610 cm⁻¹, probe frequencies are from top to bottom: 3610, 3520, 3350 and 3690 cm⁻¹, respectively. Again, the scans are scaled vertically for clarity

decays from 0.4 to 0 in a bi-exponential manner. The observed decay for pumping the antisymmetric stretch mode (Fig. 8.11c), shows an instantaneous decay from 0.4 to 0.1 followed by a slower mono-exponential decay.

8.5 Hydrogen bond mediated energy transfer

8.5.1 The HDO molecule

The interpretation of the transient spectra of the water-acetone complex would not be possible without by the HDO-spectra. It is for this molecule that only two kinds of OH-groups are present: hydrogen-bonded and non-hydrogen-bonded. Let's therefore first have a look at the results obtained for HDO.

We attribute the fast component observed for short delay times in Figure 8.6 to the breaking and formation of a hydrogen-bond. Therefore, a fast decay is observed when pumping and probing the hydrogen-bonded OH-groups: bond breaking forms an extra relaxation channel. Pumping the free groups and probing the hydrogen-bonded groups leads to an increase of the bleaching, i.e. the amount of excited hydrogen-bonded OH-groups increases (see Figures 8.4b and 8.6). A bi-exponential fit of these data leads to a lifetime of the OH-stretch vibration T_1 of 6.3 ± 0.5 ps for both the free as the hydrogen-bonded OH-groups, the hydrogen bond breaking and making time,

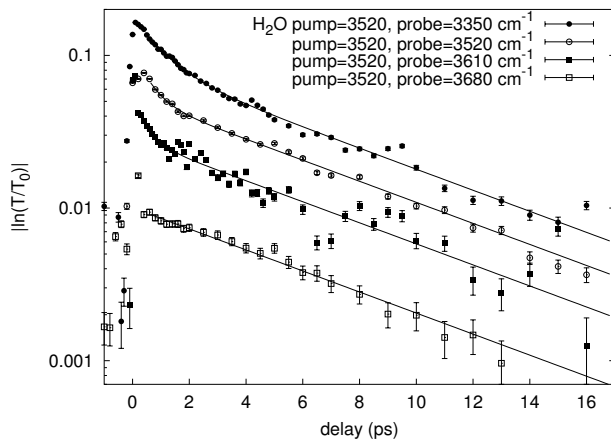


Figure 8.9. Delay time scans for H₂O: pumping the symmetric and hydrogen bond stretch mode at 3520 cm⁻¹, probe frequencies are from top to bottom: 3520, 3610, 3690 and 3350 cm⁻¹, respectively. The scans are vertically scaled for clarity.

τ_{hb} is found to be 1.3 ± 0.4 ps, as shown in the previous section.

The anisotropy decay for the HDO molecule (Figure 8.11a) can be well fitted with a single exponential. This gives a reorientation time of 6.0 ± 1.0 ps. The excitation of the hydrogen-bonded OH-stretch oscillators gives rise to an anisotropy in the sample. We attribute this time to the reorientation of the molecule in the liquid. It should be noted that hydrogen-bond breaking dynamics, as observed in the vibrational relaxation experiments, lead to a shift of the absorption frequency from ν_b to ν_f . Hence, it will not lead to a decay of the induced anisotropy, because the breakage of the bond does not induce a change in the polarization in the probe window.

The orientational relaxation time of water monomers was found [26] to range from 1.7 ps in solvents like carbon tetrachloride up to 6 ps in solvents with a large dipole moment, like acetonitrile. In view of this, it is not surprising that we find a reorientation time of 6 ps, as the dipole moments of acetonitrile and acetone are comparable.

8.5.2 H₂O: the intermediate state

The results for H₂O can be explained using the model depicted in Figure 8.12. In this model two processes are described: the formation and breakage of hydrogen bonds and the transfer of excitation energy between the two OH-groups in water. This gives

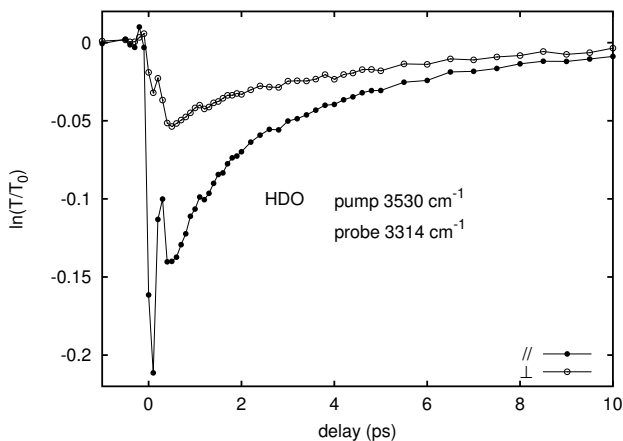


Figure 8.10. Pump-probe scans for HDO sample. The signal measured with polarizations parallel and perpendicular to the pump polarization are indicated by closed and open circles, respectively. From these two contributions, the anisotropy is calculated.

four different initial states in which an excited OH-group can be. These states are denoted with Roman numbers I, II, III and IV.

The direct transfer of excitation between the OH-stretches is very unfavorable due to the almost perpendicular dipole moments of both vibrations. Therefore, an intermediate or transient state is needed in which the energy is delocalized. Secondly, most water molecules prefer to have one hydrogen-bond. Breakage of this bond is very unfavorable unless the molecule gets in an (intermediate) state with two hydrogen-bonds. In this case, it would be preferable to break one hydrogen bond. Both conditions are fulfilled in the situation where the water molecule has two hydrogen-bonds. Therefore, we identify the situation in which a symmetric and antisymmetric mode exist as an intermediate state, which is necessary for the hydrogen-bond dynamics. This state is denoted by T in Figure 8.12.

Starting from situation I in Figure 8.12, a hydrogen-bond is present between the excited OH-stretch oscillator and the acetone molecule. We can end up in four different situations. In situation I and II, the excitation stays on the OH-group which was initially excited, whereas in situation III and IV the excitation is transferred to the other OH-group. Furthermore, in situation I and III the hydrogen bond is not broken, whereas in situation II and IV the hydrogen-bond is broken and formed at the other OH-group. Transitions between these states all involve the intermediate state T . Both the vibrational and the orientational dynamics measurements for H_2O can

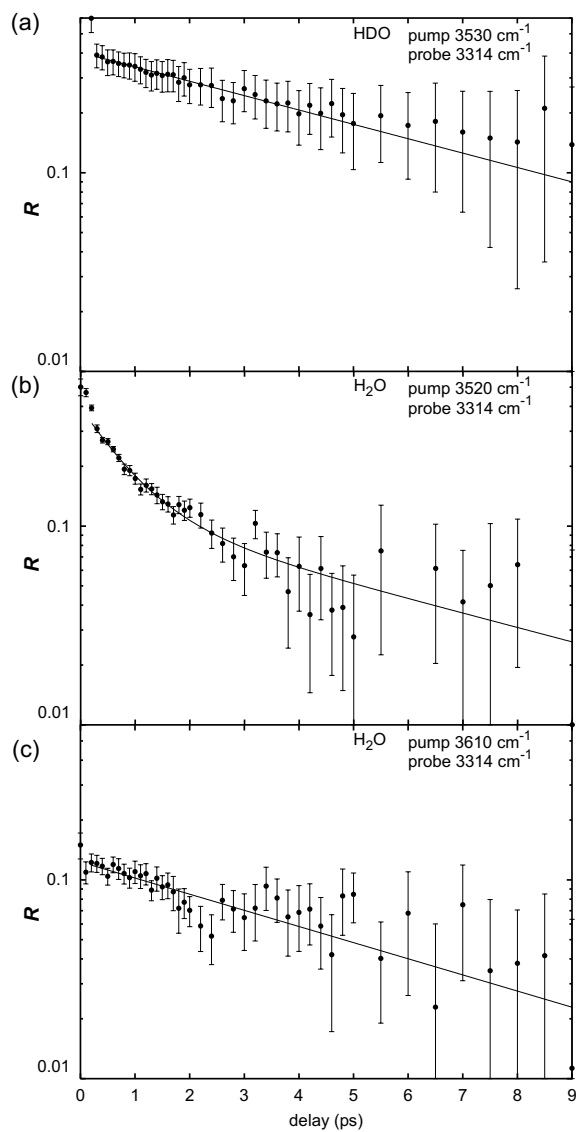


Figure 8.11. The measured anisotropy R as a function of delay for (a) HDO pumped at 3530 cm^{-1} , (b) H_2O pumped at 3610 cm^{-1} and (c) H_2O pumped at 3520 cm^{-1} . The probe frequency lies in the $1 \rightarrow 2$ band.

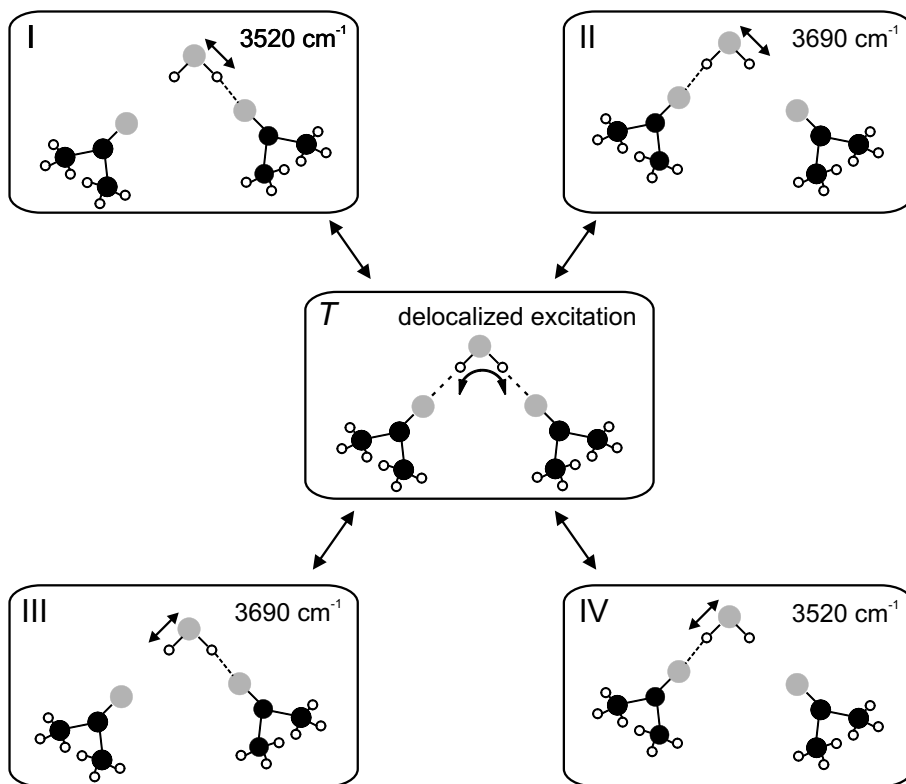


Figure 8.12. The state in which the excitation energy is delocalized forms the intermediate state for the two processes observed in the measurements: the transfer of excitation energy from one OH-group to the other and the changes in excitation frequency due to hydrogen-bond dynamics.

be explained by the model presented in Figure 8.12. In the process I→II, for example, the excitation stays on the initially excited OH-groups, but a hydrogen bond is broken and formed at the other group. This process contributes to the rotation free signal, but not to the anisotropy decay.

8.5.3 H₂O: interpretation of the measurements

In analogy with HDO, we attribute the ingrowth observed for H₂O when pumping at 3690 cm⁻¹ and probing at 3520 and 3610 cm⁻¹ to the formation of a hydrogen-

bond, as shown in Figure 8.7 (process II/III \rightarrow T \rightarrow I/IV). When the pump and probe frequencies are equal, hydrogen-bond breaking and making forms an extra and faster relaxation channel and will therefore appear as a peak on the bleaching signal (see Fig 8.7 upper curve and 8.9 second curve). The observed signals for pump and probe frequencies at 3610 cm⁻¹ need special attention. It should be noted that the anti-symmetric stretch forms the transient *T* state. Therefore, the ingrowth observed at 3520 cm⁻¹ (middle curve of Fig. 8.8) is the result of breaking of one hydrogen bond and strengthening of the other. As stated before, the fast time scales observed for Figure 8.8 upper two curves, are similar; they are, however, much faster than the hydrogen bond breaking and making time which is in the order of 1 ps. This fast decay and fast ingrowth occurs on a \sim 200 fs time scale. This fast time scale can be well understood using the model from Figure 8.12. The transition state is an energetically unfavorable state, therefore breakage of one of the hydrogen bonds out of this state occurs faster than in case the initial state was one of the four stable states.

The small absorption band at 3180 cm⁻¹ observed for H₂O is due to a combination band from the transition $\nu_b=0, \nu_f=1 \rightarrow \nu_b=2, \nu_f=0$. The calculated energy for this transition is (3520 + 3350) - 3690 = 3180 cm⁻¹, which matches with the observed absorption feature. The dynamics of the band is similar to that of the 1 \rightarrow 2 transition, which corroborates our assignment. Because we observe this band at all three pump frequencies, this implies that at all three pump frequencies excited free OH-stretches are present, either due to energy transfer (Figure 8.5a) or due to direct excitation with (the wings of) the pump pulse (Figure 8.5b,c).

For the H₂O molecule, the observed anisotropy decay is more complicated. By pumping at 3520 cm⁻¹ in the H₂O sample, mainly singly hydrogen-bonded OH-stretches are excited. In contrast to the HDO molecule, breakage of a hydrogen-bond now affects the anisotropy. Passing the transient state *T*, the excitation can end up in four different states. Because there is no preferred state, the excitation energy will be equally distributed over both OH-groups. Therefore, breakage of the hydrogen-bond leads to a decay of the anisotropy with τ_{hb} . The data can be fitted with a bi-exponential function with time scales of 1.0 \pm 0.4 ps and 6.0 \pm 1.0 ps. We attribute the faster component to hydrogen-bond breaking dynamics, the slower decay component is the reorientation time of the molecule as observed for HDO.

Direct excitation of the transient state leads to an instantaneous decay of the anisotropy from 0.4 to approximately 0.1. This means that the energy redistribution among both OH-groups, and thus the delocalization of the excitation, occurs on an ultrafast time scale. It can be shown that the rotational anisotropy decays from $\frac{2}{5}$ to $\frac{2}{5} * P_2(\cos\delta)$, with P_2 the second-order Legendre polynomial, if the total excitation polarization is transferred from a donor molecule to an acceptor molecule that has its transition dipole under an angle δ with respect to the donor dipole [26, 94]. Because the angle between both OH-groups is 104 degrees, delocalization of the excitation leads to a decrease of the anisotropy to $\frac{1}{2} * (\frac{2}{5} + \frac{2}{5} * P_2(\cos(104^\circ))) = 0.12$, as is indeed observed for short time scales. It should be noted that also in Figure 8.11b a first

decay of the anisotropy to the value of 0.12 is observed. Because here, the initial situation was state I or IV instead of the intermediate T , the time scale at which this level is reached is different.

Transfer mechanisms between two resonances influence the observed population dynamics. When the transfer time is slow compared to the lifetime, the individual lifetimes of the separate states are not affected. In this case, we would have different lifetimes for the hydrogen-bonded, the free, the symmetric and the antisymmetric OH-stretch. We observe, however, similar dynamics at all probe frequencies. This means that the transfer times between two resonances are faster than the lifetime, and that the lifetime decays with an average value. In fact, all observed transfer times, either the hydrogen-bond dynamics (1.3 ps) or the bond breakage time out of the transient state (200 fs), are faster than the lifetime. All measured delay time scans for H_2O can be well fitted with a bi-exponential decay. The longer time component, the lifetime of the OH-stretch vibration is observed to be 6.3 ± 0.4 ps, the slower time depends on the initial state. When starting from situation I-IV the hydrogen-bond dynamics time is 1.3 ± 0.5 ps.

8.6 Conclusions

We have studied both vibrational and rotational relaxation of a single water molecule with hydrogen bonds. Using a solution of water, acetone and carbon tetrachloride, we have shown that for HDO two different OH-stretch vibrations are present: those of free OH-groups (ν_f , 3680 cm^{-1}) and those of hydrogen-bonded OH-groups (ν_b , 3530 cm^{-1}). For H_2O instead of HDO, two OH-stretch vibrations come into play. A water molecule which donates two hydrogen bonds, has two OH-stretch vibrations: the symmetric (ν_s) and the antisymmetric (ν_a) mode, which absorb at 3520 and 3610 cm^{-1} , respectively. We have shown that the state in which the H_2O molecule has two hydrogen bonds acts as an intermediate state for excitation transfer and hydrogen-bond dynamics. From the vibrational relaxation experiments we observe that in H_2O three time scales are present. Next to the life time of the OH-stretch vibration, which is found to be 6.3 ± 0.5 ps for all types, two other time scales are found. Hydrogen bond breaking and making is observed to occur on a 1.3 ± 0.4 ps ps time scale starting from one of the states I-IV. Starting from the intermediate state a characteristic time of 0.2 ps is found for ending up in one of the four states I-IV. From the rotational anisotropy measurements we conclude that molecular reorientation has a characteristic time scale of 6.0 ± 1.0 ps. Pumping the intermediate state gives an instantaneous decrease of the anisotropy from 0.4 to 0.12, the signature of a state in which the energy is delocalized, followed by the molecular reorientation with 6 ps.

9 Vibrational Relaxation and Coupling of Two OH-stretch Oscillators with an Intramolecular Hydrogen-Bond

We studied the vibrational dynamics of the OH-stretch oscillators of an alcohol with two vicinal OH-groups using femtosecond mid-infrared pump-probe spectroscopy. The absorption spectrum of pinacol (2,3-dimethyl-2,3-butanediol) in CDCl_3 shows two OH-stretch peaks belonging to hydrogen bonded and free OH-groups. The anharmonicities of the hydrogen-bonded and free OH-stretch vibrations are 180 and 160 cm^{-1} , respectively. The lifetime T_1 of the OH-stretch vibration is found to be 3.5 ± 0.4 ps for the hydrogen-bonded and 7.4 ± 0.5 ps for the free OH-group. We observed sidebands in the transient spectra after excitation of the bonded OH-group, which we attribute to a progression in the low-frequency hydrogen-bond stretch mode. The sideband is red-shifted 60 cm^{-1} with respect to the $0_g \rightarrow 1$ transition. Due to the coupling between the two OH-groups and the presence of the sidebands, simultaneous excitation of both OH-stretch vibrations leads to oscillations on the pump-probe signal with frequencies of 40 and 60 cm^{-1} .

9.1 Introduction: The OH-stretch vibration as an indicator for the structure of molecules

The structure of molecules plays an essential role in chemical reactivity. A clear example are proteins for which the 3D conformation determines the selectivity and specificity of the biochemical reactions. As a result, the study of the relation between the function and the structure of molecules has become a major research theme. A relatively new technique for unraveling the structure and conformational changes of biomolecules is 2D vibrational spectroscopy. Up to now, this technique has predominantly been applied to the peptide amide I band [29, 30, 31, 73, 109, 110], which mainly involves the C=O stretch vibration. This band lies around 1650 cm^{-1} , depending on the precise structure. The orientation and distance of two different amide I vibrations within a peptide determines the strength of the coupling between the vibrations, and hence a measurement of the coupling may help to determine the conformation.

The potential of 2D vibrational spectroscopy could be greatly enhanced if other vibrations could also be used for probing the molecular conformational dynamics. Recently, Hochstrasser and coworkers have explored this field using an extra color to probe the amide-A band (N-H stretch, $\sim 3300\text{ cm}^{-1}$) next to the amide-I band [79, 80]. Another interesting candidate would be the O-H stretch vibration which can be found in many molecules. Furthermore, this vibration is strongly anharmonic and very sensitive to its environment, in particular to hydrogen bonding, as shown in Chapter 1. As a first step, in this Chapter we will focus on the interaction between two OH-groups within one molecule. Clearly, the simplest example would be pure water (H_2O). However, the strong intermolecular interactions in pure water prevents a careful study of the vibrational energy relaxation and transport [52], see Chapter 4. We therefore studied a di-alcohol which forms an intramolecular hydrogen bond, dissolved in an apolar solvent. Most studies on alcohols with two OH-groups have dealt with the linear absorption spectrum [44, 57, 71, 72, 86, 87], the determination of the structure, and the effect of (slow) interchanges between different conformers. Unfortunately, di-alcohols with a single carbon-chain, like 1,2-ethanediol, or 1,2-propanediol dissolved in an apolar solvent like CCl_4 tend to form clusters already at rather low concentrations. Hence, we used a di-alcohol for which the polar OH-groups were shielded from the surroundings due to the presence of side groups. Here, we present results on 2,3-dimethyl-2,3-butanediol or pinacol.

Pinacol can have many conformations that can be divided into two classes with respect to the central C-C axis: the gauche conformers, where the neighboring OH-groups form an internal hydrogen bond, and the trans conformers, without a hydrogen bond. The gauche form is energetically more favorable, but depending on the solvent, the trans form may also be present in solution [10]. The two OH-groups in the trans form are equivalent and will give rise to a single peak in the absorption spectrum. In the gauche form, however, one OH-group acts as a hydrogen bond donor and the other as a hydrogen bond acceptor. The latter OH-group behaves very similar to the non-

bonded OH-groups of the trans conformer. In the following we will denote the non-bonded OH-groups of the trans and the hydrogen bond accepting OH-group of the gauche conformer as "free" OH-groups. The presence of OH-groups which donate or accept a hydrogen-bond will lead to a splitting of the OH-stretch band [44]. Here, we study the ultrafast dynamics of the OH-groups and their coupling using femtosecond mid-infrared pump-probe spectroscopy.

9.2 Experimental

9.2.1 Narrow band excitation

In the experiment, one of the OH-stretch vibrations of pinacol is excited to the $\nu_{\text{OH}} = 1$ state with an intense femtosecond mid-infrared pulse. The effect of the excitation on both OH-groups is measured by following the transmission change of a probe pulse as a function of delay with respect to the pump. This excitation leads to a transient bleaching of the $0 \rightarrow 1$ transition (positive signal) due to absorption from the ground state and stimulated emission from the excited state and to an induced absorption of the $1 \rightarrow 2$ transition (negative signal).

The generation of mid-infrared laser pulses and the probe setup are described in Chapter 3.2. In this study, however, we use two KTP-crystals to generate the pump pulses. With the second crystal, the spectral band width of the pump pulses can be reduced to approximately 50 cm^{-1} . The pump pulses have a duration of about 500 fs and an energy of about $20 \mu\text{J}$.

9.2.2 Signal detection

After the sample, the transmitted probe beam is focused by a 50 mm CaF_2 lens on the entrance slit of an imaging spectrograph. In this study, the array covers a spectral width of 200 cm^{-1} at a frequency of 3300 cm^{-1} . The reference beam is not dispersed, in contrast to the previous chapter. We instead use a single nitrogen-cooled MCT (HgCdTe)-detector to measure the reference intensity I_{ref} . The transmission change $\ln(T/T_0)$ is calculated as a function of delay between pump and probe pulse, where $T(\omega) = I(\omega)/I_{\text{ref}}$ and $T_0(\omega) = I_0(\omega)/I_{\text{ref}}$. The probe polarization was set at the magic angle with respect to the polarization of the pump pulse by means of a zero-order $\lambda/2$ plate to cancel the effect of orientational relaxation on the observed dynamics [24]. Whereas the time-integrated pump-probe signal is given by Eq. 2.46, the dispersed pump-probe signal $I(\omega, \Delta t)$ reads [92]:

$$I(\omega, \Delta t) = 2\omega_2 \text{Im} E_2(\omega) P^{(3)*}(\omega, \Delta t) \quad (9.1)$$

where $E_2(\omega)$ and $P^{(3)}(\omega)$ are the Fourier transforms of the probe field and third order polarization.

9.2.3 Broadband excitation

The experiment described in Section 9.3.5 is performed using a similar setup. A commercial diode-pumped Ti:Sapphire amplifier delivers 800 nm pulses with a duration of about 100 fs, an energy of 1 mJ per pulse, and a repetition rate of 1 kHz. These pulses are used in a commercial white-light seeded OPA system based on BBO. Signal and idler pulses are generated with a wavelength of 2240 and 1245 nm, respectively. The idler is frequency doubled by a second BBO crystal. Finally, light at 2790 nm (3590 cm^{-1}) is generated in a DFG process by combining the doubled idler with the 800 nm light in a KTP crystal. The resulting pulses have an energy of $5\text{ }\mu\text{J}$ and a FWHM of 110 cm^{-1} . A probe beam is split off from this beam by means of a wedged CaF_2 window and is delayed by means of a delay line. Both beams are focused into the sample using an off-axis parabolic mirror with a focal length of 101.6 mm. The detection system is the same as used in the narrow-band excitation experiments.

9.2.4 Sample

The sample was prepared by dissolving pinacol (2,3-dimethyl-2,3-butanediol) crystals (Aldrich, 98%) in chloroform-d (CDCl_3 , Aldrich, 99.6 atom % D). The concentration used was 0.21 mol/l. The measurements were performed on a $500\text{ }\mu\text{m}$ thick sample kept in between two CaF_2 windows. The transmission of the sample is typically 15% at 3615 cm^{-1} . In order to avoid the accumulation of heat produced by the pump pulses, the sample is rotated.

9.3 Results

9.3.1 Absorption spectrum

The absorption spectrum in the OH-stretch region of pinacol molecules dissolved in chloroform-d is depicted in Figure 9.1 for different concentrations. For low concentrations (lower two curves), two separate peaks are observed at 3570 cm^{-1} and 3612 cm^{-1} . These peaks correspond to the internally hydrogen bonded OH-stretch and the free OH-stretch vibration, respectively [10, 11]. At higher concentrations, a red-shifted band shows up. We attribute this band to clusters of pinacol molecules formed in the solution, in close analogy with the behavior of alcohols dissolved in non-polar solvent [107, 48]. Furthermore, a small band at 3670 cm^{-1} is observed. Inspection of the normal modes of both chloroform-d [85] and pinacol [10] shows that neither pinacol nor the solvent can have a combination band at 3670 cm^{-1} . A pump-probe measurement performed on this band showed a slow decay of the bleaching with a time constant of about 60 ps (result not shown). This time constant agrees very well with the one observed by Graener et al. [23] for monomeric water molecules dissolved in chloroform-d. We therefore conclude that our pinacol sample contains a small amount of water monomers. Because this band lies outside the spectral region

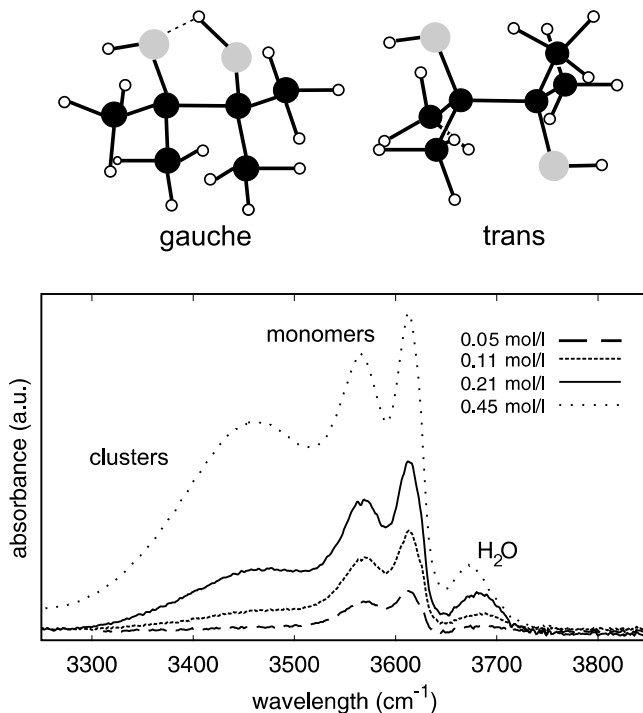


Figure 9.1. Pinacol can adopt two conformations with respect to the central C-C axis. On the left side the gauche conformer is shown, in which an internal hydrogen bond is formed between the two OH-groups. This hydrogen bond is absent in the trans conformer (drawn structures adapted from Ref. [10]). Lower part: the absorption spectrum of pinacol molecules dissolved in CDCl_3 for different concentrations. In this work, we used the 0.21 mol/l sample (solid line).

of the pinacol OH-stretch vibrations, it does not affect the study of the OH-bands of pinacol. The experiments described in this study are all performed using the 0.21 mol/l sample (solid line).

9.3.2 Transient spectra

Figure 9.2 shows three transient spectra obtained after excitation at 3615 cm^{-1} . At this frequency both the OH-groups of the trans molecules and the hydrogen bond accepting OH-group of the gauche molecules are excited. One clearly sees a bleaching around the pumping frequency in all three spectra. In addition, a small shoulder

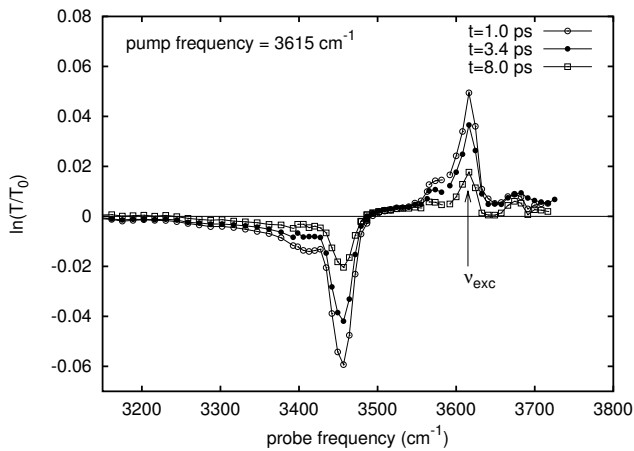


Figure 9.2. The transmission change as a function of probe frequency for different delay times after pumping at 3615 cm^{-1} .

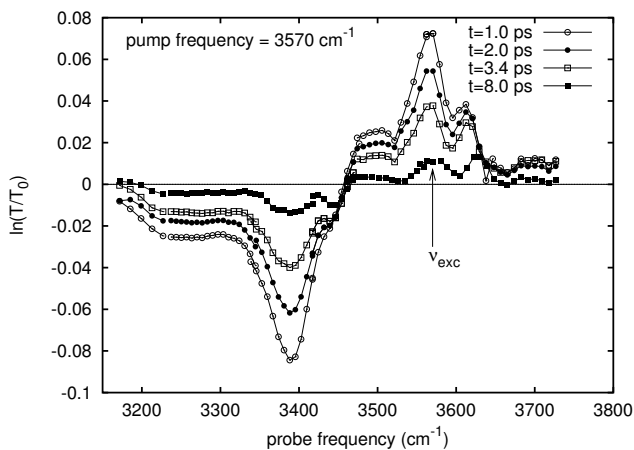


Figure 9.3. Transient spectra after pumping the hydrogen-bonded OH-group (3570 cm^{-1}) for four different delay times.

around 3570 cm^{-1} is observed. The 1 \rightarrow 2 absorption is observed near 3450 cm^{-1} , which implies that the anharmonicity is 160 cm^{-1} . Around 3400 cm^{-1} a small shoulder is observed. In Figure 9.3, four transient spectra are shown obtained after pumping of the hydrogen bonded OH-group of the gauche conformer at 3570 cm^{-1} . This excitation leads to a bleaching around 3570 cm^{-1} and to a smaller bleaching at 3510 cm^{-1} . In addition a bleaching around 3610 cm^{-1} is observed, the frequency at which the free OH-groups absorb. This 3610 cm^{-1} bleaching clearly decays slower than the bleachings at 3570 and 3510 cm^{-1} . At 3390 cm^{-1} , the 1 \rightarrow 2 absorption of the hydrogen-bonded OH-group is observed, which implies that this vibration has an anharmonicity of 180 cm^{-1} . We also observe induced absorption at frequencies lower than 3300 cm^{-1} .

9.3.3 Delay time scans

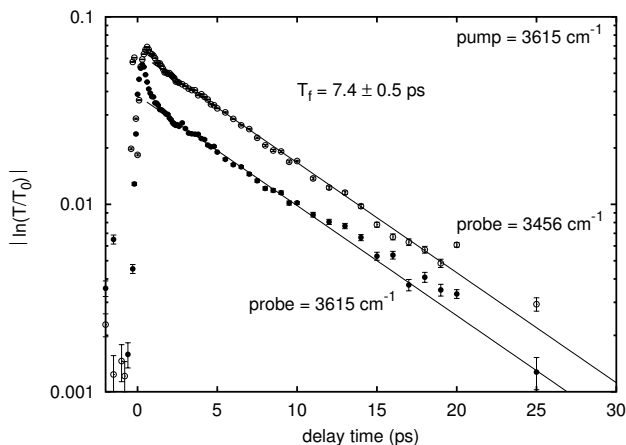


Figure 9.4. Transmission change as a function of delay time between pump and probe pulse. The pump pulse was fixed at 3615 cm^{-1} , the probe at 3456 (upper curve) and 3615 cm^{-1} (lower curve). The sign of the upper signal (induced absorption) was inverted.

Figure 9.4 shows two time traces measured at the center of the bleaching (3615 cm^{-1} , lower curve) and induced absorption (3456 cm^{-1} , upper curve) signals after excitation of the free OH-group at 3615 cm^{-1} . Both curves show the same mono-exponential dynamics. In the lower curve a strong modulation of the signal around $t = 0$ is observed due to a combination of a coherent artifact [105] and the Kerr effect [13]. The latter effect amounts to a small shift in the spectrum of the probe pulse due to the simultaneous presence of the intense pump pulse. The pump

field slightly changes the index of refraction of the solvent and the CaF_2 windows, causing a frequency shift of the probe pulse. For delays $t < 0$ (probe earlier than pump) the result is a red shift, for delays $t > 0$ the result is a blue shift. Since the effect is non-resonant, it only occurs for delay values within the cross-correlation.

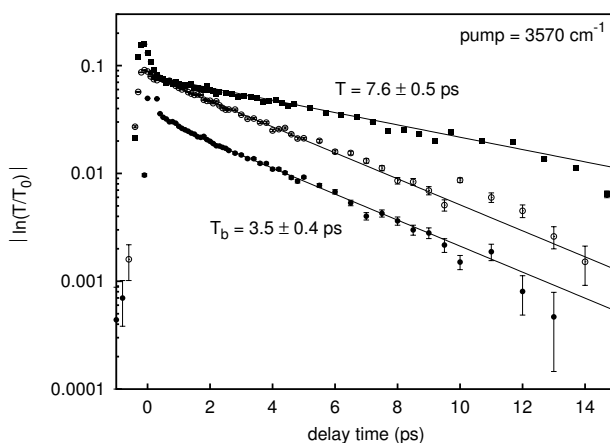


Figure 9.5. Delay time scans for three different probe frequencies (3617, 3575 and 3388 cm^{-1} , upper to lower curve) after pumping the hydrogen bonded OH-group (3570 cm^{-1}). The sign of the lower curve was inverted for clarity.

Figure 9.5 presents the transmission changes at three different wavelengths after pumping at 3570 cm^{-1} : probing the free OH-stretch band (3617 cm^{-1} , upper curve), and probing at the center of the $0 \rightarrow 1$ bleach (3575 cm^{-1} middle curve) and $1 \rightarrow 2$ induced absorption (3388 cm^{-1} , lower curve), respectively. At 3575 and 3388 cm^{-1} the same dynamics are observed. At 3617 cm^{-1} the decay is much slower. In Figure 9.6, delay time scans at three other probe frequencies are displayed, obtained with an excitation pulse at 3570 cm^{-1} .

It follows from Figures 9.4-6 that the decay of the bleaching and induced absorption can be fitted well with a single exponential. All fits started after 1 ps, to exclude coherent artifacts and cross phase modulations. For the lifetime of the free OH-group we find $T_f = 7.4 \pm 0.5$ ps (Figure 9.4), for that of the bonded OH-group we find $T_b = 3.5 \pm 0.4$ ps (Figure 9.5, lower two curves). The three curves in Figure 9.6 can also be well described with a single exponential. The observed lifetime here is 3.2 ± 0.5 ps.

The question now arises whether energy transfer is possible between the bonded and the free OH-group. A fast energy transfer process would lead to an identical

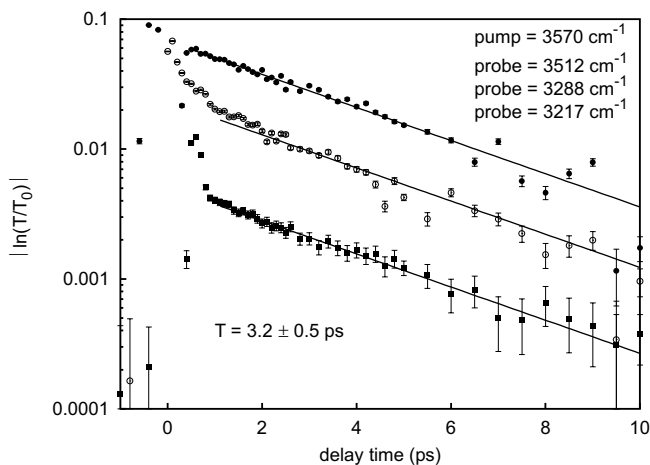


Figure 9.6. Delay time scan for pumping the bonded OH-group at 3570 cm^{-1} and probing at three different frequencies in the sidebands. The sign of the induced absorption signals (lower two curves) was inverted.

relaxation time for all probe frequencies, which is in contrast with our observations. If the energy transfer rate would be comparable with the vibrational relaxation rate, a biexponential behavior is expected. The pumped (donor) transition would show an initial faster decay due to energy transfer, whereas the acceptor transition would show an initial ingrowth of the signal. This is not observed either. We therefore conclude that energy transfer between the hydrogen-bonded and free OH-groups is much slower than the vibrational relaxation rate. The signal observed at 3617 cm^{-1} in Figure 9.5 results from direct excitation by the wing of the pump pulse.

9.3.4 The sidebands

The observed bleaching and induced absorption at the red side of the main $0\rightarrow 1$ and $1\rightarrow 2$ transitions in Fig. 9.3 show the same dynamics as the main absorption and bleaching peaks. This indicates that these signals result from sidebands. It should be noted that these signals cannot be due to the response of pinacol clusters, since we found that the cluster OH-stretch vibrations have a lifetime of 2 ps (results not shown).

As indicated in Figure 9.7, the anharmonic coupling between a low-frequency mode (n) and the high frequency OH-stretch mode (ν) will give rise to bleaching and absorption contributions at wavelengths other than the main $0\rightarrow 1$ and $1\rightarrow 2$

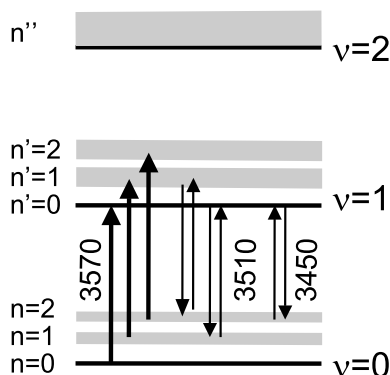


Figure 9.7. Energy level scheme of the hydrogen bonded OH-group used for the explanation of the appearance of sidebands. The $\nu=0,1,2$ states represent the vibrational ground state and the first two excited states of the OH-stretch vibration. The anharmonically coupled low frequency mode is indicated by n and n' in the ground and first excited state of the OH-stretch vibration, respectively. The arrows correspond to the observed sideband transitions.

transitions. Excitation from the ground state ($\nu=0$) to the excited state ($\nu=1$), leads to progression in the bleaching ($\nu=0, n=i \rightarrow \nu=1, n'=\dots, i-1, i, i+1, \dots$), the stimulated emission ($\nu=1, n'=i \rightarrow \nu=0, n=\dots, i-1, i, i+1, \dots$), and the induced absorption ($\nu=1, n'=i \rightarrow \nu=2, n''=\dots, i-1, i, i+1, \dots$)

In Figure 9.3, one observes the first sideband in bleaching at 3510 cm^{-1} , the low-frequency mode observed has thus a frequency of 60 cm^{-1} . Also for the $1 \rightarrow 2$ transition a broad sideband is observed. Probing at a frequency corresponding to the ($\nu=1, n'=i \rightarrow \nu=2, n''=\dots, i-2, i-1$) transition will lead to a red-shifted induced absorption, as observed in Fig. 9.3. Likely, as the result of the distribution of hydrogen bond frequencies and the fast dephasing of the OH-stretch vibration in the excited state, the sidebands overlap, leading to a broad featureless absorption. We do not observe a clear blue-shifted band in the transient spectra. This can be explained from the fact that the first, fast relaxing, sideband at 3630 cm^{-1} would be hidden under the slow relaxing band of the free OH-stretch band. In the linear spectrum (Fig. 9.1) the very small shoulder at the high-frequency side of the free OH-band could originate from the blue-shifted sideband.

Figure 9.8 shows an enlargement of the response near 3450 cm^{-1} , where the second sideband in the bleaching ($\nu=0, n=i \rightarrow \nu=1, n'=i-2$) is expected. At this frequency, both the sideband and the wing of the $1 \rightarrow 2$ absorption of the free OH-group are observed. These signals have opposite signs and different decay times (3.5 and 7.4 ps), which leads to the complicated dynamics observed in Figs. 9.8 and 9.9.

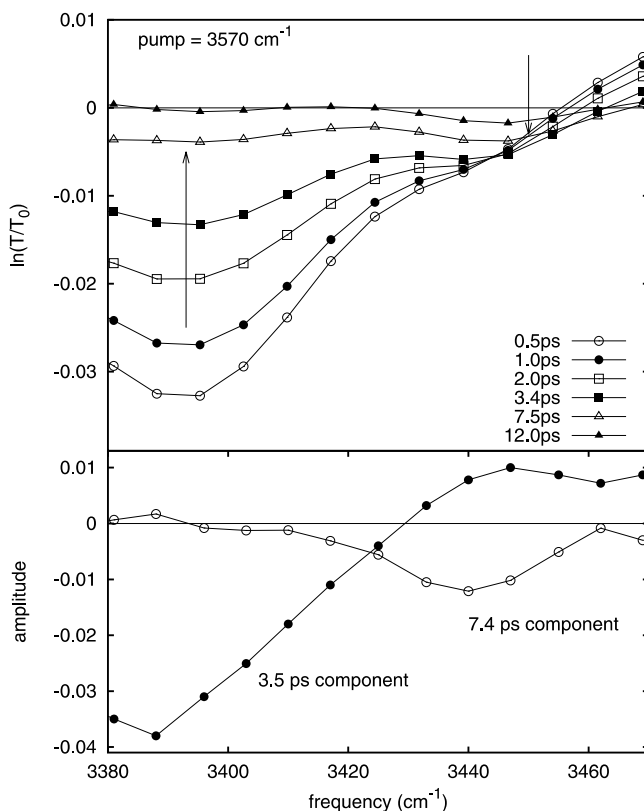


Figure 9.8. Upper part: transient spectrum for six different delay times after pumping at 3570 cm^{-1} , zoomed in to the 3450 cm^{-1} region. Lower part: contributions of the two relaxation times to the observed decay as a function of probe frequency.

Earlier reported sidebands of 35 cm^{-1} for 2,2-dimethyl-3-ethyl-3-pentanol dissolved in CCl_4 were attributed to the hydrogen bond bending mode [47, 48, 49]. Because we only observe sidebands for the hydrogen-bonded OH-group and not for the free OH-group, it is reasonable to attribute the low-frequency mode n to a hydrogen bond mode. Based on our results, we cannot distinguish whether the low frequency mode is the hydrogen bond stretch or bending mode.

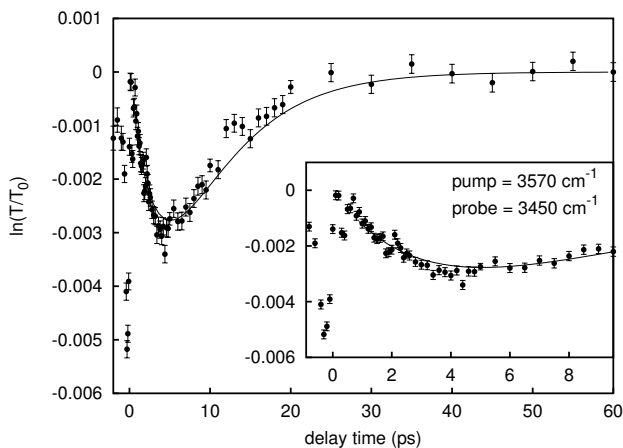


Figure 9.9. Delay time scan for pumping at 3570 cm^{-1} and probing at 3450 cm^{-1} . Inset: short time behavior.

9.3.5 Broadband excitation

In Fig. 9.10 the result of a one color pump-probe experiment is shown in which pump and probe pulses were used with a large spectral width (110 cm^{-1}). The center frequency of the pulse was 3590 cm^{-1} , in between both OH-stretch bands. The signal contains oscillations that correspond to frequencies of 40 cm^{-1} and 60 cm^{-1} . These oscillations are observed at all measured probe frequencies ($3495\text{--}3650\text{ cm}^{-1}$) albeit with different amplitudes. The 60 cm^{-1} frequency component corresponds to the interference of the main transition of the hydrogen-bonded OH group centered at 3570 cm^{-1} and its sideband centered at 3510 cm^{-1} . Although we cannot completely exclude that the 40 cm^{-1} oscillation is due to anharmonic coupling with another low-frequency mode, this is not very likely, because the 60 cm^{-1} hydrogen bond mode is the only low-frequency mode that is expected to be strongly coupled with the OH-stretch vibration. The 40 cm^{-1} frequency component most likely results from the interference of the free and the hydrogen-bonded OH group of the pinacol molecule. The observation of this interference in the pump-probe signal implies that these two oscillators are coupled, i.e. excitation of one of the oscillators leads to a frequency shift of the other. Hence, the 40 cm^{-1} frequency component must result from the gauche conformer of pinacol for which the free and hydrogen-bonded OH groups are indeed closely spaced.

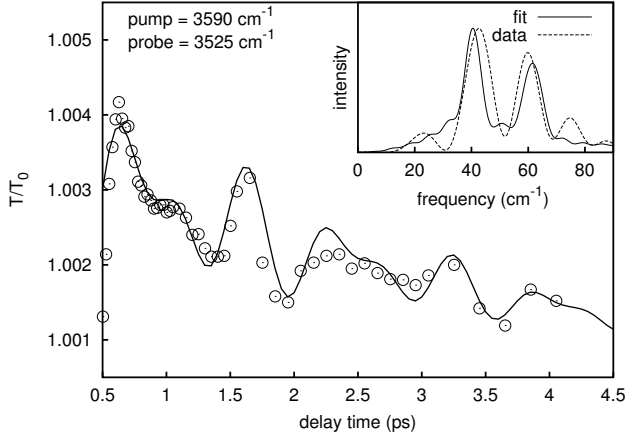


Figure 9.10. Delay time scan obtained after broadband excitation at 3590 cm^{-1} for a probe frequency of 3525 cm^{-1} . The solid curve is a fit using the model which takes into account the coupling between the free and hydrogen bonded OH–group, and between the hydrogen-bonded OH–group and its sideband. See section 9.4 for the calculation of this pump-probe signal. Inset: Fourier transforms of the observed oscillations in the data (dashed line) and the fit (solid line).

9.4 Coupling of two O–H oscillators

The solid curve in Fig. 9.10 represents a calculation of the pump-probe signal in which the anharmonic coupling and the presence of a sideband are taken into account. In this calculation the pump-probe signal is described in the following way. The spectrally resolved pump-probe signal is given by $S(\omega) \propto \text{Im}[E_2(\omega)P^{(3)}(\omega)]$, with $E_2(\omega)$ the Fourier transform of the probe field, and $P^{(3)}(\omega)$ the Fourier transform of the third-order polarization that is generated by the pump field $E_1(\mathbf{r}, t) = \mathcal{E}_1(t)e^{i(\mathbf{k}_1 \cdot \mathbf{r} - \omega_1 t)} + \text{c.c.}$ and the probe field $E_2(\mathbf{r}, t) = \mathcal{E}_2(t)e^{i(\mathbf{k}_2 \cdot \mathbf{r} - \omega_2 t)} + \text{c.c.}$ The Feynman diagrams representing the different contributions to the third-order polarization are shown in Figure 9.11. The diagrams R_1, R_2, R_3 represent the rephasing contributions, the diagrams R_4, R_5, R_6 the non-rephasing contributions.

The response functions that follow from these diagrams are [29, 30, 61]:

$$R_1 = \sum_{i,j} \mu_{0,i}^2 \mu_{0,j}^2 e^{i(\epsilon_i t_3 - \epsilon_j t_1)} e^{i(\epsilon_i - \epsilon_j) t_2} e^{-t_3/T_{2,i} - t_1/T_{2,j} - t_2/T_{1,ij}} \quad (9.2)$$

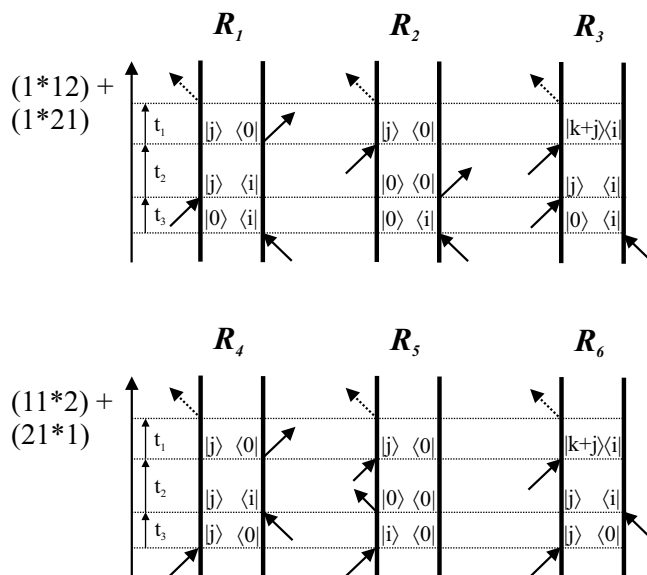


Figure 9.11. Feynman diagrams for the different contributions to the third-order polarization.

$$R_2 = \sum_{i,j} \mu_{0,i}^2 \mu_{0,j}^2 e^{i(\epsilon_i t_3 - \epsilon_j t_1)} e^{-t_3/T_2, i - t_1/T_2, j - t_2/T_1, ii} \quad (9.3)$$

$$R_3 = - \sum_{i,j,k} \mu_{0,i} \mu_{0,j} \mu_{j,j+k} \mu_{j+k,i} e^{i(\epsilon_i t_3 - (\epsilon_{k+j} - \epsilon_i) t_1)} e^{i(\epsilon_i - \epsilon_j) t_2} \times e^{-t_3/T_2, i - t_1/T_2, k+j, i - t_2/T_1, ij} \quad (9.4)$$

$$R_4 = \sum_{i,j} \mu_{0,i}^2 \mu_{0,j}^2 e^{-i\epsilon_j(t_3+t_1)} e^{i(\epsilon_i - \epsilon_j) t_2} e^{-t_3/T_2, j - t_1/T_2, j - t_2/T_1, ij} \quad (9.5)$$

$$R_5 = \sum_{i,j} \mu_{0,i}^2 \mu_{0,j}^2 e^{-i(\epsilon_i t_3 + \epsilon_j t_1)} e^{-t_3/T_2, i - t_1/T_2, j - t_2/T_1, ii} \quad (9.6)$$

$$R_6 = - \sum_{i,j,k} \mu_{0,i} \mu_{0,j} \mu_{j,j+k} \mu_{j+k,i} e^{-i(\epsilon_j t_3 + (\epsilon_{k+j} - \epsilon_i) t_1)} e^{i(\epsilon_i - \epsilon_j) t_2} \times e^{-t_3/T_2, j - t_1/T_2, k+j, i - t_2/T_1, ij} \quad (9.7)$$

In the above equations i, j, k represent states of different oscillators, ϵ_i the energy of state i and $\mu_{i,j}$ the transition dipole moment. In these response functions it is assumed that transitions $|i\rangle \rightarrow |k+j\rangle$ can be neglected if $i \neq j$ and $i \neq k$. Hence, $\mu_{j,k+i} = 0$, for $j \neq k$ and $i \neq k$. Furthermore, it is assumed that $T_{2,i} = T_{2,i+j,j}$, which implies that, if $i = j$, the $0 \rightarrow 1$ and the $1 \rightarrow 2$ transitions of resonance i are assumed to show the same homogeneous dephasing time and, in case $i \neq j$, excitation of j does not affect the homogeneous dephasing of i . The time constant $T_{1,ij}$ represents the population relaxation time of resonance i , in case $i = j$. If $i \neq j$, $T_{1,ij}$ represents the dephasing time of the mixed excitation of resonances i and j , i.e. of the state $|j\rangle\langle i|$.

If the dipole moments of the allowed transitions are $\mu_{i,i+j} = \mu_{0,j}$, $i \neq j$, and $\mu_{i,i+j} = \sqrt{2}\mu_{0,i}$, $i = j$, the rephasing response functions can be grouped together:

$$\sum_{l=1}^3 R_l = \sum_{i,j} \mu_{0,i}^2 \mu_{0,j}^2 e^{i(\epsilon_i t_3 - \epsilon_j t_1)} [e^{-t_2/T_{1,ii}} + e^{i(\epsilon_i - \epsilon_j)t_2} \times e^{-t_2/T_{1,ij}}] [1 - e^{-i\Delta\epsilon_{ij}t_1}] e^{-t_3/T_{2,i-t_1/T_{2,j}}} \quad (9.8)$$

with $\Delta\epsilon_{ii} = \epsilon_{i+i} - 2\epsilon_i$ and $\Delta\epsilon_{ij} = \epsilon_{i+j} - \epsilon_i - \epsilon_j$. Similarly, the non-rephasing response functions can be grouped together:

$$\sum_{l=4}^6 R_l = \sum_{i,j} \mu_{0,i}^2 \mu_{0,j}^2 [e^{-i(\epsilon_i t_3 + \epsilon_j t_1)} e^{-t_2/T_{1,ii-t_3/T_{2,i-t_1/T_{2,j}}}} + e^{-i\epsilon_j(t_3+t_1)} e^{i(\epsilon_i - \epsilon_j)t_2} e^{-t_2/T_{1,ij-(t_3+t_1)/T_{2,j}}} \times [1 - e^{-i\Delta\epsilon_{ij}t_1}] \quad (9.9)$$

In the present case we consider three coupled oscillators: the free OH–stretch vibration, the main transition of the hydrogen-bonded OH oscillator, and the first sideband of this latter oscillator centered at 3510 cm^{-1} . Since the pump and probe spectra used to get the result shown in Fig. 9.10 are only resonant with the $0 \rightarrow 1$ transition, we included only a single sideband for the fundamental transition of the hydrogen-bonded OH group. Hence, $i = 1, 2, 3$ and $j = 1, 2, 3$, where resonances 1 and 2 denote the main transition and the sideband of the hydrogen-bonded OH group, respectively, and resonance 3 the free OH group. To simplify the description, we assumed that $\Delta\epsilon_{13} = \Delta\epsilon_{23}$ which means that the coupling between the free OH group and the hydrogen bonded OH group is the same for the main transition as for the sideband. Further, it should be noted that in this particular case it is not possible to create a state $|1+2\rangle$, because the resonances 1 and 2 originate from the same oscillator. Hence, the terms $-e^{-i\Delta\epsilon_{12}t_1}$ and $-e^{-i\Delta\epsilon_{21}t_1}$ are removed from the rephasing and non-rephasing response functions.

To arrive at the third-order polarization generated in the pump-probe experiment, the response functions are convoluted with the electric fields of the pump and probe. Under the assumption that the field of the pump $\mathcal{E}_1(t)$ is much stronger than the

probe $\mathcal{E}_2(t)$, the third-order polarization $P^{(3)}(t)$ in the direction of the probe \mathbf{k}_2 is given by:

$$\begin{aligned}
 P^{(3)}(k_2, t) \propto & \int_0^\infty dt_1 \int_0^\infty dt_2 \int_0^\infty dt_3 \\
 & [\mathcal{E}_2(t-t_1)e^{-i\omega_2(t-t_1)}\mathcal{E}_1(t-t_1-t_2)\mathcal{E}_1^*(t-t_1-t_2-t_3)e^{-i\omega_1 t_3} + \\
 & \mathcal{E}_1(t-t_1)\mathcal{E}_2(t-t_1-t_2)e^{-i\omega_2(t-t_1-t_2)} \times \\
 & \mathcal{E}_1^*(t-t_1-t_2-t_3)e^{-i\omega_1(t_2+t_3)}] \times \\
 & \sum_1^3 R_i(t, t_1, t_2, t_3) + \\
 & [\mathcal{E}_2(t-t_1)e^{-i\omega_2(t-t_1)}\mathcal{E}_1^*(t-t_1-t_2)\mathcal{E}_1(t-t_1-t_2-t_3)e^{i\omega_1 t_3} + \\
 & \mathcal{E}_1(t-t_1)\mathcal{E}_1^*(t-t_1-t_2)e^{-i\omega_1 t_2} \times \\
 & \mathcal{E}_2(t-t_1-t_2-t_3)e^{-i\omega_2(t-t_1-t_2-t_3)}] \times \\
 & \sum_4^6 R_i(t, t_1, t_2, t_3) + c.c.
 \end{aligned} \tag{9.10}$$

The parameters used to obtain the calculated result of Fig. 9.10 are partly obtained from other measurements and partly from a fit to the data. The parameters obtained from the narrow-band measurements are listed in the upper part of Table 9.1 together with the dephasing times which were deduced from the width of the peaks of the linear absorption spectrum, which we assumed to be homogeneously broadened. The pump and probe fields were given by $\mathcal{E}_1(t) = e^{-4 \ln 2 (t/\tau_p)^2}$, $\mathcal{E}_2(t) = e^{-4 \ln 2 [(t-\tau)/\tau_p]^2}$ with τ the delay between pump and probe and $\tau_p = 200$ fs, $\omega_1 = \omega_2 = 3590$ cm⁻¹. The parameters obtained from a fit to the data in Fig. 9.10 are the cross anharmonicities, the lifetimes of the coherences and the cross sections. They are displayed in the lower part of Table 9.1.

9.5 Discussion

The vibrational lifetime of the free OH-group of pinacol of 7.4 ps is very similar to the lifetimes observed for several monomeric mono-alcohols dissolved in apolar solvents, like methanol dissolved in CCl₄, C₂Cl₄, C₄Cl₆, 1-decanol dissolved in CCl₄ and 2,2-dimethyl-3-ethyl-3-pentanol dissolved in CCl₄ [47, 48, 49]. The lifetime of the OH-stretch vibration has been observed to depend strongly on the strength of the O-H...O hydrogen bond interaction. The strength of the hydrogen bond is reflected in the red shift of the OH band $\Delta\omega_{OH}$ with respect to the gas phase frequency. For many systems, the lifetime of the OH-stretch vibration follows the empirical relation [59] $T_1 \propto 1/(\Delta\omega_{OH})^{1.8}$. For pinacol, $\Delta\omega_{OH}$ is small, making the lifetime of the OH-stretch vibration relatively long compared to for instance the lifetime of

Table 9.1. Parameters for the fit of Fig. 9.10. Those obtained from narrow-band measurements are displayed above, the fit results below the horizontal line

parameter	value
frequency ϵ_1	3570 cm ⁻¹
frequency ϵ_2	3510 cm ⁻¹
frequency ϵ_3	3610 cm ⁻¹
diagonal anharmonicity $\Delta\epsilon_{11}$	-180 cm ⁻¹
diagonal anharmonicity $\Delta\epsilon_{22}$	-180 cm ⁻¹
diagonal anharmonicity $\Delta\epsilon_{33}$	-160 cm ⁻¹
lifetime $T_{1,11}$	3.5 ps
lifetime $T_{1,22}$	3.5 ps
lifetime $T_{1,33}$	7.4 ps
dephasing time $T_{2,1}$	0.4 ps
dephasing time $T_{2,2}$	0.4 ps
dephasing time $T_{2,3}$	0.4 ps
cross anharmonicity $\Delta\epsilon_{13}$	-12 cm ⁻¹
cross anharmonicity $\Delta\epsilon_{23}$	-12 cm ⁻¹
lifetimes coherences $T_{1,13}$	2.3 ps
lifetimes coherences $T_{1,23}$	2.3 ps
lifetimes coherences $T_{1,12}$	2.0 ps
cross sections	$ \mu_{0,1} ^2 = 10 \mu_{0,2} ^2 = 2 \mu_{0,3} ^2$

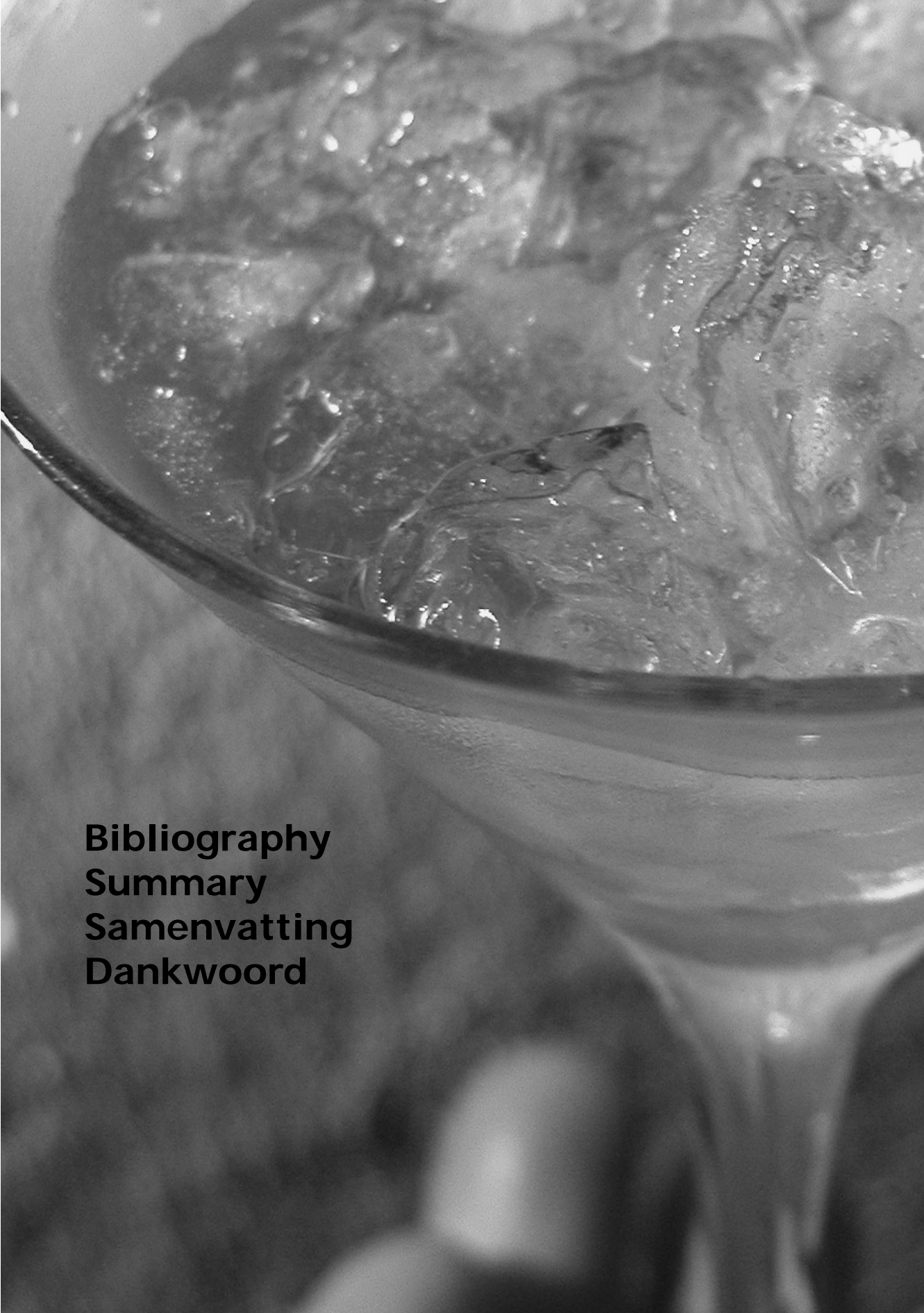
ethanol clusters dissolved in CCl₄, that show a lifetime on a sub-picosecond time scale [107].

The observation of oscillations with a frequency of 60 cm⁻¹ on the pump-probe signal shows that the hydrogen bond mode is underdamped. Coherent vibrational dynamics in a hydrogen bonded system were reported only recently and explored by means of infrared pump probe and photon echo spectroscopy on phthalic acid monomethylester [89, 90]. It was shown that the oscillation of the hydrogen bond length led to a modulation of the frequency of the OH or OD stretch vibration. Observation of an oscillatory component with a frequency of 40 cm⁻¹ implies that the free and hydrogen bonded OH-groups of the gauche conformer are coupled. Interestingly, this coupling does not lead to energy transfer between the two OH-groups, which is in contrast with the behavior of coupled amide I bands of small peptides in water [112]. However, here it should be realized that energy transfer not only requires a coupling, but also fluctuations of this coupling or of the energy levels. For tri-alanine dissolved in water, energy transfer between two amide I bands with a time constant of 5.3 ps was observed. For tri-alanine, the energy transfer rate was observed to be enabled by fluctuations of the coupling between both amide I bands that are caused by fluctuations in the peptide backbone. The absence of any population transfer in

pinacol molecules can well be explained from the rigidity of the pinacol “backbone” and from the weak interactions with chloroform molecules.

9.6 Summary

We have performed mid-infrared pump probe spectroscopy on pinacol monomers in solution, which adopt conformations *trans* and *gauche* with respect to the central C–C axis. The *trans* molecules have two equivalent OH–groups, absorbing at 3610 cm^{-1} ; in the *gauche* conformation an internal hydrogen bond between the OH–groups is formed, leading to one bonded OH–group absorbing at 3570 cm^{-1} , and one free OH–group, absorbing at 3610 cm^{-1} . Excitation of either of these bands leads to a bleaching at the same frequency and an induced absorption that is red-shifted 180 cm^{-1} or 160 cm^{-1} , for the bonded and free OH-stretch vibration, respectively. For the hydrogen-bonded OH–groups, side bands are observed that show the same dynamics as the main transition band and are attributed to a progression of an anharmonically coupled low frequency mode, probably a hydrogen bond mode. The lifetime of the bonded OH-stretch is found to be $T_b = 3.5 \pm 0.4\text{ ps}$, that of the free OH-stretch vibration $T_f = 7.4 \pm 0.5\text{ ps}$. Broadband excitation of both OH-stretch bands leads to oscillations on the pump-probe signal with frequency components of 40 and 60 cm^{-1} . The frequency of 40 cm^{-1} indicates the presence of a coupling between the free and bonded OH–groups in the *gauche* conformer. The frequency of 60 cm^{-1} results from the quantum interference of the main transition and the first sideband of the bonded OH–group.



Bibliography
Summary
Samenvatting
Dankwoord

Bibliography

- [1] H. J. Bakker. Effect of intermolecular interactions on vibrational energy transfer in the liquid phase. *J. Chem. Phys.* **98**, 8496–8506 (1993).
- [2] H. J. Bakker, P. C. M. Planken, L. Kuipers, and A. Lagendijk. Ultrafast infrared saturation spectroscopy of chloroform, bromoform and iodoform. *J. Chem. Phys.* **94**, 1730–1739 (1991).
- [3] J. Barthel, K. Bachhuber, R. Buchner, and H. Hetzenauer. Dielectric spectra of some common solvents in the microwave region. Water and lower alcohols. *Chem. Phys. Lett.* **165**, 369–373 (1990).
- [4] J. E. Bertie, M. Khalique Ahmed, and S. Baluja. Infrared intensities of liquids. 6. A study of the effect of water purity and dissolved gases on the intensity of the OH stretching band of H₂O(l). *J. Phys. Chem.* **93**, 6660–6661 (1989).
- [5] J. E. Bertie, M. Khalique Ahmed, and H. H. Eysel. Infrared intensities of liquids. 5. Optical and dielectric constants, integrated intensities, and dipole moment derivatives of water and water-d₂ at 22 °C. *J. Phys. Chem.* **93**, 2210–2218 (1989).
- [6] N. Bloembergen, E. M. Purcell, and R. V. Pound. Nuclear magnetic resonance absorption. *Phys. Rev.* **73**, 679–712 (1948).
- [7] R. W. Boyd. *Nonlinear Optics*. (Academic Press, San Diego, 1992).
- [8] J. Chesnoy and D. Ricard. Experimental study of vibrational relaxation in liquid hydrogen chloride. *Chem. Phys. Lett.* **73**, 433–437 (1980).
- [9] Q. Cui and M. Karplus. Molecular properties from combined QM/MM methods. I. Analytical second derivative and vibrational calculations. *J. Chem. Phys.* **112**, 1133–1149 (2000).
- [10] M. Dahlqvist, M. Hotokka, and M. Räsänen. Structures and vibrational spectra of pinacol. 1 Infrared and matrix infrared spectra of monomeric pinacol. Ab initio calculations on conformers and vibrational frequencies. *Chem. Phys.* **229**, 137–147 (1998).

Bibliography

- [11] M. Dahlqvist and R. Sillanpää. Structures and vibrational spectra of pinacol. Part 2. A new crystal form of pinacol: a key to the infrared spectroscopic identification of the G and T conformers in condensed phases. *J. Mol. Str.* **524**, 141–149 (2000).
- [12] J. C. Deák, S. T. Rhea, L. K. Iwaki, and D. D. Dlott. Vibrational energy relaxation and spectral diffusion in water and deuterated water. *J. Phys. Chem. A* **104**, 4866–4875 (2000).
- [13] K. Ekvall, P. van der Meulen, C. Dhollande, L.-E. Berg, S. Pommeret, R. Naskrecki, and J.-C. Mialocq. Cross phase modulation artifact in liquid phase transient absorption spectroscopy. *J. Appl. Phys.* **87**, 2340–2352 (2000).
- [14] T. Elsaesser and H.J. Bakker. In T. Elsaesser and H.J. Bakker, editors, *Ultrafast hydrogen bonding dynamics and proton transfer in the condensed phase*, chapter 1. Kluwer Academic Publishers, Dordrecht, 2002.
- [15] U. Emmerichs, S. Woutersen, and H. J. Bakker. Generation of intense femtosecond optical pulses near $3\mu\text{m}$ with a kilohertz repetition rate. *J. Opt. Soc. Am. B* **14**, 1478–1483 (1997).
- [16] M. Falk. Frequency of HOH, HOD and DOD bending fundamentals in liquid water. *J. Raman. Spec.* **21**, 563–567 (1990).
- [17] M. Falk and T. A. Ford. Infrared spectrum and structure of liquid water. *Can. J. Chem.* **44**, 1699–1707 (1966).
- [18] T. A. Ford and M. Falk. Hydrogen bonding in water and ice. *Can. J. Chem.* **46**, 3579–3586 (1968).
- [19] B. M. Fung and T. M. McGaughy. Molecular motions in liquid I. Rotation of water and small alcohols by deuteron relaxation. *J. Chem. Phys.* **65**, 2970–2976 (1976).
- [20] G. M. Gale, G. Gallot, F. Hache, N. Lascoux, S. Bratos, and J.-Cl. Leickman. Femtosecond dynamics of hydrogen bonds in liquid water: a real time study. *Phys. Rev. Lett.* **82**, 1068–1071 (1999).
- [21] O. Golonzka, M. Khalil, N. Demirdöven, and A. Tokmakoff. Vibrational anharmonicities revealed by coherent two-dimensional infrared spectroscopy. *Phys. Rev. Lett.* **86**, 2154–2157 (2001).
- [22] H. Graener, T. Patzlaff, N. Kadarisman, and G. Seifert. Observation of intensity dependent, non-exponential vibrational relaxation in liquid bromoform. *Chem. Phys. Lett.* **348**, 403–410 (2001).

- [23] H. Graener and G. Seifert. Vibrational and orientational relaxation of monomeric water molecules in liquids. *J. Chem. Phys.* **98**, 36–45 (1992).
- [24] H. Graener, G. Seifert, and A. Laubereau. Direct observation of rotational relaxation times by time-resolved infrared spectroscopy. *Chem. Phys. Lett.* **172**, 435–439 (1990).
- [25] H. Graener, G. Seifert, and A. Laubereau. New spectroscopy of water using tunable picosecond pulses in the infrared. *Phys. Rev. Lett.* **66**, 2092–2095 (1991).
- [26] H. Graener, G. Seifert, and A. Laubereau. Vibrational and reorientational dynamics of water molecules in liquid matrices. *Chem. Phys.* **175**, 193–204 (1993).
- [27] H. Graener, T. Q. Ye, and A. Laubereau. Ultrafast vibrational predissociation of hydrogen bonds: Mode selective infrared photochemistry in liquids. *J. Chem. Phys.* **91**, 1043–1046 (1989).
- [28] D. Hadži and S. Bratos. Vibrational spectroscopy of the hydrogen bond. In P. Schuster, G. Zundel, and C. Sandorfy, editors, *The Hydrogen Bond*, volume II, chapter 12. Elsevier, Amsterdam, 1976.
- [29] P. Hamm, M. Lim, W. F. DeGrado, and R. M. Hochstrasser. Stimulated photon echoes from amide I vibrations. *J. Phys. Chem. A* **103**, 10049–10053 (1999).
- [30] P. Hamm, M. Lim, W. F. DeGrado, and R. M. Hochstrasser. Pump/probe self heterodyned 2D spectroscopy of vibrational transitions of a small globular peptide. *J. Chem. Phys.* **112**, 1907–1916 (2000).
- [31] P. Hamm, M. Lim, and R. M. Hochstrasser. Structure of the amide I band of peptides measured by femtosecond nonlinear-infrared spectroscopy. *J. Phys. Chem. B* **102**, 6123–6138 (1998).
- [32] U. Happek, J. R. Engholm, and A. J. Sievers. Frequency and temperature dependence of the vibrational relaxation of the SH stretch mode in vitreous As₂S₃. *Chem. Phys. Lett.* **221**, 279–282 (1994).
- [33] S. E. Harris, M. K. Oshman, and R. L. Byer. Observation of tunable optical parametrical fluorescence. *Phys. Rev. Lett.* **18**, 732–734 (1967).
- [34] E. J. Heilweil, M. P. Casassa, R. R. Cavanagh, and J. C. Stephenson. Temperature dependence of the vibrational population lifetime of OH($v = 1$) in fused silica. *Chem. Phys. Lett.* **117**, 185–189 (1985).
- [35] G. Herzberg. *Molecular spectra and molecular structure. II: Infrared and Raman spectra of polyatomic molecules*. (D. van Nostrand Company, New York, 1945).

Bibliography

- [36] J. R. Hill, E. L. Chronister, T. C. Chang, H. Kim, J. C. Postlewaite, and D. D. Dlott. Vibrational relaxation and vibrational cooling in low temperature molecular crystals. *J. Chem. Phys.* **88**, 949–967 (1988).
- [37] J. R. Hill, D. D. Dlott, C. W. Rella, K. A. Peterson, S. M. Decatur, S. G. Boxer, and M. D. Fayer. Vibrational dynamics of carbon monoxide at the active sites of mutant heme proteins. *J. Phys. Chem.* **100**, 12100–12107 (1996).
- [38] J. R. Hill, C. J. Ziegler, K. S. Suslick, D. D. Dlott, C. W. Rella, and M. D. Fayer. Tuning the vibrational relaxation of CO bound to heme and metalloporphyrin complexes. *J. Phys. Chem.* **100**, 18023–18032 (1996).
- [39] R. Jimenez, G. R. Fleming, P. V. Kumar, and M. Maroncelli. Femtosecond solvation dynamics of water. *Nature* **369**, 471–473 (1994).
- [40] W. L. Jorgensen. Optimized intermolecular potential functions for liquid alcohols. *J. Phys. Chem.* **90**, 1276–1284 (1986).
- [41] M. Khalil, N. Demirdöven, and A. Tokmakoff. Obtaining absorptive line shapes in two-dimensional infrared vibrational correlation spectra. *Phys. Rev. Lett.* **90**, 047401 (2003).
- [42] J. T. Kindt and C. A. Schmuttenmaer. Far-infrared dielectric properties of polar liquids probed by femtosecond terahertz pulse spectroscopy. *J. Phys. Chem.* **100**, 10373–10379 (1996).
- [43] M. F. Kropman and H. J. Bakker. Dynamics of water molecules in aqueous solvation shells. *Science* **291**, 2118–2120 (2001).
- [44] L. P. Kuhn. The hydrogen bond: Intra- and intermolecular hydrogen bonds in alcohols. *J. Am. Chem. Soc.* **74**, 2492–2499 (1952).
- [45] R. Laenen and C. Rauscher. A structural model for associated liquid ethanol developed from transient spectroscopy. *J. Chem. Phys.* **107**, 9759–9763 (1997).
- [46] R. Laenen and C. Rauscher. Transient hole-burning spectroscopy of associated ethanol molecules in the infrared: structural dynamics and evidence for energy migration. *J. Chem. Phys.* **106**, 8974–8980 (1997).
- [47] R. Laenen and K. Simeonidis. Towards a more detailed understanding of the OH-stretching bands of H-bonded liquids. *Chem. Phys. Lett.* **290**, 94–98 (1998).
- [48] R. Laenen and K. Simeonidis. Energy relaxation and reorientation of the OH mode of simple alcohol molecules in different solvents monitored by transient IR spectroscopy. *Chem. Phys. Lett.* **299**, 589–596 (1999).

- [49] R. Laenen and K. Simeonidis. Librational substructure of the OH-stretching band of an H-bonded dimer observed by time-resolved spectroscopy. *J. Mol. Str.* **552**, 147–152 (2000).
- [50] S. H. Lin. Theory of vibrational relaxation and infrared absorption in condensed media. *J. Chem. Phys.* **65**, 1053–1062 (1976).
- [51] A. J. Lock and H. J. Bakker. Temperature dependence of the vibrational relaxation in liquid H₂O. *J. Chem. Phys.* **117**, 1708–1713 (2002).
- [52] A. J. Lock, S. Woutersen, and H. J. Bakker. Ultrafast energy equilibration in hydrogen-bonded liquids. *J. Phys. Chem. A* **105**, 1238–1243 (2001).
- [53] W. H. Louisell, A. Yariv, and A. E. Siegman. Quantum fluctuations and noise in parametric processes. *Phys. Rev.* **124**, 1646–1654 (1961).
- [54] D. Madsen, J. Stenger, J. Dreyer, E. T. J. Nibbering, P. Hamm, and T. Elsaesser. Coherent vibrational ground-state dynamics of an intramolecular hydrogen bond. *Chem. Phys. Lett.* **341**, 56–62 (2001).
- [55] Y. Maréchal. Infrared spectra of water I: Effect of temperature and of H/D isotopic substitution. *J. Chem. Phys.* **95**, 5565–5573 (1991).
- [56] Y. Maréchal. Infrared spectra of water II: Dynamics of H₂O (D₂O) molecules. *J. Phys. II France* **3**, 557–571 (1993).
- [57] M. P. McDonald and L. D. R. Wilford. Infrared study of pinacol and its two hydrates. *Spectrochim. Acta* **29A**, 1407–1417 (1973).
- [58] W. Mikenda. Stretching frequency versus bond distance correlation of O—D(H)···Y (Y = N, O, S, Se, Cl, Br, I) hydrogen bonds in solid hydrates. *J. Mol. Str.* **147**, 1–15 (1986).
- [59] R. E. Miller. The vibrational spectroscopy and dynamics of weakly bound neutral complexes. *Science* **240**, 447–453 (1988).
- [60] R.D. Mountain. Comparison of a fixed-charge and a polarizable water model. *J. Chem. Phys.* **103**, 3084–3090 (1995).
- [61] S. Mukamel. *Principles of Nonlinear Optical Spectroscopy*. (Oxford University Press, New York, 1995).
- [62] H.-K. Nienhuys, A. J. Lock, R. A. van Santen, and H. J. Bakker. Dynamics of water molecules in an alkaline environment. *J. Chem. Phys.* **117**, 8021–8029 (2002).

Bibliography

- [63] H.-K. Nienhuys, R. A. van Santen, and H. J. Bakker. Orientational relaxation of liquid water molecules as an activated process. *J. Chem. Phys.* **112**, 8487–8494 (2000).
- [64] H.-K. Nienhuys, S. Woutersen, R. A. van Santen, and H. J. Bakker. Mechanism for vibrational relaxation in water investigated by femtosecond infrared spectroscopy. *J. Chem. Phys.* **111**, 1494–1500 (1999).
- [65] A. Nitzan and J. Jortner. Vibrational relaxation of a molecule in a dense medium. *Mol. Phys.* **25**, 713–734 (1973).
- [66] A. Nitzan, S. Mukamel, and J. Jortner. Some features of vibrational relaxation of a diatomic molecule in a dense medium. *J. Chem. Phys.* **60**, 3929–3934 (1974).
- [67] A. Novak. Hydrogen bonding in solids. Correlation of spectroscopic and crystallographic data. *Struct. Bonding (Berlin)* **18**, 177–216 (1974).
- [68] A. W. Omta, M. F. Kropman, S. Woutersen, and H. J. Bakker. Negligible effect of ions on the hydrogen-bond structure in liquid water. *Science* **301**, 347–349 (2003).
- [69] A. Pakoulev, Z. Wang, and D. D. Klott. Vibrational relaxation and spectral evolution following ultrafast OH stretch excitation of water. *Chem. Phys. Lett.* **371**, 594–600 (2003).
- [70] P. Pant, R. E. Riter, and N. E. Levinger. Influence of restricted environment and ionic interactions on water solvation dynamics. *J. Chem. Phys.* **109**, 9995–10003 (1998).
- [71] C. G. Park, M. Nakata, and M. Tasumi. Infrared induces conformational isomerization and reverse reaction in the dark of 1,2-propanediol in low temperature argon matrices. *J. Mol. Str.* **174**, 1–4 (1988).
- [72] C. G. Park and M. Tasumi. Reinvestigation of infrared induced conformational isomerizations of 1,2-ethanediol in low temperature Ar matrices and reverse reaction in the dark. *J. Phys. Chem.* **95**, 2757–2762 (1991).
- [73] K. A. Peterson, C. W. Rella, J. R. Engholm, and H. A. Schwettman. Ultrafast vibrational dynamics of the myoglobin amide I band. *J. Phys. Chem. B* **103**, 557–561 (1999).
- [74] B. M. Pettitt and M. Karplus. The structure of water surrounding a peptide: a theoretical approach. *Chem. Phys. Lett.* **136**, 383–386 (1987).
- [75] K. D. Rector, A. S. Kwok, A. Tokmakoff, C. W. Rella, and M. D. Fayer. Vibrational anharmonicity and multilevel vibrational dephasing from vibrational echo beats. *J. Chem. Phys.* **106**, 10027–10036 (1997).

- [76] R. Rey and J. T. Hynes. Vibrational energy relaxation of HOD in liquid D₂O. *J. Chem. Phys.* **104**, 2356–2368 (1996).
- [77] R. Rey, K. B. Moeller, and J. T. Hynes. Hydrogen bond dynamics in water and ultrafast infrared spectroscopy. *J. Phys. Chem. A* **105**, 11993–11996 (2002).
- [78] M. Rini, B. Z. Magnes, E. Pines, and E. T. J. Nibbering. Real-time observation of bimodal proton transfer in acid-base pairs in water. *Science* **301**, 349–352 (2003).
- [79] I. V. Rubtsov, J. Wang, and R. M. Hochstrasser. Dual frequency 2D-IR of peptide amide-A and amide-I modes. *J. Chem. Phys.* **118**, 7733–7736 (2003).
- [80] I. V. Rubtsov, J. Wang, and R. M. Hochstrasser. Vibrational coupling between amide-I and amide-A modes revealed by femtosecond two color infrared spectroscopy. *J. Phys. Chem. A* **107**, 3384–3396 (2003).
- [81] B. Ruscic, A. F. Wagner, L. B. Harding, R. L. Asher, D. Feller, D. A. Dixon, K. A. Peterson, Y. Song, X. Qian, C. Y. Ng, J. B. Liu, W. Chen, and D. W. Schwenke. On the enthalpy of formation of hydroxyl radical and gas-phase bond dissociation energies of water and hydroxyl. *J. Phys. Chem. A* **106**, 2727–2747 (2002).
- [82] L. Saiz, J. A. Padro, and E. Guardia. Structure and dynamics of liquid ethanol. *J. Phys. Chem. B* **101**, 78–86 (1997).
- [83] J. R. Scherer, M. K. Go, and S. Kint. Raman spectra and structure of water from -10 to 90°. *J. Phys. Chem.* **78**, 1304–1313 (1974).
- [84] Y. R. Shen. *The Principles of Nonlinear Optics*. (John Wiley & Sons, New York, 1984).
- [85] T. Shimanouchi. *Tables of molecular vibrational frequencies consolidated*, volume I. (National Bureau of standards, Washington, D.C., 1972).
- [86] F. A. J. Singelenberg and J. H. van der Maas. Fourier transform infrared study of hydrogen bonding between an OH-donor and a vicinal oxygen acceptor. *J. Mol. Str.* **240**, 213–223 (1990).
- [87] F. A. J. Singelenberg and J. H. van der Maas. Hydrogen-bonding in non-cyclic vicinal diols and their mono-methyl ethers: an FTIR study. *J. Mol. Str.* **243**, 111–122 (1991).
- [88] A. Staib and J. T. Hynes. Vibrational predissociation in hydrogen bonded OH··O complexes via OH stretch-OO stretch energy transfer. *Chem. Phys. Lett.* **204**(1,2), 197–205 (1993).

Bibliography

- [89] J. Stenger, D. Madsen, J. Dreyer, P. Hamm, E.T.J. Nibbering, and T. Elsaesser. Femtosecond mid-infrared photon echo of an intramolecular hydrogen bond. *Chem. Phys. Lett.* **354**, 256–263 (2002).
- [90] J. Stenger, D. Madsen, J. Dreyer, E.T.J. Nibbering, P. Hamm, and T. Elsaesser. Coherent response of hydrogen bonds in liquids probed by ultrafast vibrational spectroscopy. *J. Phys. Chem. A* **105**, 2929–2932 (2001).
- [91] J. Stenger, D. Madsen, P. Hamm, E.T.J. Nibbering, and T. Elsaesser. Ultrafast vibrational dephasing of liquid water. *Phys. Rev. Lett.* **87**, 027401 (2001).
- [92] G. Stock and W. Domcke. Detection of ultrafast molecular-excited-state dynamics with time- and frequency-resolved pump-probe spectroscopy. *Phys. Rev. A* **45**, 3032–3040 (1992).
- [93] S. J. Suresh and V. M. Naik. Hydrogen bond thermodynamic properties of water from dielectric constant data. *J. Chem. Phys.* **113**, 9727–9732 (2000).
- [94] A. Szabo. Theory of fluorescence depolarization in macromolecules and membranes. *J. Chem. Phys.* **81**, 150–167 (1984).
- [95] K.L. Vodopyanov. Water and ethanol as bleachable radiation absorbers in an yttrium-erbium-aluminium garnet laser ($\lambda=2.94\ \mu\text{m}$). *Sov. Phys. JETP* **55**, 1049–1051 (1982).
- [96] K.L. Vodopyanov. Laser-induced generation of subnanosecond sound pulses in liquids. *Sov. Phys. JETP* **64**, 67–70 (1986).
- [97] K.L. Vodopyanov. Bleaching of water by intense light at the maximum of the $\lambda \sim 3\ \mu\text{m}$ absorption band. *Sov. Phys. JETP* **70**, 114–121 (1990).
- [98] K.L. Vodopyanov. Saturation studies of H_2O and HDO near $3400\ \text{cm}^{-1}$ using intense picosecond laser pulses. *J. Chem. Phys.* **94**, 5389–5393 (1991).
- [99] S. Völker. Hole-burning spectroscopy. *Annu. Rev. Phys. Chem.* **40**, 499–530 (1989).
- [100] G. Walrafen. *Water, A Comprehensive Treatise*. (Plenum, New York, 1972).
- [101] Z. Wang, A. Pakoulev, Y. Pang, and D.D. Dlott. Vibrational substructure in the OH stretching band of water. *Chem. Phys. Lett.* **378**, 281–288 (2003).
- [102] R. M. Whitnell, K. R. Wilson, and J. T. Hynes. Vibrational relaxation of a dipolar molecule in water. *J. Chem. Phys.* **96**, 5354–5369 (1992).
- [103] S. Woutersen and H. J. Bakker. Hydrogen bond in liquid water as a Brownian oscillator. *Phys. Rev. Lett.* **83**, 2077–2080 (1999).

- [104] S. Woutersen and H. J. Bakker. Resonant intermolecular transfer of vibrational energy in liquid water. *Nature* **402**, 507–509 (1999).
- [105] S. Woutersen and H. J. Bakker. Coherent coupling in frequency-resolved pump-probe spectroscopy. *J. Opt. Soc. Am.* **B 17**, 827–832 (2000).
- [106] S. Woutersen, U. Emmerichs, and H. J. Bakker. Femtosecond mid-ir pump-probe spectroscopy of liquid water: Evidence for a two-component structure. *Science* **278**, 658–660 (1997).
- [107] S. Woutersen, U. Emmerichs, and H. J. Bakker. A femtosecond midinfrared pump-probe study of hydrogen bonding in ethanol. *J. Chem. Phys.* **107**, 1483–1490 (1997).
- [108] S. Woutersen, U. Emmerichs, H.-K. Nienhuys, and H. J. Bakker. Anomalous temperature dependence of vibrational lifetimes in water and ice. *Phys. Rev. Lett.* **81**, 1106–1109 (1998).
- [109] S. Woutersen and P. Hamm. Structure determination of trialanine in water using polarization sensitive two-dimensional vibrational spectroscopy. *J. Phys. Chem. B* **104**, 11316–11320 (2000).
- [110] S. Woutersen and P. Hamm. Time-resolved two-dimensional vibrational spectroscopy of a short α -helix in water. *J. Chem. Phys.* **115**, 7737–7743 (2001).
- [111] S. Woutersen and P. Hamm. Nonlinear two-dimensional vibrational spectroscopy of peptides. *J. Phys.: Condens. Matter* **14**, 1035–1065 (2002).
- [112] S. Woutersen, Y. Mu, G. Stock, and P. Hamm. Subpicosecond conformational dynamics of small peptides probed by two-dimensional vibrational spectroscopy. *Proc. Natl. Ac. Sci.* **98**, 11254–11258 (2001).
- [113] A. Yariv. *Optical Electronics*. (Holt-Saunders International Editions, New York, 1985).

Summary

The presence of hydrogen bonds in water strongly influences the macroscopic and microscopic properties of this liquid. The network of hydrogen bonds is by no means static: the formation and breakage of bonds occurs on an ultrafast time scale of a picosecond, which is on the same order as the relaxation time of vibrations in liquids. It is therefore expected that hydrogen bonding has a profound effect on vibrational relaxation in liquids like water and ethanol.

The absorption band of the OH-stretch vibration in liquid water is inhomogeneously broadened due to the different environment each water molecule experiences. In order to reveal the dynamics of water molecules, mid-infrared pump-probe spectroscopy is applied, in which a pump pulse excites a homogeneous sub-ensemble of oscillators with the same OH-stretch frequency. By tuning the frequency of the probe pulse, the response at the same or at other frequencies can be measured as a function of time, which enables us to deduce vibrational lifetimes.

The vibrational dynamics of the OH-stretch oscillator in liquid water, however, is not revealed in a straightforward way. In Chapter 4 we show that the measured pump-probe scans are governed by two time scales: the lifetime of the excited state of the OH-stretch oscillator and the so-called equilibration time. The latter time constant represents the redistribution time of the energy of the relaxed OH-stretch vibration over all degrees of freedom, i.e. over all low(er) frequency modes. This time scale is observed to be 550 ± 50 fs at all wavelengths and at all temperatures. The lifetime T_1 of the OH-stretch vibration at room temperature is found to be 260 ± 18 fs at all wavelengths. This means that spectral diffusion in pure water occurs on a time scale shorter than the pulse duration. The lifetime of the OH-stretch vibration is observed to increase with temperature to 320 fs at 358 K. The increase in lifetime can quantitatively be explained from the overlap integral between the OH-stretch mode and the first overtone of the H-O-H bending mode. These modes spectrally overlap which enables the transfer of energy from the stretch to the bend mode, but due to the change in hydrogen bond interactions at higher temperatures, the positions and shapes of these bands change, leading to a decrease in overlap, which leads to a longer lifetime of the OH-stretch mode.

In Chapter 5 we study the equilibration process. Here, we compare the equilibration time scales of water with other hydrogen-bonding solvents like the lower alcohols as methanol, ethanol and propanol. We observe that equilibration, or thermalization, leads to a shift of the position of the OH-stretch band and a decrease of its cross section. The equilibration times are observed to increase with the mass of the

Summary

molecule for the alcohols. This means that equilibration results from repositioning of the molecules in the liquid. The wavelength dependent equilibration behavior for alcohols indicates that at least two different processes are involved in the equilibration process. For water, the equilibration time is not observed to depend on frequency. This suggests that for water the equilibration rate is determined by the time scale at which energy can be transferred from a non-thermal intermediate state, likely the overtone of the bending mode, to the low frequency modes. Hence, water can adapt extremely fast to a deposition of energy.

The work presented in Chapters 6 and 7 was triggered by a time-resolved anti-Stokes Raman study by the group of Dlott. This group came up with a reinterpretation of the results presented in Chapter 4. In Chapter 6 we show that this reinterpretation is incorrect and is not able to explain our results. The long pulses used by the group of Dlott (1.4 ps) could not distinguish between the vibrational relaxation and equilibration time. It is shown in Chapter 7 that the subsequent action of these two processes leads to a deceleration of the vibrational relaxation rate of the still excited OH-groups. Because the pulse duration in our experiment was short compared with the lifetime of the OH-stretch vibration, this deceleration effect did not play an important role in our experiments. In the experiments by Dlott, however, long pulses are used. There still exist excited OH-groups, when the relaxation and equilibration of the OH-stretches excited by the front of the pulse have already changed the temperature of the sample. This leads to a deceleration of the vibrational relaxation of the still excited OH-groups. We present a numerical model describing this feedback effect on the lifetime for liquid water. The model accurately describes both the results presented in Chapter 4 and the results of Dlott and coworkers.

In Chapter 8, vibrational and reorientational measurements are presented for water monomers with one or two hydrogen bonds. In liquid water energy hopping to neighboring molecules and redistribution of energy among the antisymmetric and symmetric mode leads to a complete delocalization of vibrational energy over the molecule. For monomers, however, we can exclusively focus on the intramolecular energy redistribution. In all experiments two processes occur: the transfer of excitation energy and the change in excitation frequency due to the formation and breakage of hydrogen bonds. In all these processes an intermediate state occurs in which the energy is delocalized. From a comparison with HDO molecules, we have shown that the breakage and formation of hydrogen bonds occurs on a time scale of 1.3 ± 0.4 ps, the lifetime of the transient state is ~ 200 fs. From the rotational anisotropy we conclude that the molecular reorientation occurs on a 6.0 ± 1.0 ps time scale.

Chapter 9, finally, is devoted to the dynamics of two OH-groups that are coupled via an intramolecular hydrogen bond. The hydrogen-bond donating OH-stretch vibration has a slightly smaller OH-resonance frequency than the hydrogen bond accepting mode, 3570 and 3610 cm^{-1} , respectively. We show that the lifetimes of these vibrations are 3.5 ± 0.4 and 7.4 ± 0.5 ps, respectively. A 60 cm^{-1} low-frequency mode is anharmonically coupled to the hydrogen-bond donating OH-groups, leading

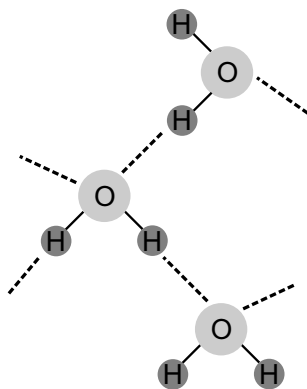
to sidebands in the transient spectra. If we use broadband excitation of both OH-groups, oscillations with frequency components of 40 and 60 cm^{-1} are observed. We have modeled these oscillations using Feynman diagrams. The 60 cm^{-1} oscillation stems from the quantum interference of the hydrogen-bond donating group with its first sideband, the 40 cm^{-1} oscillation indicates the presence of a coupling between the hydrogen bond donating and accepting OH-stretch mode.

Samenvatting

In dit proefschrift zijn de resultaten beschreven van experimenten aan vloeibaar water. Water is van essentieel belang voor al het leven, omdat veel chemische reacties in water plaats vinden. Om chemische processen beter te begrijpen is het ook nodig te doorgronden hoe water zelf, op moleculair niveau, reageert op het aanbieden van energie. Na een korte inleiding over water en waterstofbruggen, worden in deze samenvatting de gebruikte meettechniek en de uitgevoerde experimenten beschreven.

Water en waterstofbruggen

De kleinste bouwsteen van water is het watermolecuul H_2O . Dit molecuul is opgebouwd uit drie atomen: aan het zuurstofatoom (O) zitten twee waterstofatomen (H) vast. In vloeibaar water trekken deze H_2O moleculen elkaar ook een beetje aan: er wordt een waterstofbrug gevormd tussen twee buurmoleculen, in de figuur aangegeven door een stippellijn. Deze bruggen zijn verantwoordelijk voor een aantal bijzondere eigenschappen van water. Zo'n bijzondere eigenschap is het hoge kookpunt van water; het kost relatief veel energie om al die bruggen te verbreken. Nu is het allerminst zo dat die bruggen statisch zijn. Ze verbreken en groeien weer aan, worden langer en korter. Binnen het watermolecuul vinden ook bewegingen plaats. De verschillende atomen kunnen ten opzichte van elkaar trillen, waarbij de binding intact blijft. Een voorbeeld van zo'n trilling is de zogenaamde buigvibratie. Dit lijkt op een knipbewe-



Samenvatting

ging van een schaar: de hoek tussen de drie atomen van het watermolecuul schommelt om een evenwichtswaarde. Een andere beweging is die van het waterstofatoom (H) ten opzichte van het zuurstofatoom (O). Deze beweging wordt de OH-strek vibratie genoemd, een trilling waarbij de afstand tussen het zuurstof- en het waterstofatoom schommelt rond een evenwichtswaarde. Je kunt je voorstellen dat het gedrag van zo'n schommeling hevig verstoord wordt als aan het waterstofatoom een brug zit naar een buurmolecuul. De trillingsfrequentie neemt dan af. Omdat in vloeibaar water die bruggen allemaal een verschillende lengte hebben, zijn de trillingsfrequenties van de moleculen verschillend. Dat maakt het erg lastig informatie te krijgen over het gedrag van water, elk molecuul gedraagt zich namelijk anders. Bovendien leven trillingen in water erg kort, typisch iets van 1 picoseconde, dat wil zeggen 0,000000000001 seconde. Als je dit soort bewegingen wilt waarnemen, moet je erg snel kunnen meten, vandaar ook het woord *ultrafast* in de titel van dit proefschrift. De uitdaging ligt voor ons hierin dat we, ondanks alle verschillende trillingsfrequenties en ondanks de extreem korte levensduur van de trillingen, toch informatie over de structuur en dynamica van watermoleculen kunnen verkrijgen.

Het experiment

Wat is er dan nodig om zo'n trilling in gang te zetten? We doen door energie in het molecuul te stoppen met behulp van een laser. Deze laser heeft twee bijzondere eigenschappen. Ten eerste geeft hij lichtflitsjes die ongeveer 0,2 picoseconde duren. Dat is iets korter dan de levensduur van de vibraties, zodat we het gedrag daarvan goed kunnen volgen. Het proces is vergelijkbaar met fotograferen; snelle bewegingen kun je bevriezen met een sluitertijd die korter is dan de tijdschaal van de beweging. De tweede bijzondere eigenschap is dat je de kleur van de lichtflitsjes kunt instellen. Hiermee kun je verschillende soorten water moleculen bekijken: moleculen met sterke en moleculen met zwakke bruggen. Deze kleuren liggen allemaal in het voor ons onzichtbare infrarood (golflengtes rond 3000 nanometer). In de experimenten hebben we twee lichtflitsjes gebruikt. Met de eerste, energierijke flits zetten we de moleculen in trilling. Met de tweede flits bepalen we hoeveel moleculen er nog trillen op een bepaald tijdstip na de eerste flits. Een watermolecuul dat nog in trilling is, zal de energie van het tweede lichtflitsje namelijk niet absorberen; trilt het watermolecuul niet meer, dan kan het de energie weer opnemen om te gaan trillen. Door te meten hoeveel licht er door het water heenkomt, weten we hoeveel watermoleculen nog in trilling zijn. Deze meting herhalen we voor verschillende tijden na de eerste flits, zodat we kunnen zien hoe snel een trilling uitdooft. Zo'n meting geeft de levensduur van de trilling weer. Door dit te doen voor verschillende kleuren licht, krijgen we informatie over het gedrag van watermoleculen op korte tijdschalen.

Temperatuurafhankelijkheid van de levensduur

In hoofdstuk 4 hebben we voor verschillende temperaturen gekeken hoe lang de OH-strek vibratie in water leeft. We hebben ontdekt dat ze langer leven bij een hogere

temperatuur. Dat is tegen alle verwachtingen in, want bij de meeste stoffen leeft de vibratie juist korter bij een hogere temperatuur. We kunnen dit bijzondere gedrag wel verklaren. Voor water is de energie van de OH-strektrilling vrijwel gelijk aan de energie nodig voor twee buigtrillingen in water. De trilling van de OH-strektrilling verdwijnt door energieoverdracht naar de buigtrillingen. Bij hogere temperatuur gaat het overbrengen van de energie niet zo makkelijk meer. Dat komt doordat de bruggen tussen de moleculen allemaal wat zwakker worden en ervoor zorgen dat de energieën van de strek- en buigtrillingen niet goed meer passen. Doordat de overdracht van energie van de strektrilling naar de buigtrillingen moeilijker en blijft de OH-strektrilling langer leven.

In hoofdstuk 5 vergelijken we het uitdoven van deze OH-strektrillingen in water met andere stoffen die waterstofbruggen vormen, zoals ethanol (alcohol). We hebben ook gekeken hoe lang het duurt voordat de toegevoegde trillingsenergie, om het met een mooi woord te zeggen, geëquilibreerd is. Daar bedoelen we mee, dat we kijken hoe lang het duurt voordat de energie verdeeld is over alle mogelijke bewegingen van de watermoleculen. We zien dat dat proces langer duurt naarmate het molecuul groter is. Blijkbaar moeten de moleculen draaien en zich verplaatsen in de vloeistof en dat gaat langzamer als het molecuul een grotere massa heeft. Juist omdat het watermolecuul zo klein is, kan het zich dus heel snel aanpassen aan het toedienen van extra energie, zoals dat in chemische reacties gebeurt.

Concurrentie?

Het is niet zo dat wij de enige groep ter wereld zijn die zich met water bezighoudt. In de VS werkt Dana Dlott met zijn groep ook aan water. Hij gebruikt ook laserlicht om water aan het trillen te krijgen, alleen duren zijn lichtflitsjes wat langer dan bij ons. Dat hoeft geen probleem te zijn als het uitdoven van de trillingen langzamer gaat dan de duur van de lichtflits. In water is dat niet zo en dat betekent dat Dlott het uitdoven van de trillingen niet goed kan volgen. Dlott heeft een artikel geschreven waarin hij beweert dat wij onze metingen verkeerd interpreteren. Hij komt met een alternatieve verklaring voor zowel zijn als onze metingen. Zijn verklaring van onze metingen is echter inconsistent en hij ziet niet dat zijn lange pulsen een enorme invloed hebben op het gedrag van water. Daarom hebben we een commentaar geschreven op zijn stuk in hoofdstuk 6. In hoofdstuk 7 hebben we een model gemaakt waarmee we zowel zijn als onze metingen kunnen verklaren. In het rekenmodel kun je invullen hoe lang de lichtflitsjes zijn die je gebruikt; de berekeningen komen precies overeen met wat wij meten en wat Dlott meet.

Bijzondere tussentoestand

In het volgende hoofdstuk hebben we water gemengd met aceton (nagellakremover). Het resultaat hiervan zijn enkele watermoleculen met een brug, maar zonder buurwatermoleculen. Daarvoor in de plaats zitten nu een acetonmoleculen. De trillingsenergie kan nu niet meer overgedragen worden aan een ander watermolecuul. Het voordeel

Samenvatting

hiervan is dat we kunnen kijken hoe snel de energie binnen het molecuul wordt overgedragen en hoe snel een brug verbreekt en weer aangroeit. We hebben ook gemeten hoe snel zo'n watermolecuul draait. Uit die metingen hebben we ontdekt, dat er een tussentoestand bestaat, als je een waterstofbrug wilt verbreken of trillingsenergie wilt overdragen aan de andere OH-strekvibratie binnen het watermolecuul. Die tussentoestand is heel bijzonder: beide OH-groepen van het watermolecuul hebben een hele zwakke waterstofbrug en de trillingsenergie is gedelocaliseerd, dat wil zeggen dat de trilling niet vast op een OH-groep zit.

Gekoppelde trillingen

In het laatste hoofdstuk hebben we gekeken naar een alcoholmolecuul met twee OH-groepen naast elkaar. Er ontstaat dan een brug tussen die twee groepen binnen het molecuul. We zien dat de OH-strektrilling van een OH-groep met een brug sneller uitdooft dan eentje zonder. Bovendien blijkt dat bij het in trilling zetten van de OH-strekvibratie automatisch de waterstofbrug mee gaat doen en dat de frequenties van andere trillingen veranderen. Dit betekent dat de trillingen onderling gekoppeld zijn.

Ten slotte

Met deze serie experimenten hebben we het begrip van het gedrag van watermoleculen op korte tijdschaal vergroot. Dat wil niet zeggen dat het onderzoek afgerond is. De technologische ontwikkelingen op het gebied van korte laserpulsen gaan door. Dit biedt, samen met nieuwe vragen naar het gedrag van materie, genoeg perspectief voor toekomstig onderzoek.

Dankwoord

Het zit erop; vijf jaar promotieonderzoek op AMOLF heeft geresulteerd in het proefschrift dat u nu in handen heeft. In het laatste stuk wil ik de aandacht richten op de mensen die op welke manier dan ook aan de verwezenlijking van dit boekje hebben bijgedragen.

Allereerst wil ik mijn promotor Huib Bakker bedanken voor de begeleiding die hij mij de afgelopen jaren gegeven heeft. Hoewel onze samenwerking niet altijd even optimaal was, waardeer ik zijn vernieuwende ideeën en fysisch inzicht bij interpretatie van de metingen. Het heeft mij gescherpt. Sander Woutersen heeft mij kennis bijgebracht over de laseropstelling en heeft mij na zijn terugkomst uit Berlijn weten te stimuleren door op enthousiaste wijze mee te denken. In dit dankwoord mogen de huidige en vroegere groepsleden niet ontbreken. Han-Kwang Nienhuys, Frederik van den Broek, Michel Kropman, Anne-Willem Omta, Yves Rezus, Dorte Madsen, Joop Gilijamse, Adriaan Dokter, Mingcheng Zong en Ingrid Giebels wil ik bedanken voor de samenwerking en hun bijdrage tot het creëren van een goede sfeer in de groep. Frederik en Han-Kwang zijn het geweest die naast het schrijven van een degelijk meetprogramma, vraagbaak waren voor menig linux-beginner. Joop Gilijamse heeft in het kader van zijn afstudeerstage de metingen uit het achtste hoofdstuk uitgevoerd en heeft meegeholpen met die van hoofdstuk 9. Ik wil hem hartelijk danken voor deze inhoudelijke bijdrage aan het proefschrift en zijn prettige manier van samenwerken.

Menig technisch probleem werd snel en vakkundig verholpen door Henco Schoenmaker en Rob Kemper. Als louter probleemoplossers doe je hen echter tekort. Hun actief meedenken om een goed werkende opstelling te krijgen heb ik zeer gewaardeerd. Ook ondersteunende afdelingen als de werkplaats, tekenkamer en E&I wil ik bedanken voor hun accurate hulp. In het bijzonder wil ik Idsart Attema, Hans ter Horst en Henk Dekker noemen, die steeds bereid waren de detectoren optimaal af te stemmen op onze wensen.

Voor het verkrijgen van resultaat op korte termijn stond de PV garant. De afgelopen jaren heb ik met veel plezier deel uit gemaakt van de PV en dat kon alleen door de prettige omgang en manier van samenwerken binnen de PV. Daarom wil ik Ad, Afric, Andreas, Annebeth, Annemieke, Anouk, Daniëlle, Grace, Igor, Katrien, Marcel, Marcia, Marco, Marlies, Paul, Rimco, Thea, Willem, Yumna en (alweer) Yves erg bedanken.

Nóg meer afwisseling was er te vinden buiten het AMOLF. Het zal ook dan ook geen verrassing zijn dat ik vrienden en familie hier wil bedanken voor de afleiding en ontspanning die ze boden na een lange dag meten, het geduld dat ze opbrachten om de

Dankwoord

vele AMOLF verhalen en anekdotes aan te horen en voor hun morele ondersteuning in tijden dat het wat tegenzat. In het bijzonder wil hier Arthur en Caroline, Mila en Tijmen en Judie noemen. Tijmen wil ik ook bedanken voor zijn hulp bij de creatieve kant van dit boekje. Ten slotte wil ik dicht bij huis eindigen en mijn broer Jan-Pieter en mijn ouders bedanken voor hun betrokkenheid en steun door de jaren heen.

Arjan Lock, november 2003

